William & Mary
CHARTERED 1693

W&M ScholarWorks

Dissertations, Theses, and Masters Projects

Theses, Dissertations, & Master Projects

2008

Time-resolved magnetic flux and AC-current distributions in superconducting yttrium barium copper oxide thin films and multifilaments

Ran Yang
College of William & Mary - Arts & Sciences

Follow this and additional works at: https://scholarworks.wm.edu/etd

Part of the Materials Science and Engineering Commons, and the Optics Commons

Recommended Citation

Yang, Ran, "Time-resolved magnetic flux and AC-current distributions in superconducting yttrium barium copper oxide thin films and multifilaments" (2008). *Dissertations, Theses, and Masters Projects.* Paper 1539623536.
https://dx.doi.org/doi:10.21220/s2-wdzq-cx39

This Dissertation is brought to you for free and open access by the Theses, Dissertations, & Master Projects at W&M ScholarWorks. It has been accepted for inclusion in Dissertations, Theses, and Masters Projects by an authorized administrator of W&M ScholarWorks. For more information, please contact scholarworks@wm.edu.

Time-Resolved Magnetic Flux and AC-Current Distributions in Superconducting YBCO Thin Films and Multifilaments

Ran Yang
Emeishan, Sichuan, China

Master of Science, the College of William and Mary, 2007
Bachelor of Engineering with a minor in Finance, East China University of Science and Technology, 2003

A Dissertation Presented to
The Graduate Faculty of the College of William and Mary in Candidacy for
The Degree of Doctor of Philosophy

Department of Applied Science

The College of William and Mary
August 2008

APPROVAL PAGE

This dissertation is submitted in partial fulfillment of
the requirements for the degree of

Doctor of Philosophy

Ran Yang

Approved by the Committee, August, 2008

Committee Chair
Professor Gunter Luepke, Applied Science
College of William and Mary

Professor Michael J. Kelley, Applied Science
College of William and Mary

Professor William J. Kossler, Physics
College of William and Mary

Dr. Gwyn P. Williams
Jefferson Lab

ABSTRACT PAGE

Time-resolved magneto-optical imaging (TRMOI) technique allows dynamic ac transport measurements on superconductors. The high time and spatial resolutions of the measurements also offer good quantitative data analysis of the MO images. $YBa_2Cu_3O_{7-\delta}$ (YBCO) was discovered as a high-temperature superconductor (HTSC) which has wide applications due to its high critical temperature of $T_c = 91$ K, and high critical current density J_c in the order of 10^{6-7} Acm^{-2}. Many of the applications require high ac current load and a high magnetic field. We study the interaction behavior of YBCO thin films in an ac transport current and a dc magnetic field by the TRMOI technique.

In this dissertation, I first introduce the applications of high-temperature superconductors with focus on YBCO and describe the advantages of the TRMOI technique we developed over other methods to map the magnetic flux distribution of superconductors. The theories to understand the magnetic properties of HTSC are presented, followed by theoretical models. I also introduce a newly developed finite elemental method (FEM) simulation which is proved to be a better theoretical guideline to our data analysis. The TRMOI experimental setup and the procedures are discussed in detail. I show step-by-step the calibration of light intensity profiles averaged from MO images to determine magnetic field distribution, and a numerical inversion of the Biot-Savart law to calculate the current density distributions.

The current density evolution in YBCO thin films is studied by TRMOI as a function of the phase of an ac current applied simultaneously with a perpendicular dc magnetic field. The measurements show that an ac current enables the vortex matter in YBCO thin films to reorganize into two coexisting steady states of driven vortex motion with different characteristics. To study the transport current effects in YBCO thin films, we present a new empirical method to separate the total current distribution into a circulating shielding current and a transport current.

Furthermore, we performed TRMOI measurements on multifilamentary YBCO thin films with six superconducting filaments. Several sets of measurements with different experimental parameters are compared to find optimized measurements especially fitting the TRMOI technique for best quantitative results. The integrated transport current in the optimized measurements agrees fairly well with the current we applied. Nearly half of the transport current flows in the most outer two filaments while the rest of the current flows roughly evenly in the inner four filaments. Comparing with the FEM simulation results, the multifilamentary film shows higher critical current than the single bridged TBCO thin film. Finger-like inhomogeneous flux penetration patterns are observed in the TRMOI study of YBCO coated conductors in ac current regime. A quantitative analysis of the images show how the grain boundary network affects the overall behavior of the flux and current density evolution.

Contents

1 Introduction **1**
- 1.1 High-temperature Superconductors (HTSCs) . . . 1
  - 1.1.1 Various applications of HTSCs . . . 2
  - 1.1.2 YBCO . . . 5
  - 1.1.3 Why superconducting? . . . 7
- 1.2 Magnetic flux density measurements of HTSCs . . . 10
- 1.3 Outline . . . 11

2 Theories **14**
- 2.1 Magnetic properties of superconductors . . . 14
  - 2.1.1 Type I superconductors . . . 16
  - 2.1.2 Type II superconductors . . . 18
- 2.2 Flux pinning in type II superconductors . . . 20
  - 2.2.1 Vortex and vortex state . . . 20
  - 2.2.2 Flux pinning . . . 21
- 2.3 Thermal-magnetic instabilities . . . 23
  - 2.3.1 Flux dynamics . . . 23
  - 2.3.2 Flux creep and drastic avalanches . . . 24
- 2.4 The critical state model (CSM) . . . 28
  - 2.4.1 The original CSM for slab geometry . . . 28
  - 2.4.2 Modified CSM for thin film geometry . . . 30
  - 2.4.3 The finite element model (FEM) based simulation . . . 36
- 2.5 Inversion of the Biot-Savart law . . . 38

3 Experiment **41**
- 3.1 Time-Resolved magneto-optical imaging . . . 41
  - 3.1.1 Introduction to TRMOI . . . 41
  - 3.1.2 Experimental setup . . . 44
- 3.2 Experimental procedures . . . 50
  - 3.2.1 Sample preparation and mounting . . . 50
  - 3.2.2 TRMO imaging measurement . . . 54
- 3.3 Magnetic field calibration from images . . . 55

4 YBCO thin films **64**
4.1 Introduction 64
4.2 Experimental 65
4.3 Results and discussions 67
4.3.1 Phase-dependence measurements 67
4.3.2 The ac current driven dynamic vortex state 72
4.3.3 The transport current dynamics 79
4.3.4 Frequency-dependence measurements 84
4.4 Conclusion 85

5 YBCO Multifilamentary thin films **87**
5.1 Introduction 87
5.2 Experimental 88
5.3 Results and discussions 90
5.3.1 Comparing different values of ac current and dc field 90
5.3.2 The optimized measurement 96
5.4 Conclusion 107

6 The second generation (2G) superconductors - coated conductors **108**
6.1 Introduction 108
6.2 Experimental 111
6.3 Results and discussions 112
6.3.1 Inhomogeneous flux penetration 112
6.3.2 Phase dependent quantitative study 114
6.4 Conclusion 117

7 Conclusions **118**

Bibliography **121**

List of Figures

1.1 the scheme of an underground HTS power cable connecting two substations in Albany, New York. 4
1.2 The AMSC 36.5 MW, 120 rpm, 2.9×10^6 N-m, 75 Tonnes ship propulsion motor. 5
1.3 The $R - T$ curve of YBCO measured by us. 6
1.4 *Left* The crystal structure of $YBa_2Cu_3O_{7-\delta}$. *Right* (a) $\delta = 7.0$, green squares represent vacancies; (b) $\delta = 6.5$, pink shaded circles represent half-occupied sites; (c) $\delta = 6.0$. 6
1.5 An illustration of the forming of the Cooper pair. 7

2.1 The Meissner Effect. 15
2.2 The three phase (T_c, H_c and J_c) diagram of superconductivity. The highest values for H_c and J_c occur at 0 K, while the highest value for T_c occurs when H and J are zero. When considering all three parameters, the plot represents a critical surface. From this surface, and moving toward the origin, the material is superconducting. For regions outside this surface the material is normal or in a mixed state. 16
2.3 Magnetization curve of type I superconductors 17
2.4 The magnetization curve of a pure type II superconductor. 18
2.5 Type II superconductors phase transitions. 19
2.6 Vortex lines penetrate the bulk of a type II superconductor in the vortex state where $H_{c1} < H_a < H_{c2}$. In vortex state, the sample is superconducting everywhere but inside of each vortex line in which magnetic field lines can fully go through. 20
2.7 The flux pinning in bulk type-II superconductors 22
2.8 The instability diagram calculated by Denisov *et al* plotted in the $H-E$ plane[33]. 27
2.9 The slab sample geometry in the Bean model with infinite length and height. An external magnetic field is applied along the z direction. Flux penetrates the darker shaded regions $|w - a|$ where the current density stays constant and equals the critical current density j_c. . . . 29

2.10 The magnetic flux density B_x (a) and the current density J_y (b) distributions across a slab in the Bean model at different values of applied magnetic field: ($B_a < B_s$) - blue dotted lines, and ($B_a = B_s$) - the olive-green solid lines. 30
2.11 A thin film geometry of superconductor sample with infinite length and very small thickness, $\lambda << d << w$. The external magnetic field B_a is perpendicular to the thin film with strongly bent flux lines at the edges. 31
2.12 The magnetic field and current density distributions in a thin film geometry sample with different values of a perpendicular applied field B_a calculated from the modified critical state model. 34
2.13 The transport current distribution in a thin film with different values of transport current flowing along the y-direction. 35
2.14 The new transport current distribution considering a more realistic physical case, which does not create magnetic flux in the flux-free region in the thin film sample center. Different values of the applied currents from $I_T = 0.1I_c$ to $I_T = 0.8I_c$ are shown. 36
2.15 The magnetic flux density profiles (top) and the new total current distributions (bottom). The applied transport current varies from a low value $I_T = 0.1I_c$ to a large load $I_T = 1.5I_c$. 37

3.1 The Faraday Effect. 42
3.2 The iron garnet thin film magneto-optical indicator. Incident polarized light passes the indicator layer twice, and is rotated by an angle Θ_F that is proportional to the perpendicular applied magnetic field H_a. . 44
3.3 Schematic of the time-Resolved Magneto-Optical Imaging setup . Both a mercury-vapor lamp and a laser are available light sources for the MOI experiment. TRMOI requires a laser synchronized to an ac current power source. 45
3.4 Hamamatsu ORCA-ER-1394 CCD camera spectral sensitivity. At a laser light wavelength $\lambda = 527$ nm, the camera has an approximately 70% quantum effciency. 48
3.5 The synchronization scheme. The phase of ac current at which pulses are triggered is adjusted by a synchronization circuit. Laser pulses sensed by a photodiode are displayed on an oscilloscope with the ac current signal. The inset shows how laser pulses (green spikes) are synchronized with a ac current (blue sine wave) 50
3.6 Custom designed sample holder mounted on top of the cold finger. A horizontal open slit 5 mm beneath the sample is for inserting the Hall probe and the diode temperature sensor. 52
3.7 A top view of mounted sample on a sample holder.Telfon ring is excluded in this figure. 53

3.8 Calibration curve, measured points (Green markers) and a function 3.7 fitting curve (purple) at $T = 15$ K, laser PRF $f = 1000$ Hz, and the CCD camera exposure time $\tau = 30$ ms. 58
3.9 One sample calibration image of 6 filamentary YBCO thin film. The dark regions in the image shows where the superconducting filaments are, and the very bright lines are the edges of each filament. Chapter 5 presents a discussion of YBCO filamentary thin film. 58
3.10 Intensity of MO images versus the number of collect light pulses. . . . 59
3.11 A complete calibration curve. Black markers are measured calibration points, upper blue curve plots function 3.12, and lower green curve plots function 3.13 in an intensity range from 0 to 150. 62

4.1 The picture of a YBCO thin film. The bridge width $= 475\mu m$. 65
4.2 A MO image of YBCO thin film with only a perpendicular field applied. The blue lines confine a relatively homogeneous area for taking the 2D profiles. 66
4.3 The field distribution profiles across the sample width for the field-dependent measurements (calibration). The vertical black dotted lines at $x/w = [-1, 1]$ indicate where the edges are located. 67
4.4 The 26 (from 0 to 25) phase points arrangement over a full cycle of an applied ac current. 68
4.5 TRMO images for 6 different values of phase ϕ of the applied ac current with the applied field normal to the surface. To display more clear detail features, each images are enhanced in contrast and its color channels. 69
4.6 The magnetic field profiles for different values of the phases of the applied ac current with a peak value of $I_{peak} = 8A$. The top, from red to green curves are profiles taken for the first half of the period $\phi = 0°$ to 180°, and the bottom is the second half period. 71
4.7 The current density profiles for different values of the phase ϕ for the total current showing in (a) the first half period and (b) the second half period of the applied ac current. 73
4.8 The magnetic field profiles at selected phase points 0° and 90° plotted with the modified critical state model. 74
4.9 The current density profiles at selected phase points plotted with the critical state model at 0° and 90°. 75
4.10 The magnetic field distribution (**a**) and the total current density profiles (**b**) for selected phase points measured in TRMOI experiments, compared to the FEM simulations (dotted line) at 90° and 270°. . . . 77
4.11 The magnetic field (**a**) and the current density distribution (**b**) corresponding to the shielding current at $\phi = 0°$ and $\phi = 180°$, compared to the shielding current density induced by an applied field only $B_a = 10$ mT and the corresponding FEM simulations at the same phase points. 78

4.12 The time dependent transport current distributions plotted with the shielding currents (the dashed lines) at zero phase points $\phi = 0°, 180°$ and 360°. 80
4.13 The integrated transport current value for the 25 measured phase points (olive green dots), which reproduce well the applied ac current (dark green solid line). 81
4.14 The current density profiles for different values of phase for transport current (solid lines), the corresponding best fits (the dashed lines) based on the CSM and the shielding current at zero phase (the black dotted line). 82
4.15 The self-field profiles (solid lines) from the transport current plotted with the magnetic profile at zero phase $\phi = 0°$ (the dashed line). . . . 83
4.16 The magnetic field distribution across the YBCO thin film bridge of 10 different frequencies at $\phi = 90°$ and 270° phases of ac transport current. 85

5.1 The YBCO multi-filamentary thin film sample with six etched filaments: a 3D drawing and a microscopic top view picture taken by our MOI optical setup. 89
5.2 One TRMO image of six-multifilamentary film with $I_{tr} = 8A$ and no external field. The dotted lines indicate each filament's edge, and the dashed lines indicate the region of interest to take the profiles for further analysis. The dark circles and wavy lines are due to the MO indicator's imperfections. Using background correction, we can obtain more homogeneous light intensity. 90
5.3 The enhanced color contrast TRMO images with applied ac current with peak $I_{peak} = 8$ A and applied field $B_a = 5$ mT at three phase points. The images show only the areas with relatively homogeneous light illumination and the least amount of defects. 91
5.4 The magnetic field distribution (top) and the total current distribution (bottom) for the multifilamentary YBCO sample while only applying a transport current ($I_{peak} = 8$ A) without any external field ($B_a = 0$ mT). The total current density distribution is also the transport current density distribution. The positive and negative ac current cycles are colored in cyan-magenta shades. The vertical dotted lines indicate the edges of each filament. 92
5.5 The magnetic field distribution (top), the total current distribution (middle) and the transport current distribution (bottom) of the multifilamentary YBCO sample with an ac transport current ($I_{peak} = 4$ A) flowing and an external field ($B_a = 10$ mT). The positive and negative ac current cycles are colored in limegreen-firered shades. The vertical dotted lines indicate the edges of each filament. 94

5.6 The integrated transport current (dots) plotted with the applied transport current (dashed black lines) for the left - with an ac transport current ($I_{peak} = 4$ A) flowing and an external field ($B_a = 10$ mT), and the right - with ac transport current ($I_{peak} = 8$ A) flowing without any external field ($B_a = 0$ mT), respectively. 95
5.7 The cross section intensity profiles of the multi-filamentary YBCO sample with an ac transport current ($I_{peak} = 8$ A) flowing and an external field ($B_a = 5$ mT). The inset shows an example of the peaks at certain filament edge that need to use the extended calibration procedure to get the correct magnetic field profiles. The positive and negative ac current cycles are colored in red-black-blue shades. 97
5.8 The magnetic field distribution (top), the total current distribution (middle) and the transport current distribution (bottom) the multi-filamentary YBCO sample with an ac transport current ($I_{peak} = 8$ A) flowing and an external field ($B_a = 5$ mT). The positive and negative ac current cycles are colored in red-black-blue shades. 98
5.9 The integrated transport current (red dots) when applying an ac transport current ($I_{peak} = 8$ A) and an external field ($B_a = 5$ mT), which agrees fairly well with the applied ac current (the dashed black curve). 100
5.10 The integrated transport current for each filament labeled by percentage of the applied transport current plotted in clustered cylinders. . . 101
5.11 A schematic drawing of the filaments coupling. Left, filaments are completely coupled and the right, when they are completely decoupled. 102
5.12 The transport current density at two extreme phase points in a comparison with the modified CSM. 102
5.13 The FEM simulated data of applying an ac transport current ($I_{peak} = 8$ A) and an external field ($B_a = 5$ mT). The top - the magnetic field distribution and the bottom - the total current density distribution. The positive and negative ac current cycles are colored in red-yellow-blue shades. 104
5.14 The measured magnetic field (top) and total current density (bottom) distribution(solid lines) comparing with the FEM simulation(dashed lines) at $\phi = 90°$ (blue), $\phi = 270°$ (red) and $\phi = 180°$ (green) phase points 105

6.1 The configuration of SuperPower 2G HTS Wire fabricated by an automated, continuous process using thin film deposition techniques to apply the superconducting material on buffered metal substrates. . . 109
6.2 TRMO images of a YBCO coated conductor for different phase points of the applied ac current in a perpendicular magnetic filed $Ba = 19$ mT. 112
6.3 A series of MO images of YBCO coated conductor strip with increaing dc current $I = 2420 - 3770$ mA and an external magnetic field $B_a = 10$ mT. 113

6.4 The color contrast enhanced MOI image of YBCO coated conductor strip with a dc current $I = 3770$ mA and a dc external magnetic field $B_a = 10$ mT. 114
6.5 The magnetic field profiles for different values of the phase of the applied ac current. The inset shows the phase points chosen in the plot. 115
6.6 The current density profiles for different values of the phases. The inset shows the phase points chosen in the plot. 116

To Curt.

Acknowledgements

First and foremost, I thank my advisor Gunter Lüpke, who gave me the opportunity to study at the College of William and Mary. He not only served as my supervisor, but also encouraged and challenged me throughout my academic program. I will be always grateful to him for his valuable advice, support and guidance in my research and future work. This dissertation could not been written without Professor Gunter Lüpke.

I must also thank Dr. Andrea Lucarelli, who has been my mentor and a friend during the years of my research in the college. His theoretical and experimental knowledge helped me rise to graduate research, and complete my program of study.

I would like to express my appreciation to my other committee members: Professor Michael J. Kelley, who advised me in my graduate coursework; Professor William J. Kossler in Department of Physics, who provided instructive comments during my study at the college, and Dr. Gwyn P. Williams at Jefferson National Laboratory, for his instructive comments on my thesis.

I am grateful to Paul Barnes, Timothy Haugan and George Levin of the Air force Research Laboratory, OH for both providing samples and sound advice.

I wish to thank Alex Frey and Stephanie Hümmert. These visiting students from Germany participated in my research area for one year. Their outstanding work significantly contributed to the project and helped me complete this dissertation.

I also wish to acknowledge and thank all of my classmates and friends at the College. My social and intellectual interactions with them helped me enjoy my time in the graduate program.

I must thank my parents-in-law, Liz and Sam Ward for their dedicated love and support since the very beginning.

I must thank my parents in China, Yiwei Zhang and Yafei Yang, for their love and affectionate encouragement despite the distance between us.

No words can express how grateful I am to my husband, Curt Ward, for his great love, understanding, and patience. Thank you Curt for giving me strength and encouragement to continue my degree program during even the most difficult circumstances.

Chapter 1

Introduction

Superconductivity is a phenomenon observed in numerous materials at very low temperatures. A material is said to be superconducting if it has zero electrical resistance and no interior magnetic fields. Superconductivity was first discovered in mercury by the Dutch physicist Heike Kamerlingh Onnes in 1911 after he successfully liqulified helium by cooling it to 4 K[1]. Scientists and engineers throughout the world have been striving to develop an understanding of this remarkable phenomenon. Much progress has been made, in fact, superconductivity is being applied in diverse areas including: medicine, theoretical and experimental science, the military, transportation, power production, electronics, and many other areas.

1.1 High-temperature Superconductors (HTSCs)

The transition temperature from the normal-to-superconducting state is a superconductor's critical temperature T_c. Before 1986, all superconductors did not exceed a critical temperature of 30 K. High-temperature superconductors with critical temperature in excess of 90 K were discovered in 1986 by German physicists Karl Muller and Johannes Bednorz[2]. Such significant increase of T_c opened new interests and

research in superconductivity. With the T_c value being higher than the boiling point 77 K of liquid nitrogen, there are more feasible commercial applications.

High-temperature superconductors are a category of superconducting ceramic materials with perovskite structure (metal-oxide ceramics that normally have a ratio of two metal atoms to every three oxygen atoms), which normally have a critical temperature greater than 30 K. Rare earth oxide ceramic materials such as the $REBa_2Cu_3O_{7-\delta}$ (where RE = Y, Sm, Nd, etc) compound have been discovered to be high temperature superconductors in the late 1980s. Since then, the critical temperature of HTSC continues increasing: from the $YBa_2Cu_3O_{7-\delta}$ (YBCO) with a $T_c = 92$ K in 1987[3] to a world record of $T_c = 195$ K for $(Sn_{1.0}Pb_{0.5}In_{0.5})Ba_4Tm_6Cu_8O_{22+}$ in July 2008[4].

Besides traditional ceramic materials, a second family of high temperature superconductors with $T_c = 26$ K was discovered in spring 2008, soon researchers found materials in the same family of iron-based superconductors that have transition temperatures of 41 K reported in June 2008[5,6]. Such new discoveries indicate that layered iron oxypnictides are promising as a new material platform for further exploration of high-temperature superconductivity.

High-temperature superconductors are classified by their critical temperatures. Normally if the materials have T_c lower than liquid nitrogen's boiling point of 77 K, they are considered to be low-temperature superconductors.

1.1.1 Various applications of HTSCs

On a timeline of HTSC research and development[7], the first generation high-temperature superconducting bismuth strontium calcium copper oxide $(Bi, Pb)_2Sr_2Ca_2Cu_3O_x$ (also called as BSCCO or Bi-2223) wires were made in 1989. Five years later in 1994, 1-km BSCCO wires were achieved. Unlike conventional superconductors, the

electrons in HTSC materials travel along the grains of the atomic lattice in straight lines. If the alignment between the atomic lattice of separate grains is off by several degrees, superconductivity will drop dramatically. For BSCCO such alignment is fairly easy. BSCCO wires with kilometers of length are already commercially used in power cables, high-efficiency industrial motors, lightweight ship propulsion systems and electricity-storing flywheels.

The downside of BSCCO wires is the high-end cost - almost ten times more expensive than the normal copper wires. Due to its poor texture, misoriented grain boundaries can block more than 75% of the current and reduce the current density to about $10^4 Acm^{-2}$ [8]. The high anisotropy of BSCCO weakens the vortex pinning and greatly limits its usage in high magnetic fields.

In 1995, physicists at Los Alamos National Laboratory and Oak Ridge National Laboratory turned to the second generation (2G) HTSCs wires known as YBCO coated conductors. Such wire can carry a current density as high as $10^6 Acm^{-2}$ and is a lot cheaper in cost and higher in magnetic field tolerance[9]. The development of 2G coated conductor wire grew fast. In 1999, a meter-long 2G YBCO coated conductor wire was made that can carry 122 A. Today, 2G HTSC power cables are used globally in industrialized nations such as in Japan, Korea, China, and the United States. In 2006, a 350-meter-long 2G wire carrying more than 200 A was installed in Albany, New York (Fig. 1.1[7]). This cable is expected to supplement the power grid to carry enough extra energy to power more than 70,000 homes. Researchers point out that in the US most power supply cables are old and ready to be replaced. The increased demand for electricity will require more power cables installed especially in crowded urban areas. The Department of Energy estimates that some 3,500 kilometers of the power cables in the US could be upgraded to 2G superconductor cables.

The new technology is still young and it will take a long time to adapt infrastruc-

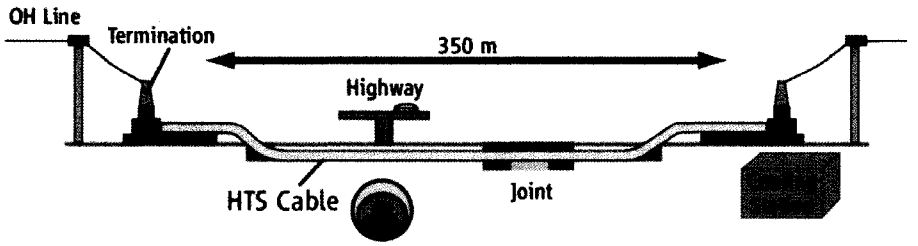

Figure 1.1: the scheme of an underground HTS power cable connecting two substations in Albany, New York.

ture to wider use. It is hard to judge its stability and security level for long-term applications.

Other than large load and high efficiency power transmission, high-temperature superconductor thin films are used for front-end filters in base-station receivers for cell phones[8,9]. The micro-strip filters patterned in a YBCO film offers advantages over the conventional, room-temperature filters: The narrow bandpass rejects interference from other cell-phone channels at neighboring frequencies , consequently reducing the noise and increasing transmission quality. The low noise allows larger distances between stations and reduces the network cost especially in rural areas. In the real market, Superconducting Technologies Inc. (STI) has installed over 5,500 HTSC filters in the US[8]. However, the development of conventional filters may overcome the benefits of HTSC filters with less cost.

Large scale applications of HTSCs include the magnetically levitated trains, already operating in China, Germany and Japan, large motors, and synchronous condensers. American Superconductor Corporations (AMSC) built two dynamic reactive power generator systems with 12-MVAR reactive power for low cost and high reliability to compensate large reactive load imbalances. AMSC also developed a full-scale, high power density, lightweight 36.5 MW propulsion motor (Fig.1.2)[8] and a drive system for naval applications. For the next generation of aircraft to achieve less - or even nonpolluting fuel, engineers at NASA[10] have disclosed several electrical com-

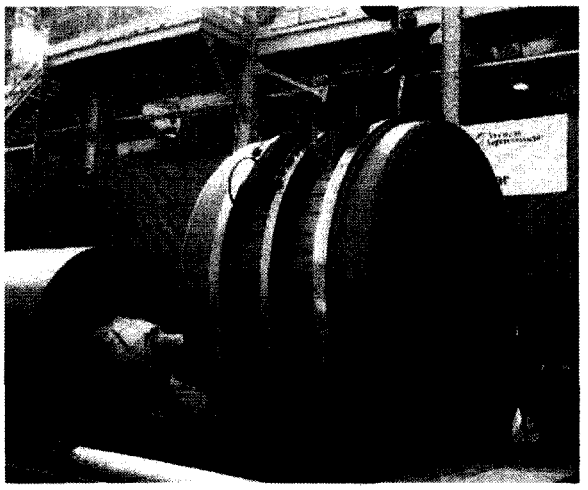

Figure 1.2: The AMSC 36.5 MW, 120 rpm, 2.9×10^6 N-m, 75 Tonnes ship propulsion motor.

ponents used to convert aircraft to electrical propulsion. Such inventions considered superconducting technology based motors and generators with high efficiency and power densities comparable to gas turbines.

Cost is still the critical challenge for HTSC applications. Before widespread use of HTSCs can occur, more advancements will be needed for increased stability, lower maintenance, and reduced cost.

1.1.2 YBCO

One of the best known high temperature superconductor, $YBa_2Cu_3O_{7-\delta}$ (YBCO), was synthesized by scientific groups[3] in 1987, and has a T_c of 91 K (Fig.1.3), a higher temperature than of the boiling point of liquid nitrogen.

Oxygen stoichiometry is a crucial property of the $YBa_2Cu_3O_{7-\delta}$ compound. In general, the oxygen stoichiometry in such compound can fluctuate in the range $6.0 < \delta < 7.0$; however, only values between $6.5 < \delta < 7.0$ present superconducting properties. Fluctuations in the copper valence are directly related to variations in the oxygen stoichiometry. If oxygen content varies in the range $6.5 < \delta < 7.0$, both

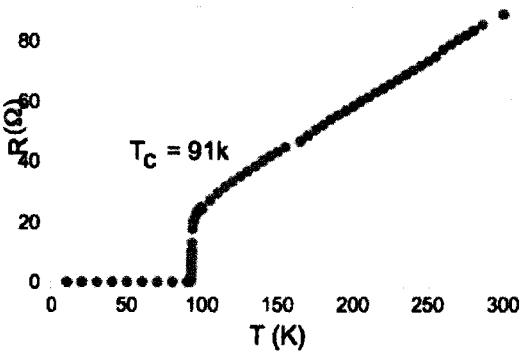

Figure 1.3: The $R-T$ curve of YBCO measured by us.

Cu^{2+} and Cu^{3+} cations are both present in the structure. For oxygen stoichiometry $\delta = 6.5$, the sample presents only Cu^{2+}. Figure 1.4 indicates different structures of $YBa_2Cu_3O_{7-\delta}$ when the value of δ varies. The critical temperature T_c increases when oxygen content increases and when $\delta > 0.5$, YBCO will lose its superconductivity[11].

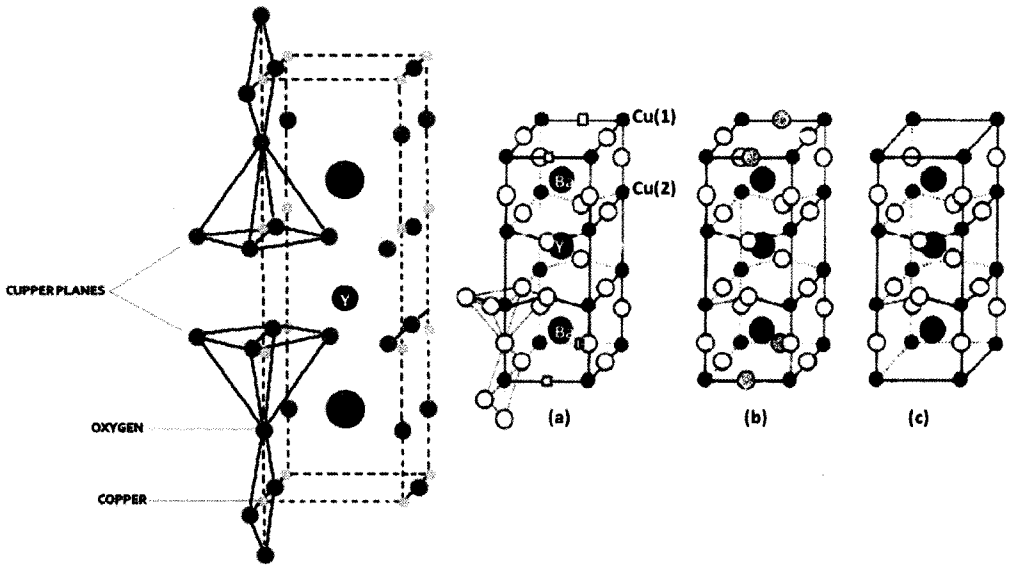

Figure 1.4: *Left* The crystal structure of $YBa_2Cu_3O_{7-\delta}$. *Right* (a) $\delta = 7.0$, green squares represent vacancies; (b) $\delta = 6.5$, pink shaded circles represent half-occupied sites; (c) $\delta = 6.0$.

As the first material to become superconducting above nitrogen boiling temperature, 77 K, single crystals of YBCO also have a very high critical current density $J_c \approx 1 \times 10^6 Acm^{-2}$ that is crucial for practical applications[12]. Though the crystals

have the critical density, the temperatures are hard to maintain for gross commercial applications. As with all ceramic material, YBCO is very brittle and is difficult to form the flexible long wires for power transmission.

1.1.3 Why superconducting?

There are many theories to explain superconductivity. Before the discovery of HTSCs, the most famous theory is the *BCS theory*[13] developed by three American physicists John Bardeen, Leon Cooper and Robert Schrieffer in 1957.

In BCS theory, Cooper explained that electrons in a superconductor act as pairs, so called *Cooper pairs*, rather than as individual particles. All Cooper pairs travel in a superconductor as a single entity and establish an electrical current. Unlike fermions and the Bose condensation, there is only elastic scattering for the Cooper pairs. In superconductors, there is no resistance to the Cooper pairs motion, so the induced current that induced continues to flow after the removal of an applied voltage. Since all electrons have same negative charges and normally repel each other, an

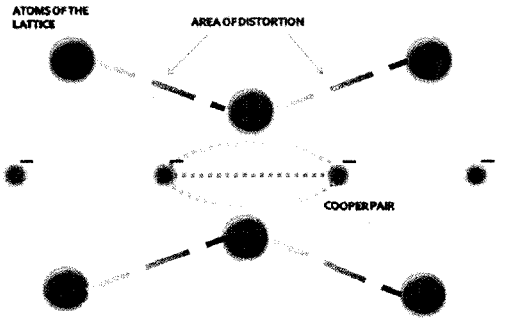

Figure 1.5: An illustration of the forming of the Cooper pair.

overwhelming attraction between the Cooper pairs of superconductors must exist. As

one negatively charged electron passes by positively charged ions, the superconductor's crystal lattice distorts. This in turn causes phonons to be emitted which forms a path of positive charges around the electron. A second electron is pulled into the path before the distortion relaxes back to normal. In such a process, two electrons, which are supposed to repel each other paired up, and the forces exerted by the phonons overcome the Columb force. When one electron in a Cooper pair passes an ion in the crystal lattice, a vibration will pass from ion to ion until the other electron of the pair absorbs the vibration, which keeps a Cooper pair together. Fig. 1.5 illustrates how the Cooper pairs become linked together.

The BCS theory states that two electrons attract to each other through interactions with the phonons, and such electron pairing puts the material into a lower energy state. As temperature rises, the Cooper pairs start to separate into single electrons and superconductivity eventually ceases to exist. The BCS theory is able to give an approximation for the quantum-mechanical state of the system of pairing electrons inside metals. The BCS also quantitatively gives the superconducting transition temperature in terms of the electron-phonon coupling potential and the Debye cutoff energy, in its simplest form:

$$K_B T_c = 1.14 E_D e^{-\frac{1}{N(0)V}}. \tag{1.1}$$

This theory ruled the superconductor world until the late 1980s, but it is insufficient to describe the observed features of high-temperature superconductivity.

As shown in the YBCO crystalline structure (Fig. 1.4), the compounds contain planes of copper and oxygen ions. Electrons will only travel from copper ion to copper ions, which differs from pure metal superconductors where the electrons pair with one another and interact with phonons[14]. In high-temperature superconductors, electrons push each other and interact with each copper ion. The proper material

doping process can create superconductivity. To explain this type of superconductivity, scientists have tried many theories. Some argue that waves of magnetism act like phonons in conventional superconductors. The electrons are little magnets which make the adjacent copper ion spins point in opposite directions to create an up-down-up-down pattern. Such antiferromagnetism cause electrons to tilt and flip, and the waves move through such a pattern and provide the electron pairing[15]. Some theorists focus on a subtle quantum connections between electrons on neighboring copper ions and states no pairing or waves are necessary to pass. This is known as the resonating valence bond (RVB) theory[16]. Still others say that both the magnetic waves and the RVB theory play some essential roles to explain superconductivity. Other theorists believe stripes of electric charges on the planes are necessary to trigger the pairing; or that loops of current flowing inside the copper - oxygen planes are the key.

Most researchers do not think there is one magical theory to fully explain the high-temperature superconducting phenomenon. Researchers also attempt to use the computer to solve this problem. They numerically simulate the electrons hopping around the copper planes and try to obtain all the different phases and the pairing mechanism from the interactions between electrons. Generally theorists use a so called Hubbard model, the simplest model of interacting particles in a lattice, to map the electron motions[17]. The ease with which the electrons hop and the Coulomb interaction strength are the only two parameters to adjust. However, the complexity of the quantum mechanical calculations limits the calculation to only dozens of lattice sites for manageable approximations.

Even after twenty-two years of effort since the discovery of HTSCs in 1986, and more than a hundred thousand articles of literature are published on high-temperature superconductors, scientists still do not find a theory or a series of theories to explain high-temperature superconductivity. But the high-temperature superconductivity

has led to many new aspects of science and technology, for example, the new discoveries of revolutionary materials, and new concepts of experimental condensed matter physics. Physicists believe in the next two decades, the mystery of high-temperature superconductivity will be unveiled.

1.2 Magnetic flux density measurements of HTSCs

High- temperature superconductors are widely used in a magnetic field with a large load of ac current. It's important to observe and understand the electric and magnetic properties of HTSCs in these conditions, which require spatial distribution measurements of the magnetic field flux density of HTSCs.

Different imaging techniques are available to study the spatial distribution of the magnetic field in HTSC thin films. One example is Lorentz microscopy[18] that uses a coherent high energy electron beam to image vortices. It has the ability to correlate very high resolution bulk magnetic and material images, but it has limited detectable fields and sample dimensions. Similarly, magnetic force microscopy (MFM) also has poor minimum detectable fields, and it is difficult to interpret the images due to its unknown micro-magnetic structure of the tip. Finally, the Scanning Hall probe microscopy[19] and Hall sensor array[20] are techniques using Hall sensors to image magnetic flux profiles at the surface of superconductors. It has great strength in imaging samples non-invasively over a broad range of temperatures and applied magnetic fields, but slow image acquisition time is a major drawback of the technique so real time imaging is not possible. Scanning SQUID(the Superconducting QUantum Interference Device) microscopy is the most sensitive magnetic field sensing element. SQUID has outstanding minimum detectable fields and quantitative output but relatively poor spatial resolution. Magneto-optical imaging (MOI) is based on the Faraday effect. Directly placing a magneto-optically active indicator film on the

superconductor sample surface as close as possible, one can image the magnetic fields by virtue of rotations in the polarized direction of passing light[21–23].

MOI has the advantages of being quantitative and quick to implement. MOI is a direct and real time method to observe the magnetic flux behaviors of HTSCs. However, reported MOI studies were limited to constant external magnetic field and/or a DC applied current[24–27], or to measurements under rather slowly evolving conditions like thermal relaxation of magnetic flux in the remnant state[28]. Dynamic studies with high time resolution MOI measurements with an ac current applied are new and will allow us to investigate ac behavior of HTSCs, which brings the MOI technique to a higher level – a new *time-resolved magneto-optical imaging* (TRMOI) technique[29]. It is capable of measuring cyclic magnetic flux distributions in planar superconductors carrying alternating current with different frequencies, normally from 100 Hz to 1000 Hz, and the spatial resolution is up to $1\mu m$. The higher spatial resolution is limited by the distance of magneto-optical indicator films and the sample, and the domain walls of the indicator films could introduce image artifacts and perturb samples.

1.3 Outline

In Chapter 2, We discuss important theories of superconductors, especially for the type II superconductors, magnetic properties, flux pinning and thermal instabilities. We also discuss the critical state model that is essentially a guideline for our quantitative imaging analysis.

In Chapter 3, we describe the time-resolved magneto-optical imaging experimental technique. It includes a detailed experimental setup, a walk-through of the experimental procedure, the sample preparation and mounting, and a discussion of the magnetic field calibration procedure from magneto-optical (MO) images.

In Chapter 4, we present the magnetic flux and current distributions measure-

ments of YBCO thin films. We observed for the first time the vortex state evolution driven by an ac transport current. A quantitative study of the TRMO images reveals the coexistence, during the ac cycle, of a quasi-static state in the thin film interior and a disordered dynamic state near the edges of the thin film. We further discuss a separation of the total current distribution, an asymmetric transport current and a circulating shielding current. This chapter also contains a study of frequency dependence measurement of YBCO thin film in a range of 100 Hz to 1000 Hz.

In Chapter 5, we present the first magnetic flux and ac current distribution measurements of multi-filamentary YBCO thin films using TRMOI. The thin film with six filaments is measured at different values of applied ac current and/or an external magnetic field. We explicitly measured and analyzed the six-filament YBCO thin film with peak value of 8 A applied ac current and a 5 mT perpendicular field. The ac phase dependence results show that most of the applied ac transport current flows in the outer two filaments while the inner four filaments carry almost the same amount of current. From our MO images one can clearly observe the magnetic flux moves from one edge to the other edge on each filament as the transport current alternates. A quantitative analysis is given and agrees very well with the experiment. The comparison with the FEM simulations are present, and the multifilamentary film exhibits a critical current value twice as high as the YBCO thin films.

In Chapter 6, we present the TRMOI measurements of the second generation (2G) YBCO high temperature superconductors, which are also known as coated conductors that have been developed and manufactured in recent years. Different from single crystal YBCO thin film, the coated conductors' grain boundaries result in non-uniform flux penetration patterns and bear a lower current density. We also give examples of quantitative studies on phase dependence measurements and show how the grain boundary structure affects the overall profiles.

In Chapter 7, the last chapter of this dissertation, we offer conclusions and recommendations for future experiments.

Chapter 2

Theories

In this chapter, we present a theoretical basis for the magnetic properties of superconductors. Because superconductors are typically classified as type-I or type-II, we provide definitions and examples of each classification. However, we purposely focus on type II superconductors as they are critical to our work; specifically, the vortex and vortex state; the flux pinning mechanism, the thermal-activated flux creep[30,31] and the thermal-magneto instabilities such as flux jumps[32,33] and finger pattern avalanches[34]. We also present a detailed discussion of Bean's critical state model and its extensions for different sample geometries in order to study the transport and magnetic behaviors of type-II superconductors. The aforementioned gives the quantitative magneto-optical imaging technique a theoretical support.

2.1 Magnetic properties of superconductors

Another characteristic of superconductivity is the exclusion of magnetic flux. A perfect superconductor is also an ideal diamagnet. This effect is called the *Meissner effect* discovered in 1933 by the German physicists Walther Meissner and Robert Ochsenfeld . When an external magnetic field, H_a , is applied along the z direction of

a superconducting sample, an induced surface current arises which completely shields the external field from the bulk.

The fundamental mechanism of superconductor diamagnetism arises from the persistent screening current which shields it from the applied field. Figure 2.1 shows a superconductor sample in its normal state (Left) and in the Meissner state (Right) when an external magnetic field is applied.

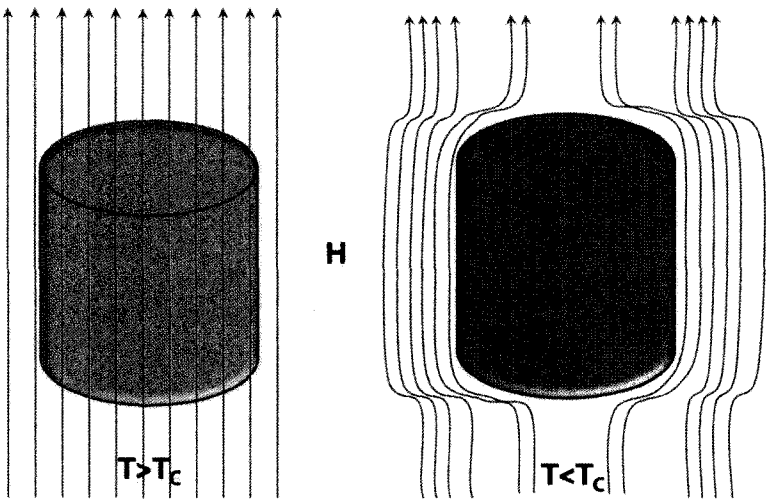

Figure 2.1: The Meissner Effect.

The Meissner effect occurs for low applied magnetic fields H_a, otherwise, the magnetic flux will penetrate the interior of the sample causing its superconductivity to decrease. For many applications of superconductors , such as creating strong electromagnets, the superconductor must carry large currents without energy losses. While an electrical current is flowing in a superconductor, a magnetic field is created. The field increases as the current increases. Each superconductor material has its own critical current density J_c. When the applied current is too large, the superconductor will go into the normal state. Figure 2.2 shows a phase diagram for three parameters, T_c, H_c and J_c. Each of these parameters depends upon on the other two. Maintaining

the superconducting state requires that both the magnetic field and the current density, as well as the temperature, remain below the critical values, all of which depend on the material.

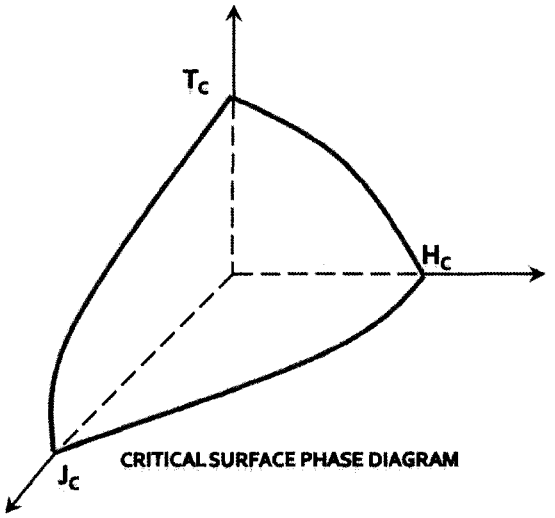

Figure 2.2: The three phase (T_c, H_c and J_c) diagram of superconductivity. The highest values for H_c and J_c occur at 0 K, while the highest value for T_c occurs when H and J are zero. When considering all three parameters, the plot represents a critical surface. From this surface, and moving toward the origin, the material is superconducting. For regions outside this surface the material is normal or in a mixed state.

Superconductors do not always behave as perfect diamagnets in an applied magnetic field. Their phase transitions often vary and as do their physical properties, leading to classification as *type I* and *type II* superconductors.

2.1.1 Type I superconductors

Type I superconductors behave like perfect diamagnets in an applied magnetic field $H_a < H_c$. The value of H_c depends on the material itself. Magnetic flux lines do not penetrate inside type I superconductors. The BCS theory and its variations explain these types of superconductors quite well[13]. The Cooper pairs move over a relatively large distance in a regularly structured lattice of the material. However, the attractive

force between Cooper pairs is small and if the temperature increases past the bond's threshold, the bond will break.

To minimize the electromagnetic free energy carried by a superconducting current, the shielding current only flows on the surface with the thickness of the London penetration depth λ (from the London equation which describes the Meissner effect[35].) When $H_a > H_c$, superconductivity breaks down and the material goes into the normal state with zero magnetization.

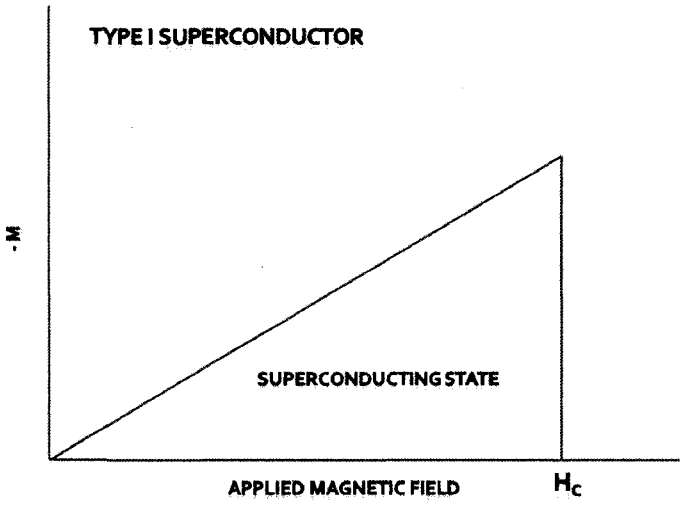

Figure 2.3: Magnetization curve of type I superconductors

Figure 2.3 shows magnetization M versus applied field H_a curve of type I superconductors. When an external magnetic field H_a is applied to a type I superconductor, the magnetization cancels the applied field until an abrupt breakdown from the superconducting state to the normal state. Ideally, this abrupt change of superconductivity from $M = -H_a$ to $M = 0$ happens at $H_a = H_c$ when the demagnetization effects are neglected.

Often, very pure elemental superconductors such as mercury, lead, and tin are type I superconductors. Such very pure elemental type I superconducting materials typically have very low critical fields and are not useful in superconducting magnets.

For example, pure superconducting lead has a critical field of only 800 gauss, which is large for type I superconductors.

2.1.2 Type II superconductors

All high temperature superconductors are type II superconductors. Examples of type II superconductors include: YBCO, some elemental superconductors such as niobium and carbon nanotubes, and some metal alloy materials such as MgB_2. Type II superconductors have two critical fields H_{c1} and H_{c2}. Applying an external field $H_a < H_{c1}$, they behave same as type I superconductors.

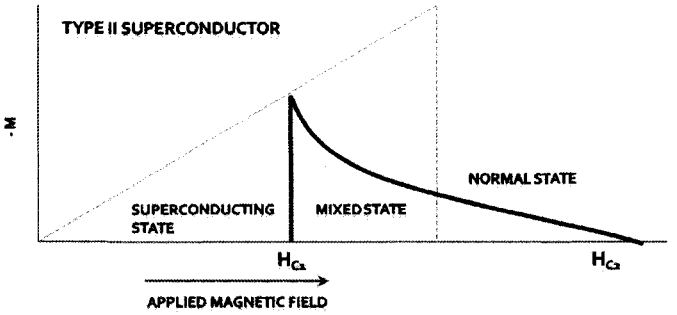

Figure 2.4: The magnetization curve of a pure type II superconductor.

Figure 2.4 shows the magnetization curve for type II superconductors. As the applied field H_a increases from H_{c1} the magnetic flux starts to enter the sample and the magnetization M decreases to zero once the applied magnetic field $H_a = H_{c2}$. Eventually, the whole superconductor sample is penetrated by the flux and loses its superconductivity.

Figure 2.5 shows the applied field H_a and temperature T phase diagram of type II superconductors. The two critical magnetic fields are temperature dependent. As the temperature increases to T_c, both H_{c1} and H_{c2} decrease to zero. When the applied magnetic field $H_a < H_{c1}$, the magnetic flux is completely shielded from the superconductor and it stays in a perfect Meissner state. While for $H_{c1} < H_a < H_{c2}$, the outer

edges of the superconductor are penetrated by magnetic flux; the area penetrated by the flux is called a mixed state. The ratio of penetration depth λ to coherence length ξ is known as the Ginzburg-Landau parameter κ, defined as $\kappa = \frac{\lambda}{\xi}$. Generally, if this value is greater than 0.7, complete flux exclusion is no longer favorable and flux is allowed to penetrate the superconductor through cores. The coherence length is smaller than the London penetration depth λ in type II superconductors. Thus when $H_{c1} < H_a < H_{c2}$, the external magnetic flux can penetrate inside of the superconductor in the form of single flux lines. This penetration forms a mixed state with some of the material in the normal state yet the interstitial space continues to superconduct. For external magnetic fields greater than the upper critical field, the material is no longer superconducting, and it is in the normal state.

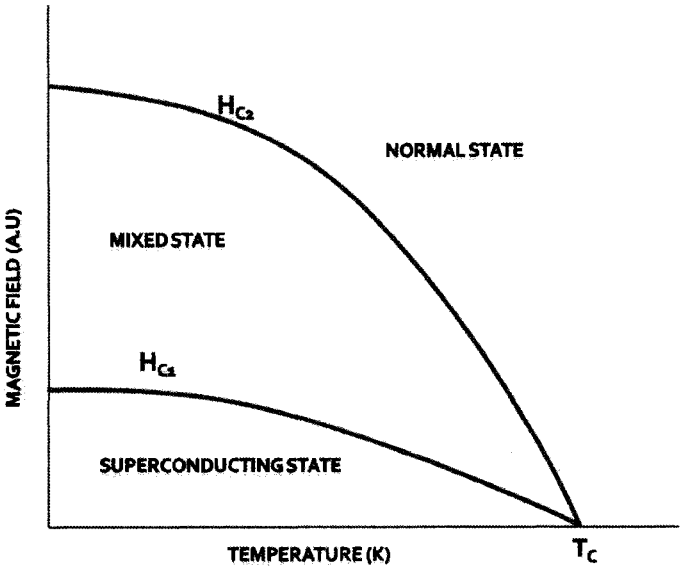

Figure 2.5: Type II superconductors phase transitions.

The crystal growth orientation of high-temperature ceramic superconductors will also affect the two critical magnetic fields H_{c1} and H_{c2} due to the layered crystal structures. Type II superconductors usually have high values of H_{c2}. For example, YBCO superconductors have upper critical field values greater than 100 Tesla at very

low temperature. Both high values of H_c, T_c and also high critical current density make YBCO an advanced superconducting material capable of facilitating various applications.

2.2 Flux pinning in type II superconductors

2.2.1 Vortex and vortex state

Type-II superconductors act like a diamagnetic material when in the Meissner state. The Meissner current runs in a thin boundary layer at the surface and expels all the externally applied magnetic fields. As the strength of the applied magnetic field H_a increases, the superconducting sample transitions from the Meissner state to a mixed state as shown in the phase diagram 2.5. In the mixed state between H_{c1} and H_{c2}, the magnetic field penetrates the bulk of type II superconductor in the form of quantized flux lines. We call such a flux line a *vortex* and the mixed state a *vortex state.*

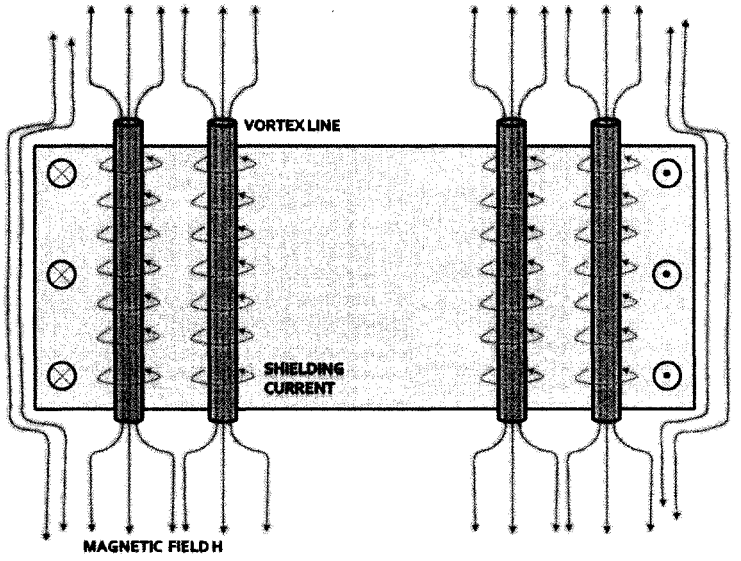

Figure 2.6: Vortex lines penetrate the bulk of a type II superconductor in the vortex state where $H_{c1} < H_a < H_{c2}$. In vortex state, the sample is superconducting everywhere but inside of each vortex line in which magnetic field lines can fully go through.

Each vortex line can contain several the elementary flux quanta $\Phi_0 = \frac{h}{2e}$. A magnetic field can exist in a normal conducting state inside of each of the vortex lines. A magnetic field can also exist outside of the vortex lines if the material is superconducting. The superconducting currents surrounding each vortex line average to zero , thus confining the magnetic field inside the vortex line. Figure 2.6 illustrates the vortices and the vortex state in a type II superconducting sample.

A superconductor lowers its energy by the penetration of quantized flux. The vortices interact with each other via the Lorentz force:

$$\vec{F} = \vec{j} \times \vec{\Phi}_0, \tag{2.1}$$

where $\vec{F}$ is the Lorentz force per unit length of one vortex line, $\vec{j}$ is the current density and $\vec{\Phi}_0$ is the flux enclosed in one line. The Lorentz force leads to a repulsive interaction between flux lines, and in thermal equilibrium the vortex lines arrange in a periodic lattice pattern for clean and defect-free perfect type-II superconductors.

2.2.2 Flux pinning

In reality, there is no perfect defect-free superconductor in which the magnetic flux lines move freely through as discussed in the previous section. Impurities, crystal defects and grain boundaries in type-II superconductor materials degrade the superconducting phase locally and create small regions where the material stays normal conducting even in superconducting phase regions. When magnetic flux lines (vortex) pass through such normal conducting regions, they will be trapped (or *pinned*) thus they act as potential wells and shorten the effective length for the flux lines. Those defect regions are called pinning sites.

When the Lorentz force is larger than the pinning force, the vortex moves further

inside of the superconducting sample (Fig. 2.7). When the pinning force is equal to the Lorentz force, one obtains:

$$F_p(\vec{r}) = J_c(\vec{r}, \vec{B}) \times B(\vec{r}), \tag{2.2}$$

where J_c is the critical current density corresponding to the value where the Lorentz force equals the pinning force $\vec{F}_p$. $\vec{B}$ is an average magnetic flux density. When the pinning force $\vec{F}_p$ is homogeneous in the material, the critical current density J_c is inversely proportional to the local magnetic flux field :

$$J_c(\vec{r}, \vec{B}) = \frac{F_p(\vec{r})}{B(\vec{r})}. \tag{2.3}$$

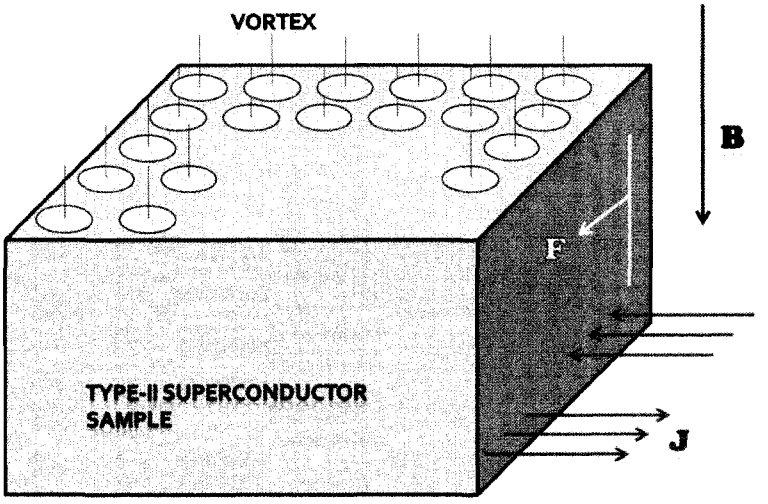

Figure 2.7: The flux pinning in bulk type-II superconductors

The flux movement creates a gradient in the magnetic field inside the superconductor sample. From Maxwell equation, one can calculate the magnetic field distribution

inside a type -II superconductor:

$$\nabla \times \vec{B} = \mu_0 \vec{J}(\vec{r}), \tag{2.4}$$

where

$$\left|\vec{J}(\vec{r})\right| = J_c(\vec{r}, \vec{B}). \tag{2.5}$$

Since there is no magnetic field flux penetration in type-I superconductors, flux pinning can only occur in type-II superconductors. Currently the ceramic high temperature superconductors suffer from thermally activated flux creep, which limits the performance of these materials at higher temperatures and at higher magnetic fields. Optimized pinning is the main available mechanism to prevent flux creep for superconductivity in these materials in the presence of external magnetic field and to improve both critical current density and critical field[36–38].

2.3 Thermal-magnetic instabilities

2.3.1 Flux dynamics

There are several forces that cause flux lines to move other than pinning force $\vec{F}_p(\vec{B}) = n_d \vec{f}_p$, where n_d is the density of defects.

When a transport current flows through the bulk of a type-II superconductor, flux lines also experience a Lorentz force and start to move under the action of the force $\vec{F}_L = \vec{j} \times \vec{B}$. If the superconductor sample is homogeneous, $\vec{F}_L$ is counteracted by a friction force density $\vec{F}_\eta = -\eta \vec{\nu}$, where $\vec{\nu}$ is the flux moving velocity. This is also the origin of a finite resistance of an ideal type-II superconductor, which corresponds to an electric field $\vec{E} = \vec{B} \times \vec{\nu}$. Similar to the Hall effect in normal conductors, an additional force called Hall force density $\vec{F}_H = n_s f \vec{\nu} \times \vec{B}$ is acting on a moving

vortex in the direction parallel to the shielding current $\vec{j}$, where n_s is the density of superconducting charge carriers and f is a dimensionless factor depending on the quasi-particle scattering rate[35].

Other fluctuating thermal forces $\delta\vec{F}(T, \vec{B}, t)$ due to temperature and vortex density also cause vortex diffusion and time decay of current density. The total possible flux motions in a type-II superconductor are summarized as :

$$\vec{F}_L + \vec{F}_\eta + \vec{F}_H + \vec{F}_p(\vec{B}) + \delta\vec{F}(T, \vec{B}, t) = 0, \tag{2.6}$$

where

$$\vec{F}_L = \vec{j} \times \vec{B}; \quad \vec{F}_\eta = -\eta\vec{\nu};$$
$$\vec{F}_H = n_s f\vec{\nu} \times \vec{B}; \; \vec{F}_p(\vec{B}) = n_d\vec{f}_p.$$

For high temperature superconductors, when the temperature is close to the critical temperature T_c, the Hall effect is negligible compared to the Lorentz and pinning forces. At low temperature region, when applied current density $\vec{j}$ is much smaller than critical current density $\vec{j}_c$, the fluctuating force $\delta\vec{F}(T, \vec{B}, t)$ is also tiny and the driving force is balanced by the pinning force:

$$\vec{F}_p(\vec{B}) + \vec{j}_c \times \vec{B} = 0 \tag{2.7}$$

2.3.2 Flux creep and drastic avalanches

Equation 2.7 describes a stationary critical state and is metastable. This balance is time dependent and *flux creep* occurs due to the thermal activation or (2) by tunneling processes[39]. Such thermo-magnetic instabilities are triggered by either (1) applying an external magnetic field with a finite ramping rate which releases energy in the form

of heat and destroys the thermal equilibrium state, or (2) increasing the temperature to decrease the pinning force causes flux to move further inside of the superconductor sample[34]. Resulting finger-like patterns and more drastic avalanches were observed in many type-II superconductors such as $YBCO$, MgB_2 and Nb films from magneto-optical studies[32]. Such avalanches usually nucleate at sample edges where the local field is the largest. The timescale t_0 which is necessary to reach a nearly stationary state after suddenly switching on a magnetic field was given by:

$$t_0(x,y) \approx \frac{\mu_0 w^2}{2\pi\rho(x,y)}, \tag{2.8}$$

where w is the superconductor sample's half width and $\rho(x,y)$ is the flux creep resistivity. The timescale t_0 depends on the sample dimensions, sample geometry and the magnetic field ramping rate, and range from 10^{-5} seconds up to 10 seconds.

There are models based on the Maxwell equation and thermal diffusion equations to understand the thermal-magnetic instability phenomenons[40,41]:

$$\frac{\partial B}{\partial t} = -\nabla(B \times \nu);\ (E = B \times \nu). \tag{2.9}$$

The electric field in the superconductor is :

$$E = E_c e^{-U(j)/K_B T}, \tag{2.10}$$

where E_c defines the electric field level of the critical current density j_c,and the electric field E depends on $U(j)$ that is the current dependent activation energy $U(j)$ due to vortex pinning.

Instabilities occur not only due to a sweeping magnetic field. When a transport current is applied to the superconductor film, instabilities can be induced. The time

for developing to a quasi-stationary state is given by:

$$t_0 \approx \mu_0 w^2 \frac{j_c s}{E}, \tag{2.11}$$

where s represents the flux creep rate. Bobyl *et al*[28] calculated the current density distribution J with a magnetic field distribution $B(x,t)$ at any time t:

$$J(x,t) = \frac{2}{\pi\mu_0}\int_{-w}^{w} \frac{B(x',t) - B_a(t)}{x - x'}\sqrt{\frac{w^2 - x'^2}{w^2 - x^2}}dx' + \frac{I(t)}{\pi\sqrt{w^2 - x^2}}; \tag{2.12}$$

where $I(t)$ and $B_a(t)$ are the time - dependent total transport current and applied field, respectively. The calculation is based on a thin film sample geometry in which the magnetic field is perpendicular to the sample with a thickness much smaller than the half width w and much larger than the London penetration depth λ. From Bobyl *et al*'s report, the magneto-optical experimental results showed several 100 ms for relaxation times of pulsed transport currents in YBCO thin films and the flux creep led to a deeper flux penetration and a more uniform current distribution.

The real-time visualization of magnetic flux distribution by magneto-optical imaging technique gives direct observation of vortex dynamical behaviors in superconductors. Faster and more severe avalanches and flux jumps were studied in MgB_2 which is a very sensitive material to the dendritic instability. S. M. Hümmert studied the flux jump phenomenon of MgB_2 thin films at low temperature regions (below 10 K) in details in our laboratory[42], and reported that the finger-like patterns grow at various rates, some fingers develop faster and further into the film while others remain or grow wider instead of longer but the flux fingers avoid overlapping due to long range repulsive forces between vortices. Between these big finger patterns, there are small flux penetrations into the film. When the ramping magnetic field is high, large fingers swallow smaller ones. The flux penetration in MgB_2 thin film carries

the fingerprints of self-organized criticality and belongs to the same universality class of YBCO[43].

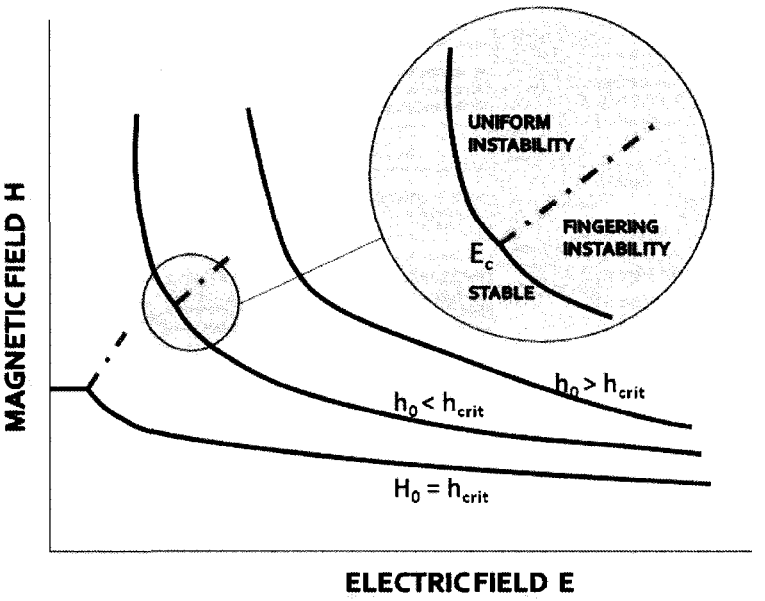

Figure 2.8: The instability diagram calculated by Denisov *et al* plotted in the $H - E$ plane[33].

Denisov *et al*[33] interpreted the appearance of the instabilities using a heat transfer rate h_0 and distinguished the instability regions in a $H - E$ (H is the magnetic field) diagram (Fig. 2.8) which claims that the instabilities depend strongly on the electric field E. Generally the onset of instabilities happens after the flux has moved inside of the sample, thus there is a few mT of a threshold magnetic field H_{th}. The critical electric field E_c depends on the sample thickness, the critical current density and the thermal conductivity.

2.4 The critical state model (CSM)

2.4.1 The original CSM for slab geometry

The critical state model, also called the Bean model, was introduced by Bean in 1962[44]. It gives a very simple assumption of the current density magnitude and distribution of type-II superconductors. The Bean model first assumes that when the applied magnetic field is significantly higher than H_{c1}, one obtains:

$$\vec{H} = \frac{\vec{B}}{\mu_0} \tag{2.13}$$

inside the superconductor; it also assumes the existence of a constant critical current density j_c that is independent of the local magnetic field $\vec{B}$ when the superconductor is in vortex state where $H_{c1} > H_a < H_{c2}$. In flux-free regions (Meissner region), the current density is zero.

In the original version of the critical state model, the assumptions are based on a slab sample geometry with a finite width and infinite length and height (Fig. 2.9). An magnetic field B_z is applied along the z direction. From Ampere's law:

$$-\frac{\partial B_z(x)}{\partial x} = \mu_0 J_y(x). \tag{2.14}$$

As the applied magnetic field increases, the flux continues to penetrate the bulk of the slab superconductor sample until a flux distribution reaches with $\left|\vec{J}(\vec{r})\right| \leq J_c$. The Bean model predicts that the current density equals to J_c wherever the flux is

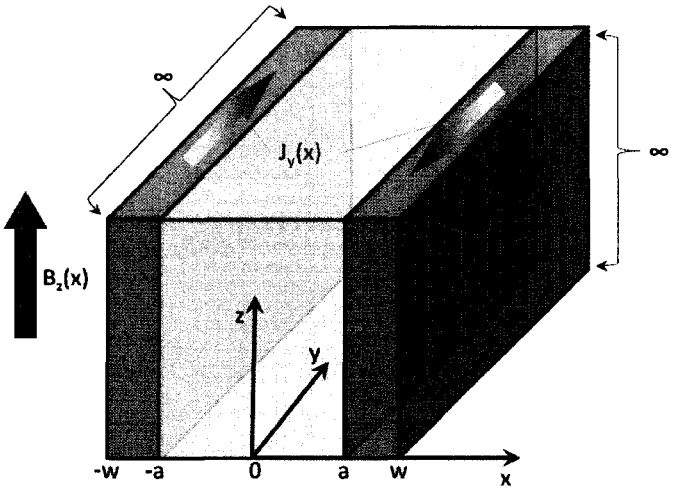

Figure 2.9: The slab sample geometry in the Bean model with infinite length and height. An external magnetic field is applied along the z direction. Flux penetrates the darker shaded regions $|w - a|$ where the current density stays constant and equals the critical current density j_c.

present and is zero in the sample center[45,46]:

$$J_y(x) = \begin{cases} J_c & \text{if } -w \leq x < -a; \\ 0 & \text{if } -a \leq x \leq a; \\ -J_c & \text{if } a < x \leq w. \end{cases} \tag{2.15}$$

Inserting the current density values into equation 2.14, the magnetic field distributions are[45] :

$$B_z(x) = \begin{cases} 0 & \text{if } -a \leq x < a; \\ \mu_0(|x| - a)J_c & \text{if } a \leq |x| \leq w; \\ B_a & \text{if } |x| > w. \end{cases} \tag{2.16}$$

As the applied field B_a increases to a saturated field $B_s = \mu_0 w J_c$, flux lines fully penetrate the bulk of the superconductor slab. Figure 2.10 (a) shows the magnetization curves in the Bean model after zero-field cooling. Figure 2.10 (b) shows the corresponding current density distribution. In flux free regions, there is no flux gradient present, the current density $j_y = 0$; when applied field $B_a = B_s$, the current is

flowing around the whole sample with a value of J_c.

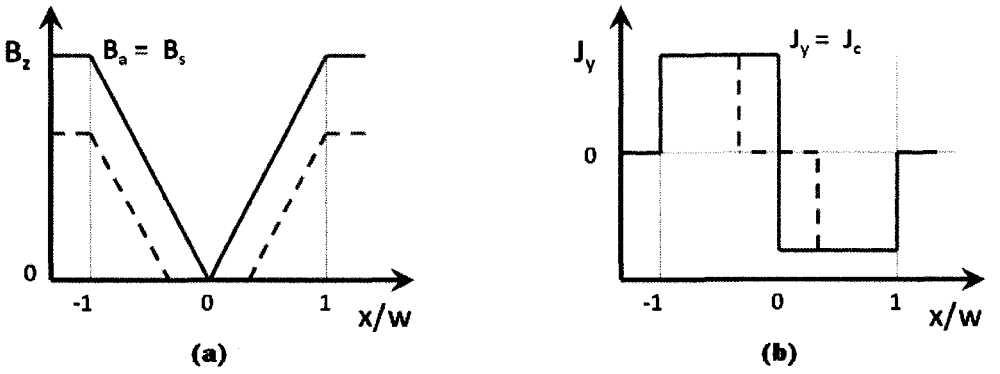

Figure 2.10: The magnetic flux density B_x (a) and the current density J_y (b) distributions across a slab in the Bean model at different values of applied magnetic field: $(B_a < B_s)$ - blue dotted lines, and $(B_a = B_s)$ - the olive-green solid lines.

The magnetization curve and the current density distribution of Fig. 2.10 are only valid with zero-field cooling. The sample's magnetic history changes when a magnetic field is applied without zero-field cooling. A change also occurs when the applied field increases from zero to a maximum value before returning to zero again. In both cases, the sample enters the remanent state with flux trapped inside the bulk.

2.4.2 Modified CSM for thin film geometry

The simple assumptions of the critical state model only works for a slab or a long cylinder sample geometry. For most realistic cases as in our experiment, the high temperature superconductor thin films have finite dimensions with a very small thickness d. Figure. 2.11 is a drawing of a thin film superconductor geometry. Comparing to Fig. 2.9, all parameters are identical except the infinite height is compressed down to a very small finite thickness d. In the thin film geometry, the thickness d is larger than the London penetration depth λ and much smaller than the sample half width w.

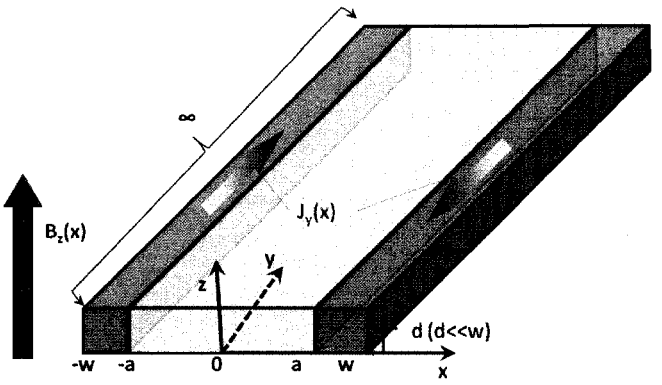

Figure 2.11: A thin film geometry of superconductor sample with infinite length and very small thickness, $\lambda << d << w$. The external magnetic field B_a is perpendicular to the thin film with strongly bent flux lines at the edges.

Only applying an external magnetic field

Applying an external magnetic field B_a along the z direction, the thin film superconductor expels the magnetic flux outside of the sample. Due to the very small thickness, the expelled flux lines are strongly bent around the sample edges and the x component of the applied magnetic field affect the overall magnetization thus cannot be neglected. Since in this geometry, the sample has infinite length, the current density j_y is one dimensional. One rewrites Ampere's law:

$$\mu_0 J_y(x) = \frac{\partial B_x}{\partial z} - \frac{\partial B_z}{\partial x}; \tag{2.17}$$

where the second term $-\frac{\partial B_z}{\partial x}$ is the new component contributing the current density of the thin film geometry. The essential assumption of the Bean model – the current density is equal to the critical current density J_c is still valid here.

In slab geometry, after vortices penetrate into the bulk, the outer regions have the current distribution $|J| = J_c$; in the flux free regions of the sample center, $J = 0$. For thin film superconductors, in the outer regions where vortices penetrate, the current distribution $|J| = J_c$ still holds but in the center region one needs to find a solution

for the current distribution J and magnetic flux density B.

In the central region $-a < x < a$, one can use conformal mapping method of images to obtain the current density $J_y(x)$[45,47]. As a result, the flux free sample center has a width $2a$ with :

$$a = \frac{w}{\cosh \frac{B_a}{B_f}}; \tag{2.18}$$

where B_f is a characteristic magnetic field for thin films:

$$B_f = \frac{4}{c} d J_c. \tag{2.19}$$

Therefore, the analytic expression for the current density in the flux free region of a thin film sample is:

$$J_y(x) = \begin{cases} J_c & \text{if } -w \leq x < -a; \\ -\frac{2J_c}{\pi} \arctan\left(\frac{x}{w}\sqrt{\frac{w^2-a^2}{a^2-x^2}}\right) & \text{if } -a \leq x \leq a; \\ -J_c & \text{if } a < x \leq w. \end{cases} \tag{2.20}$$

The transverse component of the magnetic field of the thin film is calculated from the above current distribution using the Biot-Savart law:

$$B_z(x) = B_a + \frac{2d}{c} \int_{-w}^{w} \frac{J_y(t)}{t-x} dt. \tag{2.21}$$

Solving the integral, one finds the magnetic field distributions[45]:

$$B_z(x) = \begin{cases} 0 & \text{if } -a \leq x \leq a; \\ \frac{4}{c} d J_c \ln \frac{|x|\sqrt{w^2-a^2}+w\sqrt{x^2-a^2}}{a\sqrt{|x^2-w^2|}} & \text{if } |x| > a. \end{cases} \tag{2.22}$$

Applying a transport current

It is important to study the transport behavior of HTSC because these types of superconductors often work well with a heavy load of transport current applied within a perpendicular magnetic field. This is also the case in our time-resolved MOI experiment. Calculating the critical state model for a thin film geometry sample with both external transport current I_T and perpendicular magnetic field B_a applied gives further quantitative analysis of MO images a good guideline.

When a transport current I_T is flowing along the y direction in a thin film superconductor, it will generate a self-field around the thin film. This self-field has opposite signs along the z direction at each sample edge. The conformal mapping method can solve the current distribution $J_y(x)$:

$$J_y(x) = \frac{I_T}{\pi d\sqrt{w^2 - x^2}}, \quad -w < x < w; \tag{2.23}$$

which corresponds to the magnetic field distribution:

$$B_z(x) = -\frac{2xI_T}{c|x|\sqrt{x^2 - w^2}}. \tag{2.24}$$

Figure 2.12 shows plots of the magnetic field $B_z(x)$ and a shielding current distribution $J_y(x)$ when there is only an external field B_a applied to the thin film. Different values of the applied field B_a are displayed in the figure. As the field increases, the flux free region width decreases. From the current density distribution plot, one finds that at sample edges, the current flows at a constant value of J_c as assumed in the Bean model, and changes its sign on the other edge.

To calculate the total current distribution $J_y(x)$ with both a transport current and an external field applied, one can obtain the shielding current distribution J_{iy} from equation 2.20 in the flux free region $(-a, a)$, which is equal to the current carried

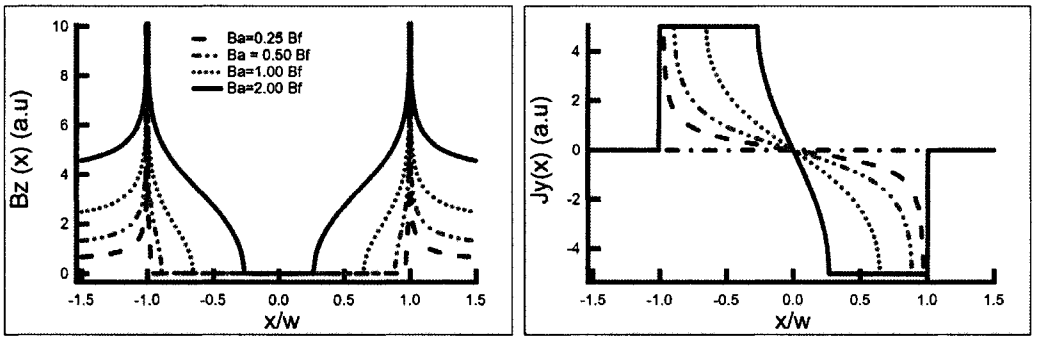

Figure 2.12: The magnetic field and current density distributions in a thin film geometry sample with different values of a perpendicular applied field B_a calculated from the modified critical state model.

by the critical region. The sum of the shielding current and the transport current density is the total current density[45,48]:

$$J_y(x) = \begin{cases} \frac{2J_c}{\pi} \arctan\left(\sqrt{\frac{w^2-a^2}{a^2-x^2}}\right) & \text{if } -a < x < a; \\ J_c & \text{if } a \leq x < w. \end{cases} \tag{2.25}$$

and the half width of the flux free region is

$$a = w\sqrt{1 - \left(\frac{I_T}{I_c}\right)^2}; \tag{2.26}$$

where I_c is the critical current of the thin film, $I_c = 2dwJ_c$.

Similarly, one obtains the total magnetic field distribution with both a current and a field applied to the film[45]:

$$B_z(x) = \begin{cases} 0, & \text{if } -a \leq x \leq a; \\ \pm\frac{4}{c}dJ_c \ln\frac{\sqrt{w^2-x^2}}{\sqrt{w^2-a^2}-\sqrt{x^2-a^2}} & \text{if } a < |x| < w; \\ \pm\frac{4}{c}dJ_c \ln\frac{\sqrt{x^2-w^2}}{\sqrt{x^2-a^2}-\sqrt{w^2-a^2}} & \text{if } |x| > w. \end{cases} \tag{2.27}$$

At the sample edges, the magnetic field distribution B_z has positive sign when $x < 0$, and vice versa. Figure 2.13 shows the transport current distribution when there is no

external field applied to the thin film sample. Different magnitudes of the transport currents are plotted from $I_T = 0.1J_c$ to $I_T = 0.8J_c$.

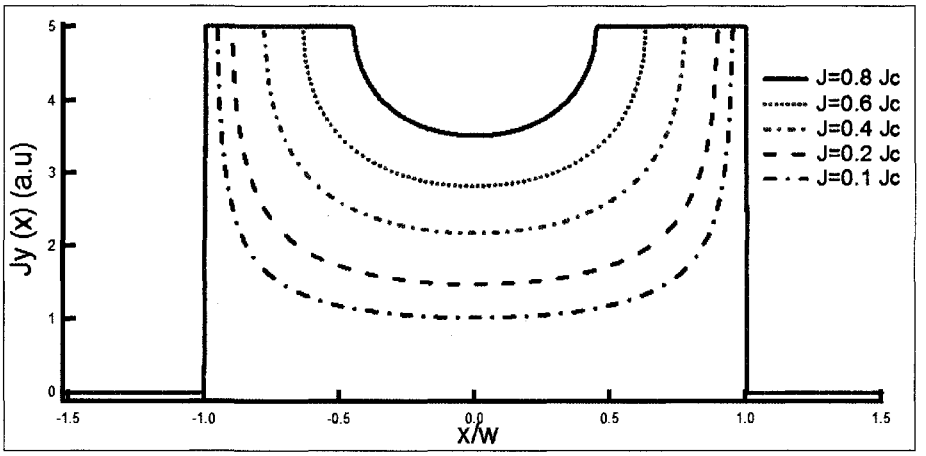

Figure 2.13: The transport current distribution in a thin film with different values of transport current flowing along the y-direction.

The current distribution model of eq. 2.25 is subject to remanence effects and will lead to non-zero magnetic field distributions in the sample center, which should be the flux-free region physically. An improved current distribution that creates zero magnetic field inside the sample is introduced to represent the transport current:

$$J_{y(new)}(x) = \frac{I_T}{\pi\sqrt{w^2 - x^2}}, \tag{2.28}$$

which is plotted in Fig. 2.14 with different values of the applied current I_T[47,49].

Note that these new current density profiles no longer follow the constant J_c assumption of the Bean's critical state model, while it has singularities at the sample edges $|x| = w$. However, this distribution is more realistic compared to the experimental data thin film superconductors obtained by magneto-optical imaging. The sum of eq.2.28 and the shielding current in eq.2.20 represents the new total current distributions, which are plotted in Fig.2.15. It is clear that with the new current distribution profiles corresponding to a new magnetic field distribution profiles no

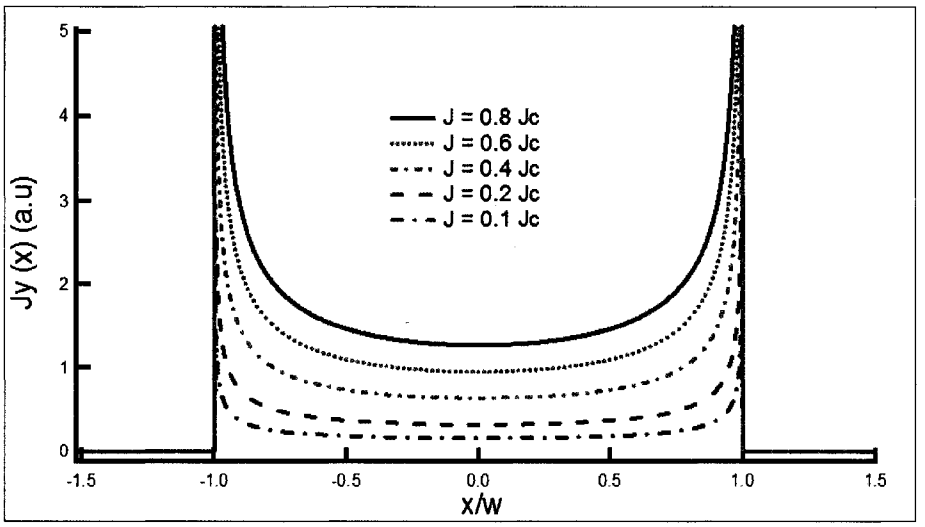

Figure 2.14: The new transport current distribution considering a more realistic physical case, which does not create magnetic flux in the flux-free region in the thin film sample center. Different values of the applied currents from $I_T = 0.1I_c$ to $I_T = 0.8I_c$ are shown.

flux are induced in the sample center.

When both the transport current and the magnetic field are applied to a film, the transport current will then create a self-shielding field around the thin film edges, whose z-components have opposite signs at each sample edge. The applied perpendicular magnetic field is fixed at one direction, thus the self-field induced by the transport current will either add or subtract the total field distributions. Such effect is pronounced when a large transport current is applied as indicated in Fig. 2.15. When a large transport current is flowing in the thin film, the self-field can be strong enough to invert the total magnetic field direction as shown in the top figure of 2.15, when $I_T = 1.5I_c$.

2.4.3 The finite element model (FEM) based simulation

The FEM model uses the direct magnetic field formulation without the use of vector or scalar potentials and relies on first order edge finite elements[50]. The governing equations are Maxwell equations and the superconducting material is described by

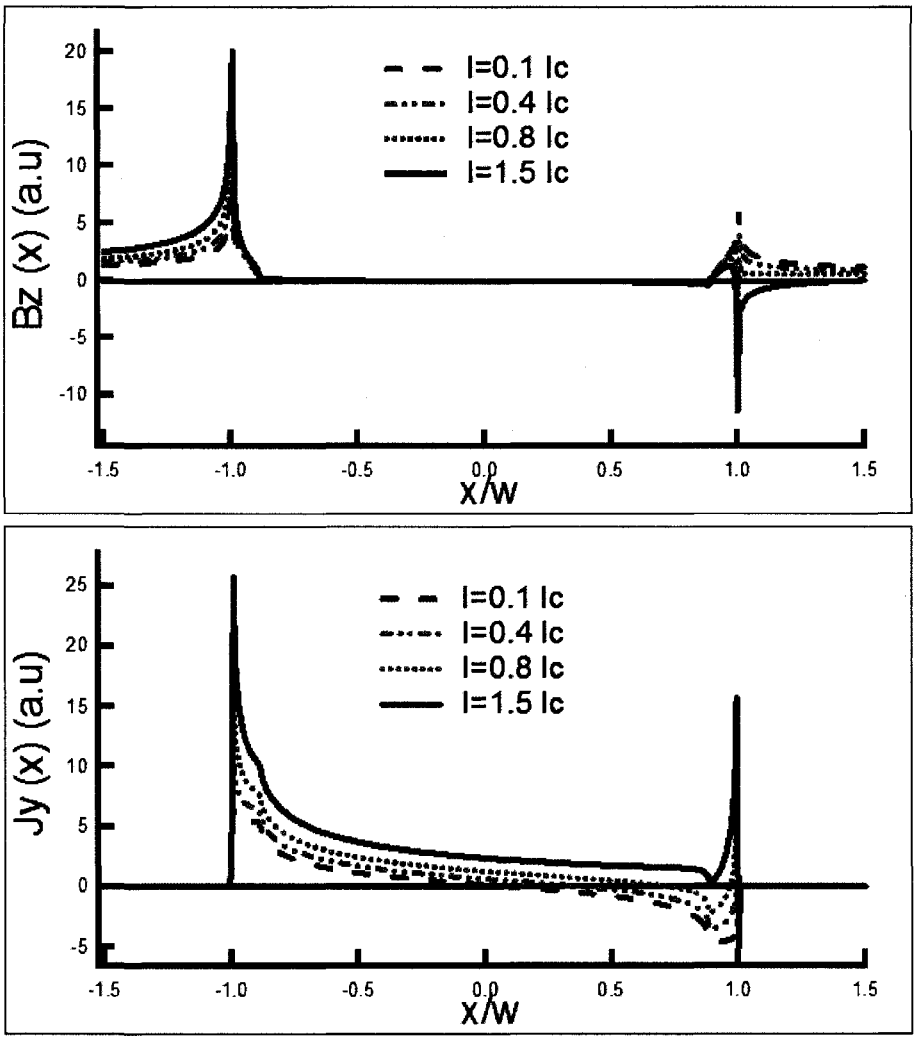

Figure 2.15: The magnetic flux density profiles (top) and the new total current distributions (bottom). The applied transport current varies from a low value $I_T = 0.1I_c$ to a large load $I_T = 1.5I_c$.

means of a non-linear $E-J$ characteristic which takes into account the transition from superconducting to normal state. The resistivity of the superconducting is expressed as:

$$\rho = \frac{E_c}{J_c}\left|\frac{J}{J_c}\right|^{n-1}, \tag{2.29}$$

where E_c is the critical electrical filed, J_c is the critical current density and n is the power index defining the steepness of the transition. For YBCO thin film, such as the sample we study in chapter 4, we use $E_c = 10^{-6} V cm^{-2}$, $J_c = (1.7 - 2.2) \times 10^7 A cm^{-2}$ at $T = 24$ K and $n = 19$. The non-linear dependence of current and electric field relation of Eq. (2.29) is determined by the thermally activated flux creep. The value of the exponent n is related to the ratio between the thermal energy and the flux pinning potential $U_0 = 40$ meV[51].

2.5 Inversion of the Biot-Savart law

To determine the current density distribution from the field from the map of the magnetic field that obtained from the MOI images. In the inversion procedure, the YBCO is considered as the thin film geometry, in which the current flows along the $y-$axis producing a B field in the $x - z$ plane. The thickness of the thin film t is much smaller than the distance to the plane of observation h (the distance between the indicator and the sample), we treat the current as one dimensional and described by a sheet current[52]:

$$J(x) = \int_0^t j(x,z)dz, \tag{2.30}$$

where $j(x,z)$ is the local current density. From the Biot-Savart law, the total perpendicular field[28,53]

$$\vec{B}(\vec{r},t) - \frac{\mu_0}{4\pi}\int_V \vec{J}(\vec{s},t) \times \frac{\vec{r}-\vec{s}}{|\vec{r}-\vec{s}|^3} d\vec{s} \tag{2.31}$$

can be reduced to an expression of[46]

$$\vec{B}(x') = \frac{\mu_0}{2\pi}\int_{-\infty}^{\infty}\frac{x-x'}{h^2+(x-x')^2}\vec{J}(x)dx. \tag{2.32}$$

To invert the Biot-Savart law, we use the convolution theorem to rewrite the current as :

$$\mu_0 J(x) = \int_{-\infty}^{\infty}\frac{\tilde{B}(k)}{\tilde{G}(k)}e^{ikx}dk, \tag{2.33}$$

where $\tilde{B}(k)$ and $\tilde{G}(k)$ are the Fourier transforms of the field profile and integral kernel, respectively. From $\tilde{G}(k) = \frac{\tilde{B}(k)}{\tilde{K}(k)}$, one obtains the current distribution through an inverse Fourier transform:

$$\vec{J}(x) = \nabla \times z\vec{G}(x). \tag{2.34}$$

The discrete numerical inversion of the Biot-Savart law is given[46,52]:

$$\begin{aligned}\mu_0\vec{J}(n) = \sum_{n'}\frac{n-n'}{\pi}\Bigg\{&\frac{1-(-1)^{n-n'}e^{\pi d}}{d^2+(n-n')^2}\\ &+\frac{[d^2+(n-n')^2-1][1+(-1)^{n-n'}e^{\pi d}]}{[d^2+(n-n'+1)^2][d^2+(n-n'-1)^2]}\Bigg\}\times\vec{B}_z(n').\end{aligned} \tag{2.35}$$

To simplify and reduce the computer's calculation time, we can discretized the integral of function (2.32) on a grid of N points x_n, corresponding to the number of pixels in a profile:

$$\vec{B}_z(x_m,h) = \frac{\mu_0}{2\pi}\sum_{n=0}^{N}\frac{\vec{J}_y(x_n)(x_m-x_n)}{(x_m-x_n)^2+h^2}\Delta x, \tag{2.36}$$

where Δx is the distance corresponding to the width of one pixel. The integral kernel,

which consists solely of geometric terms, is a square matrix of the size $N \times N$:

$$(M)_{m,n} = \frac{x_m - x_n}{(x_m - x_n)^2 + h^2}\Delta x. \tag{2.37}$$

Thus the discrete Biot-Savart law is rewritten as a matrix equation, where the discrete magnetic field line profiles and the current density are vectors with dimension N:

$$\vec{B}_z = \frac{\mu_0}{2\pi}\vec{M} \cdot \vec{J}(y). \tag{2.38}$$

Simply by inverting this matrix (2.38), one obtains the current distribution. The matrix can be inverted if for all m and n, the diagonal elements of $\vec{M}$ are non-zero:

$$\vec{J}(y) = \frac{\mu_0}{2\pi}\vec{M}^{-1} \cdot \vec{B}_z. \tag{2.39}$$

We use the magneto-optical technique to measure the magnetic field profiles of high temperature YBCO thin film superconductors, and by inversion of the Biot-Savart law, the current distribution profiles can be obtained. The detailed experimental procedures are discussed in the next chapter.

Chapter 3

Experiment

Chapter 3 describes time-resolved magneto-optical imaging (TRMOI) in detail. The basic physical principle for this advanced and unique TRMOI technique is the Faraday effect; as such, it is introduced early in the chapter. The chapter then moves from theoretical background to an overview of the experimental setup. A walk-through of the standard experimental procedure is presented with special attention given to thin film samples; including preparation and mounting. I conclude the chapter with a discussion of the magnetic field calibration procedure from magneto-optical (MO) images.

3.1 Time-Resolved magneto-optical imaging

3.1.1 Introduction to TRMOI

Magneto-optical Imaging (MOI) is a technique used to directly observe magnetism with naked eyes in real-time. The physics principle to support this phenomenon is called *Faraday effect*, which is, in brief, an interaction between light propagating in a material and a magnetic field. As Fig. 3.1 shows, if one sends linear polarized light

through a Faraday active crystal, which is mostly optically transparent dielectric material, while simultaneously applying a magnetic field along the propagation direction of the light beam, then the polarization direction will rotate slightly inside the crystal under the magnetic field's effect.

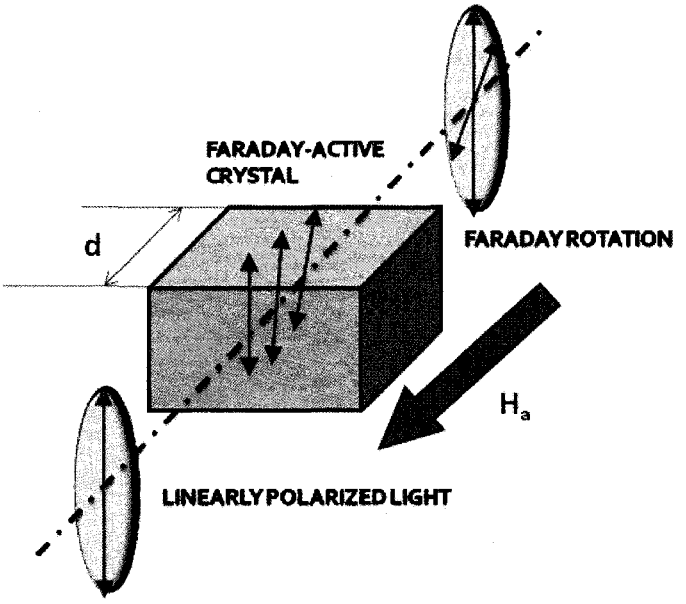

Figure 3.1: The Faraday Effect.

The rotation of the polarization direction is proportional to the magnitude of the magnetic field component parallel to the direction of the light beam. Variations in the intensity of the light allow us to observe the behavior of the magnetic field.

The Faraday effect results from the optical circular birefringence of the indicator crystal that affects the propagation of the two (left and right) circularly polarized components of the linearly polarized light. The two rays recombine with a phase offset in the propagation speed, resulting in a rotation angle of the linear polarization. Such rotation is proportional to the z-component (here the direction in which the light propagates) of the local magnetization of the material. A simple math equation describes the relationship between the angle of rotation of the polarization and the magnetic field:

$$\beta = VBd \tag{3.1}$$

where β is the Faraday rotation angle, B is the applied magnetic field, d is the length light travels inside the crystal and V is called *Verdet constant* that is related to the material itself.

In this thesis, I intend to measure two-dimensional magnetic flux density distribution of high temperature superconductor thin film samples. A YBCO superconductor thin film produces no significant Faraday effect, thus an indicator as a promisng magneto-optical recording medium is required in the setup. I choose a single crystalline iron garnet thin film $(Y, Bi, Pr, Lu)_3(Fe, Ga)_5O_{12}$. This film is ferrimagnetic with an in-plane magnetization M_s[54,55], which has an excellent magneto-optical effect.

The indicator's structure is illustrated in Fig. 3.2. The indicator layer is grown on a 4 μm thick $Ga-Gd$ garnet substrate layer, underneath which is a reflective layer, and at the bottom side of the thin film is a protective layer to avoid physical damage. This protective layer is crucial for getting clear MO images since the sample underneath normally has rough surface and a very tight contact to the sample scratches the indicator. The indicator shows a Faraday rotation of $1.08°/\mu m$ at an applied field $H_z = 750\ Oe$.

In addition to conventional MOI, we developed a time-resolved MOI technique, which allows us to take MO images at any phase point of an externally applied ac transport current. The time resolution we commonly use are 20 μs and 40 μs. By using TRMOI, we can study superconductor magnetic behavior not only in a magnetic field but also with an ac current applied. Next section presents the detailed experiment setup.

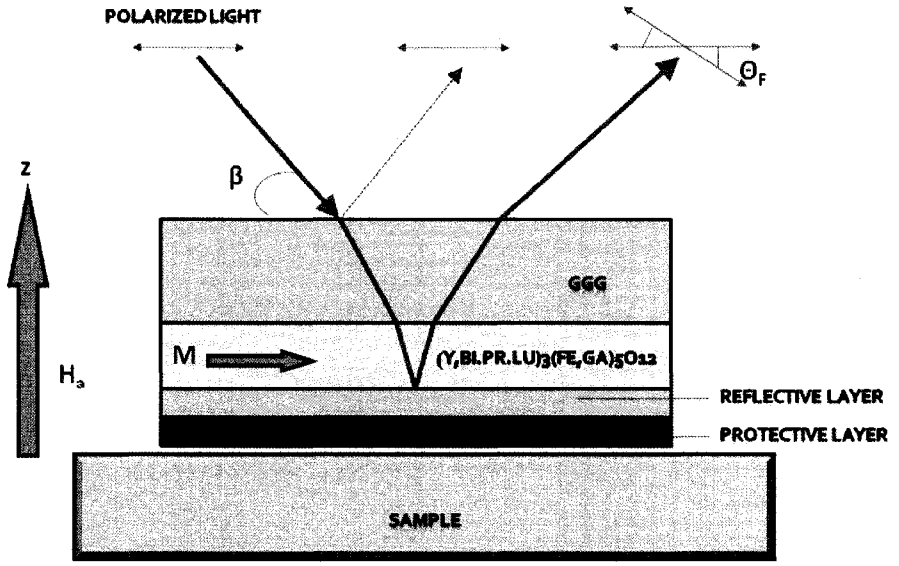

Figure 3.2: The iron garnet thin film magneto-optical indicator. Incident polarized light passes the indicator layer twice, and is rotated by an angle Θ_F that is proportional to the perpendicular applied magnetic field H_a.

3.1.2 Experimental setup

A magneto-Optical Imaging experimental setup usually involves light sources, a magnet, a pair of polarizer and analyzer, a microscope and other optical components, a image acquiring device and necessary electronics. Low temperature measurements for superconductors also need a cryostat and a vacuum.

In time-resolved MOI experiment, we take a series of time-resolved images to study magnetic field distribution in YBCO thin film with an applied ac current. Some additional device such as an ac current power source synchronized to the light source is included in order to take images at different phases of the ac transport current.

A schematic drawing of the TRMOI experiment is shown in Fig. 3.3. Polarized laser pulses are synchronized with the ac transport current at the same frequency. This stroboscopic method yields MO images at specific phase points of the alternating current, and between two phases no light will illuminate the indicator thus no image

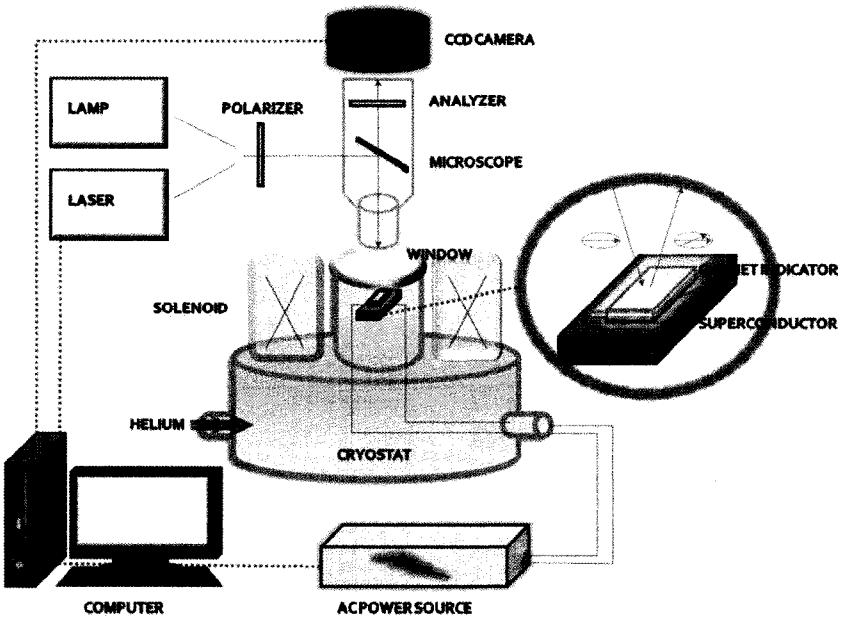

Figure 3.3: Schematic of the time-Resolved Magneto-Optical Imaging setup . Both a mercury-vapor lamp and a laser are available light sources for the MOI experiment. TRMOI requires a laser synchronized to an ac current power source.

is taken. No light between the laser pulses reaches the indicator. A series of time-resolved images that only containing the magnetic field distribution information at each phase point thus successfully obtained .

More detailed descriptions of each component are given below:

Microscope

The polarizing microscope is custom-assembled using components from Olympus. It is equipped with a Glan-Thompson polarizer and a linear polarizer providing an extinction ratio of 10^{-5}. The polarization angle of the analyzer to the polarizer is adjustable. Images taken slightly out of cross polarization will enhance the range of positive and negative field extinction but compromise the image's contrast. We normally set the polarization 2 5° out of cross polarization configuration. This off-cross polarization setting is further discussed in Section.3.3. The microscope can

mount different objectives that range from a 4× up to a 20×. A 4× objective is used to take overview MO images of the whole sample, and for higher resolution requirement, we use a 10× objective. Higher magnification objectives increase resolution but at the same time reduce the field of view. The maximum spatial resolution, however, is limited by the distance between the indicator and sample surface more than the optics.

Light Sources

As shown in Fig. 3.3, two different light sources are used: a mercury-vapor lamp or a laser. As mentioned before, in time-resolved MOI measurements, we need to use a laser to be synchronized to an ac current power source. In our work, a Q-switched Nd:YLF diode-pumped solid-state laser provides 100 ns short pulses at $\lambda = 527$ nm wavelength with pulse width $\tau = 100$ ns. For synchronization to the frequency of the ac current, the laser pulse repetition frequency is varied from single shot up to 1200 Hz by an externally triggered Pockels Cell.

Externally trigged laser light pulses are coupled into an optical fiber, which is connected to a custom-built telescope, that collimates the highly divergent laser beam coming out from the optical fiber. The images quality is related to the intensity and homogeneous distribution of the light. The telescope profile shapes the divergent light beam into parallel (slightly divergent) and more homogeneous. Passed the telescope, the laser beam travels through a beam splitter of the microscope, then goes through an objective and an optical window on top of the cryostat and illuminates the indicator. In order to avoid interference effects, due to the coherent laser light, most of the optical components requires anti-reflection coatings.

A second light source is a one watt mercury-vapor lamp , which is used for static MO measurements when no time resolution is needed. As a comparison, in static

MOI measurements, using mercury lamp light, MO images have worse contrast but do not have any interference patterns caused by the coherence of laser light. Also, mercury-vapor lamp takes very short time to achieve its maximum power and stable working status, however, depending on the room temperature or other environment issues, laser may take hours to warm up to get to desired output power and begin lasing stable pulses.

CCD Camera

On top of the microscope is a *Hamamatsu* ORCA-ER-1394 CCD camera[56] with high resolution format (horizontal 1344 pixels $\times$ vertical 1024 pixels), which is an effective area of 8.67 $\times$ 6.60 mm . The CCD offers very high quantum efficiency (Fig. 3.4) over a broad spectral range λ = 300 nm to λ = 850 nm and very low noise. The CCD camera has a 12 bit dynamic range gray scale. The camera is interfaced to a computer through the connector IEEE 1394 – 1995 in order to acquire images at the fastest frame rate of 8.8 frames/sec. Exposure time can be in a range of 10 μs to 1600 s.

In our measurements, exposure time is varied from 5 ms to 200 ms, depending on the laser pulse repetition frequency and the laser's working condition. Lower frequency means less laser pulses will reach the chip thus lower light intensity per unit time. To achieve same brightness as higher frequency images, longer exposure time is required. Sometimes, running on the same pump current, the laser output power may vary. Adjusting the camera's exposure time accordingly provides comparable brightness MO images. The recorded images are either manually or automatically saved to a computer hard disk. Images are preferred to be saved as tag image file format(.tiff) with no compression, other than a commonly used method of compression for photographic images as JPEG, for further quantitatively analysis without losing

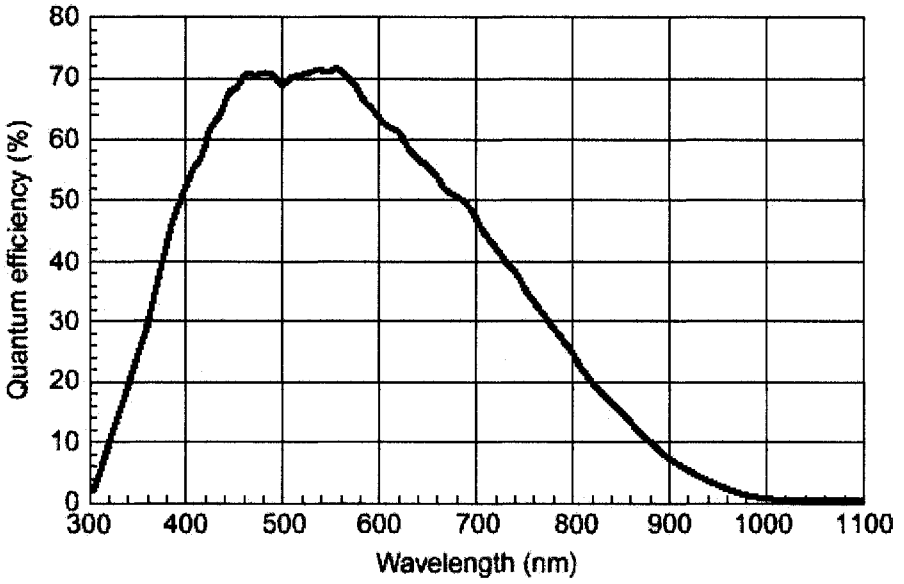

Figure 3.4: Hamamatsu ORCA-ER-1394 CCD camera spectral sensitivity. At a laser light wavelength $\lambda = 527$ nm, the camera has an approximately 70% quantum effciency.

any information. Each MO image has a resolution of 1344×1024 pixels and about 4 megabytes in size. Many series of TRMO images of a measurement can accumulate up to gigabytes, thus a large and fast hard disk partition is required for this experiment.

For the largest view, a demagnifying adapter with a demagnification of $0.63\times$ is available. After spatial calibration in this configuration, each pixel equals to 2.494 μm in length, and a resulting field of view is 3.35×2.55 mm. The sample size determines whether to use a $0.63\times$ adapter or an ordinary $1\times$ adapter.

Cryostat and Vacuum

The superconducting thin film sample is mounted on a cold finger of a continuous flow liquid helium cooled cryostat with temperature range of 3.5 K to 425 K. YBCO has a critical temperature of 92 K, above liquid nitrogen boiling temperature. However, at lower temperature, signals are stronger and images have much better contrast and homogeneity. We take the images in the range of 10 K to 45 K. Studying magnetic behavior close to critical temperature is more challenging and also important.

Before cooling down the cryostat using liquid helium flow, the cryostat needs to get pumped down to a vacuum of 10^{-5} Torr. To meet such demands for high throughputs with high ultimate vacuum, we use a RV series 3 *Edwards* dual-mode vacuum pump which allows the user to easily configure the unit to pump very high gas loads and achieve excellent vacuum - from a single pump, and a turbo molecular pump to provide reliable, hydrocarbon-free, high and ultra high vacuum. To reach a stable vacuum level of 10^{-5} torr from atmosphere pressure (1 atm = 760 torr), it usually takes 12 to 24 hours depending on the degassing of vacuum chambers.

Magnet

An electromagnet with magnetic field from -65 mT to 65 mT is mounted on the cryostat so the magnetic field is perpendicular to the MO indicator plane. Slight adjustment of the magnet's vertical position ensures that the superconductor thin film is at the center of the solenoid and only the smallest amount of x and y direction magnetic field will go through the sample, which would influence the in-plane magnetization of the indicator film and reduce the response for an applied magnetic field. Although the in-plane magnetization cannot be totally avoided, it is reported as a factor while calculating the magnetic field distribution. Note that when operating the electromagnet over ± 40 mT, water circulating cooling is needed.

Synchronization Unit

A synchronization unit was custom-built for this work (Fig. 3.5. An ac power source sends an ac current I through a load resistor R connected to the superconductor sample. The ac signal from the resistor R is the input signal to the synchronization circuit, and also displayed on an oscilloscope. The output signal sends a trigger pulse to the laser with a finely controllable time delay Δt with respect to the phase of the

ac current signal.

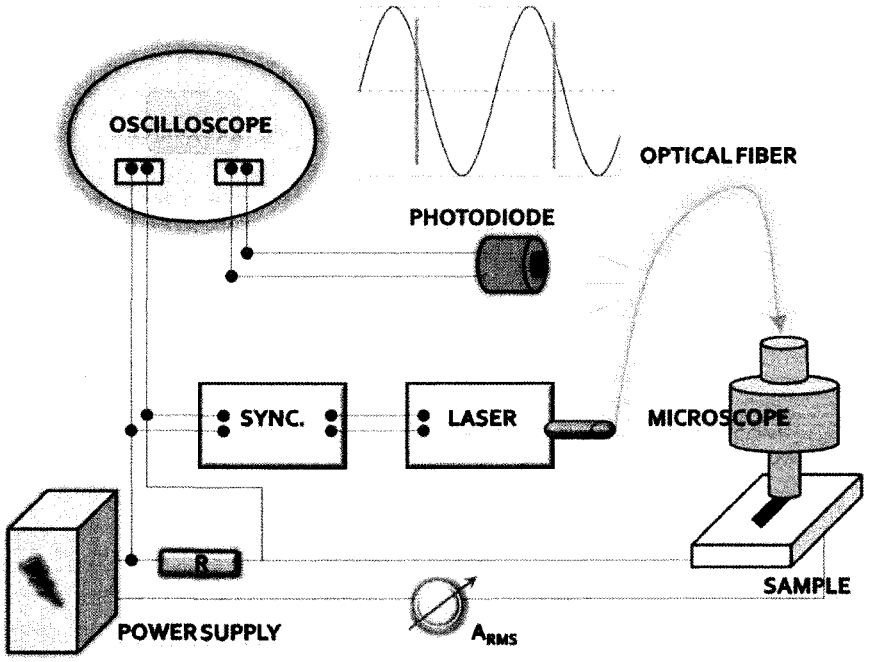

Figure 3.5: The synchronization scheme. The phase of ac current at which pulses are triggered is adjusted by a synchronization circuit. Laser pulses sensed by a photodiode are displayed on an oscilloscope with the ac current signal. The inset shows how laser pulses (green spikes) are synchronized with a ac current (blue sine wave)

The externally rigged laser generates pulses coupled into an optical fiber. A photodiode is used to detect the laser pulses which are then also displayed on the oscilloscope screen. By adjusting the overlap of the laser pulse spikes with the ac current wave on the screen, one can easily control any synchronization phase point.

3.2 Experimental procedures

3.2.1 Sample preparation and mounting

$YBa_2Cu_3O_{7-\sigma}$ (YBCO) high temperature superconductor thin film samples are grown by pulsed laser deposition (PLD) on a $LaAlO_3$ or $SrTiO_3$ substrate with typical dimensions of 10 mm $\times$ 5 mm and a thickness of 250$-$300 nm. We keep the delicate and

fragile thin film samples sealed and storage in a vacuum desiccator. Tilted SEM pictures of the thin films show that the sample surface is rough on the superconducting side.

Before mounting a thin film onto the sample holder, the film's overall physical condition is carefully examined. Bare hands touching the films will contaminate the sample surface with grease, salt and other human skin excretion, thus it is prohibited. A plastic tipped tweezer will help a lot on picking up such small dimension films. Methanol is a good cleaner for some minor contaminants. In order to send a transport current into the superconductor, the sample has metal contacting pads on the substrate connecting to the superconducting bridge. Sometimes those metal pads are all over the substrate, and once the sample is mounted on the copper sample holder, it will cause a circuit shortage. One way to remove that extra metal contacting material is to use a sharp blade and extremely carefully scratch it off, then rinse it off in methanol, and wipe the sample with optical paper other than paper tissue or cotton balls to prevent fine fibers staying on the sample.

A clean thin film is now ready to be mounted on top of the sample holder. Check one more time the resistivity of the thin film to make sure that only between the two metal pads it is conducting and everywhere else it is insulated. Normally the electric resistivity of YBCO thin film's is 40 Ω to 90 Ω at room temperature.

A sample holder is custom-designed for this work (Fig. 3.6). A roughly quarter-sized, half-inch thick cylinder shaped copper sample holder is screwed on top of the cryostat cold finger. A rectangular shaped block on top of the cylinder has a slit in the center to fit in a Hall probe and a diode temperature sensor. A thin layer of indium foil is placed between the cold finger and the sample holder for good thermal conduction. This indium foil layer accelerates the cooling rate of the sample mounting area and greatly reduces the temperature difference between the cold finger and the

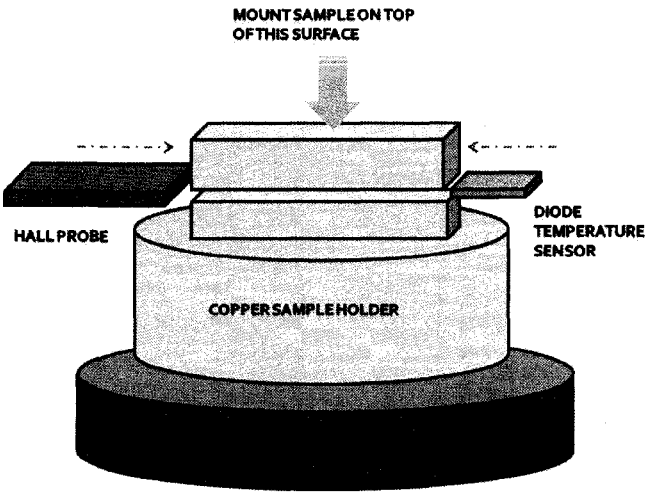

Figure 3.6: Custom designed sample holder mounted on top of the cold finger. A horizontal open slit 5 mm beneath the sample is for inserting the Hall probe and the diode temperature sensor.

sample.

The sample is glued right on top of the rectangular block. The thin film sample is glued with silver paint for excellent thermal conductivity and easily removing the sample after measurement is done. The thin layer silver paint needs to be applied evenly. Unevenly mounted film will cause part of the image taken out of focus and extra unwanted in-plane magnetization. Any excess silver paint contaminates the sample, and if it touches the metal contacting pads, the silver paint will cause shortage. Unsuccessfully glued sample can be redone by using acetone to wash off all the silver. Other low-temperature usable polymer glue is also an option.

A piece of MO indicator is mounted tightly on top of the glued thin film, as shown in Fig. 3.7. The indicator should be big enough to cover the superconducting bridge but not too big because we need the two metal contacting pads left uncovered for later to connect the sample to the ac circuit. The smaller the distance between the indicator and the sample, the higher the resolution and the better quality of the MO images. To mount the indicator on the sample, aluminum tape is cut into two thin

stripes (approximately 60 mm × 1 mm). The stripes are put over the indicator, pressed down onto the sample, and push firmly and evenly down along the side edges of the sample holder.

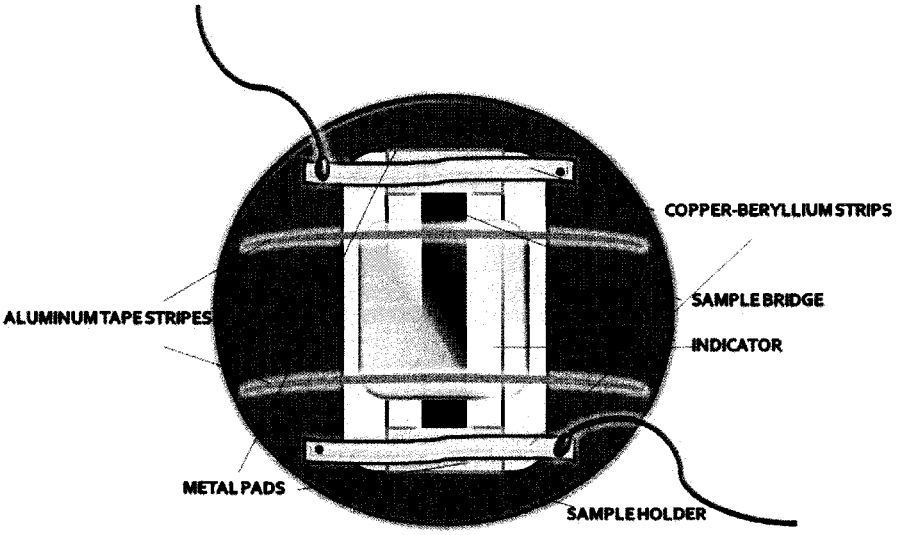

Figure 3.7: A top view of mounted sample on a sample holder.Telfon ring is excluded in this figure.

At this point, the static, no current applied MOI experiment can start. To do an ac current applied time-resolved MOI experiment, we use a pair of copper-beryllium stripes firmly touching on the metal pads to provide electrical contact to the thin film. This pair of metal stripes are screwed onto a teflon ring in order to insulate the metal stripes from the copper sample holder. A good sample contacting setup is established if there is electrical contact only between the two pads; no shortage with the sample holder or the cryostat; and the two stripes are tightly screwed into the sample holder in the condition of not over-stress the soft teflon ring, because at low temperature, due to the material contraction, electric contact is often lost. Fig. 3.7 is a top view scheme of the finished sample mounting.

A delicate sample preparation and a successful mounting are to ensure a successful measurement. This part of work represents a significant portion of the whole TRMOI

experiment.

The cryostat is then capped with a sapphire optical window and pumped to low vacuum. Next section describes a TRMOI experiment process walk-through.

3.2.2 TRMO imaging measurement

Liquid helium is used to cool down the system. Normally 5 to 20 liters of liquid helium are enough for one experiment. Before cooling down the system, we pump the cryostat to a vacuum level of at least 10^{-5} Torr, which requires at least 12 hours. Once the vacuum level is achieved, the YBCO thin film is zero magnetic field cooled down to 15 K. The cooling is down slowly and smooth to minimize thermal stresses and also reduce the risk of electric contact loss. At the same time, the Yd:YLF diode-pumped solid-state laser is warmed up. For our measurement, the desired laser output power measured after the optical fiber is 450 mW to 500 mW at PRF = 1000 Hz.

A small external magnetic field is applied at the beginning to center the view and adjust microscope to focus. The lens in the custom-built telescope can be moved slightly to improve light homogeneity. Once the sample is at the right position, the external field is turned off. The remanences in the sample are removed by raising up the temperature higher than 92 K the critical temperature of YBCO. When there is no more penetrated flux inside the sample, the system is cooled back to 15 K and the calibration measurement is started.

Integration of most of the devices and components into LabView makes the calibration measurement almost automatically done in a couple of minutes, and it also helps to reduce liquid helium consumption. The CCD camera's exposure time is properly set to avoid low contrast images at very low or very high applied magnetic fields. After calibration, the sample is reset to flux-free condition and the desired

TRMOI measurement is done at the same configuration.

In order to see more enhanced magnetic behavior of the superconductor under the effects of ac transport current, the external magnetic field normally is smaller than 20 mT. $B_a = 10$ mT is commonly used. the laser trigger is set to external to do transport measurements. The highest current is limited not only by the sample's critical current but also the load resistor R. Ac current phase dependence measurement is manually done. One has to adjust the synchronization delay time phase by phase by looking at the scope and taking images one by one. At high currents, the transport current may locally heat up the thin film sample and thus MO images will be blurry. If one does not pay extra attention to the temperature control, the superconductor will be burned.

At some phase point, the laser may loose or gain some pulses due to an instability, and the MO image will appear a lot darker or brighter than other phase points. One will have to re-take the data after the laser is stable again.

At the end of the measurement, when liquid helium flow is removed, the vacuum should be kept running and the system warms up naturally.

3.3 Magnetic field calibration from images

When a perpendicular magnetic field is applied to the indicator, the magnetization is rotated out of plane by an angle

$$\phi = \arctan \frac{B_z}{B_k} \tag{3.2}$$

where B_z is a perpendicularly applied magnetic field, B_k is the indicator film's magnetic anisotropy field. The Faraday rotation angle Θ_F of the incident polarized light

is proportional to the magnetization:

$$\Theta_F = cM_s \sin\phi = cM_s \sin\left(\arctan\frac{B_z}{B_k}\right) \tag{3.3}$$

The MO images are recorded with a CCD camera through a polarized microscope. Inserting Eq. 3.3 into Malus's law:

$$I_{out} = I_{in} \sin^2\alpha \tag{3.4}$$

one obtains[24,35]:

$$I_{out} = I_{in} \sin^2\Theta_F = I_{in} \sin^2\left[cM_s \sin\left(\arctan\frac{B_z}{B_k}\right)\right] \tag{3.5}$$

where Malus's law describes the light intensity I_{out} transmitted by a polarizer when the incident light of intensity I_{in} is polarized at an angle $\frac{\pi}{2}+\alpha$ relative to the polarizer. Eq. 3.5 only applies when the pair of polarizers are at perfectly crossed polarization configuration. In realistic conditions, a background light intensity I_0 is considered, which is transmitted by non-perfect polarizers in the cross polarized position. Also for a larger scale of positive and negative magnetic field deviation, we would like to keep the two polarizers a few degrees $\Delta\alpha$ out of cross polarization. A new realistic equation of 3.5 now becomes:

$$I_{out} = I_{in} \sin^2\left[cM_s \sin\left(\arctan\frac{B_z}{B_k} + \Delta\alpha\right)\right] + I_0 \tag{3.6}$$

where I_{in} is the maximum light intensity that can be modulated with Faraday effect, which includes any light absorption in the indicator and in the polarizers. Images taken by the CCD camera are two dimensional intensity arrays $I_{out}(x, y)$. by analytically inverting Eq. 3.6 we obtain the magnetic flux density distribution formula[35,53]:

$$B_z(x,y) = B_k \tan\left\{\arcsin\left[\frac{1}{cM_s}\arcsin\left(\sqrt{\frac{I(x,y)-I_0}{I_{max}}}+\Delta\alpha\right)\right]\right\} \tag{3.7}$$

where $B_k, cM_s, \Delta\alpha, I_0$, and I_{max} are 5 parameters that need to be determined by fitting the experimental calibration curve (Fig. 3.8). Da in the figure is the off cross polarization angle $\Delta\alpha$ in radius.

The calibration for the magnetic flux density from light intensity measurement is done right before each new MO measurement. The experimental conditions such as temperature, indicator position and laser power should be the same for subsequent MO measurements.

To do the calibration, we first take a series of MO images by changing magnetic field, either from 0 mT to 60 mT or -60 mT with a step size of 1 mT after zero cooling the superconductor sample to 15 K. To obtain the calibration curve, light intensity values of regions in the images that are far away from the superconductor areas are averaged and plotted versus recorded magnetic field B_z. Using this curve to do a fitting of function 3.7, one obtains a fitting calibration curve and the 5 parameters, as shown in Fig.3.8.

Figure 3.9 is one of the ramping-up magnetic field calibration series images at $B_a = 40.21$ mT. Regions of interest for calibration are indicated in pink frames that are far away from the superconducting area (the dark centers of each filament). The image color table is stretched to enhance its contrast.

For frequency dependence measurements, while decreasing the laser frequency, the number of laser pulses reaching the CCD chip during the same exposure time period will decrease too. If the system is not calibrated for each frequency, a frequency correction is required to make sure the calculated magnetic field distribution

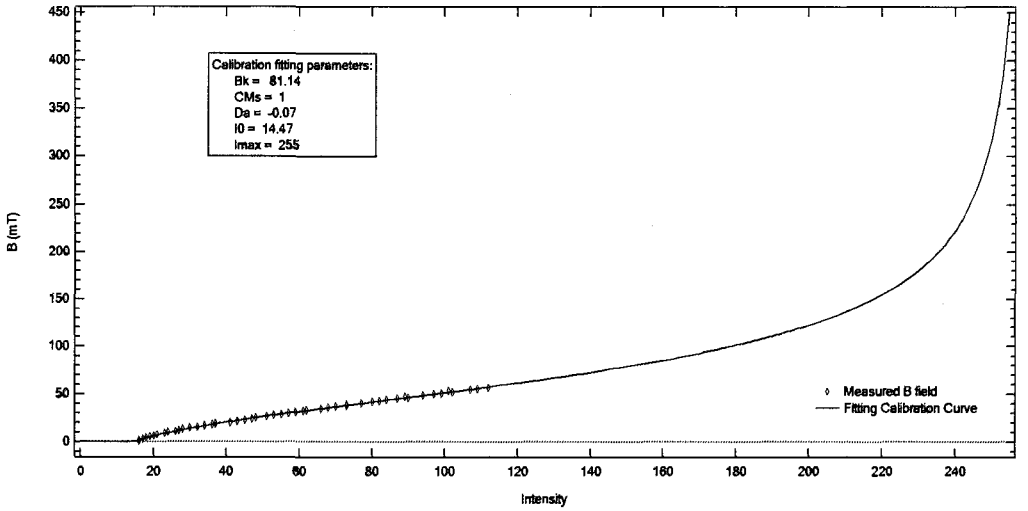

Figure 3.8: Calibration curve, measured points (Green markers) and a function 3.7 fitting curve (purple) at $T = 15$ K, laser PRF $f = 1000$ Hz, and the CCD camera exposure time $\tau = 30$ ms.

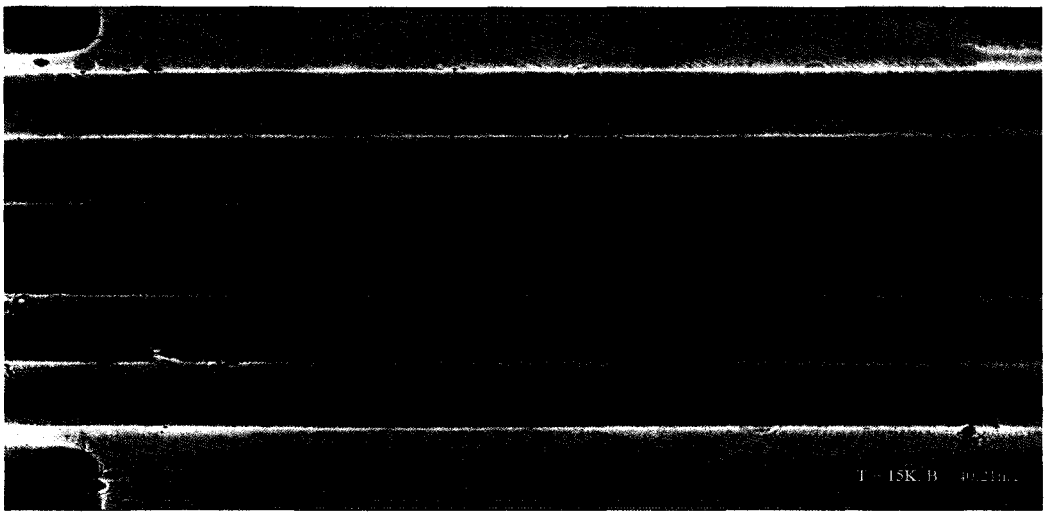

Figure 3.9: One sample calibration image of 6 filamentary YBCO thin film. The dark regions in the image shows where the superconducting filaments are, and the very bright lines are the edges of each filament. Chapter 5 presents a discussion of YBCO filamentary thin film.

is quantitatively correct.

Figure. 3.10 is a plot of the images' intensity as a function of the number of laser light pulses, which are obtained from the set of frequency images at the zero phase points of the ac current. This curve is used to determine a parameter ξ for the exposure time correction. The behavior is linear in an approximation with a background intensity $\xi \neq 0$, which justifies a phenomenologic equation:

$$I = f \cdot \tau \cdot s + \xi \tag{3.8}$$

where I is the image intenisty, τ is the exposure time and s is the intensity of one Faraday rotated laser pulse. By extrapolation to $f \cdot \tau = 0$, one can get a mean offset $\xi = 13.8 \pm 1.4$ from three such plots at the three phase points. Using the relation:

$$I_2 = \frac{f_2 \tau_2}{f_1 \tau_1}(I_1 - \xi) + \xi, \tag{3.9}$$

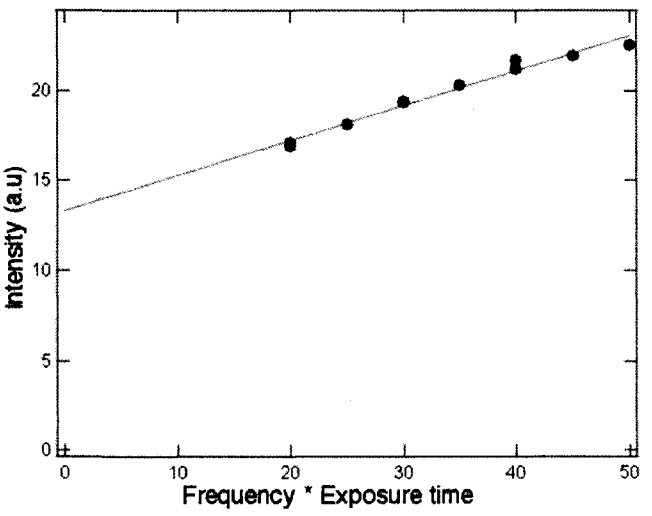

Figure 3.10: Intensity of MO images versus the number of collect light pulses.

one can convert the intensity profiles recorded at different frequencies to the highest frequency with the corresponding exposure time τ.

Extended Calibration

Figure 3.8 shows the measured calibration curve (points) from a YBCO multi-filamentary thin film and the fitting curve. I_0 is the lowest intensity value the CCD camera can record, and for the image in Fig. 3.8 $I_0 = 14.46$.

While doing the fitting to function 3.7, we constrain some of the parameters such as $I_{max} > 255$. Since in the following time-resolved MOI measurement, we keep a low applied magnetic field (less than 10 mT) to observe more of the effects of the ac transport current. The highest light intensity will not exceed 100.

Examining the lower intensity region of Fig. 3.8, the fitting curve of B_z is simply set to zero while $I \leq I_0$. This is not true because from function 3.7, while at out of cross polarization, $\Delta\alpha \neq 0$, if $I \leq I_0$, the magnetic field $B_z \neq 0$. The smaller the absolute value of $\Delta\alpha$ is, the shorter will be the range of the negative part of B_z.

We consider the magnetic flux density B_z now. Would it be negative? Yes, one can easily change the applied field direction to change the sign of it. We would expect the magnetic flux to change sign when the ac current changes phases, and thus the direction of flow, especially while applying a very small external field. However, this little part of negative values of B_z from Fig. 3.8 is not enough for a complete magnetic field calibration.

To find the correct negative field calibration curve, we first invert the calibration equation 3.7 back to Malus's law expression. Considering only physical case when $I_{x,y} \geq I_0$, inverting

$$B_z(x,y) = B_k \tan\left\{\arcsin\left[\frac{1}{cM_s}\arcsin\left(\sqrt{\frac{I(x,y)-I_0}{I_{max}}}+\Delta\alpha\right)\right]\right\}$$

one obtains:

$$I(x,y)_1 = I_0 + I_{max}\left(\sin\left[\frac{cM_sB_z}{\sqrt{B_k^2+B_z^2}}\right] - \Delta\alpha\right)^2 \tag{3.10}$$

$$I(x,y)_2 = I_0 + I_{max}\left(-\sin\left[\frac{cM_sB_z}{\sqrt{B_k^2+B_z^2}}\right] - \Delta\alpha\right)^2 \tag{3.11}$$

Simply plug in the measured calibration data into Eq. 3.10 and 3.11, we easily fit our experiment well with equation 3.10 thus it is the real root of the inversion. The variable of function 3.10, B_z, could be any real number and thus shows a full inverted calibration curve.

Next, we invert Eq. 3.10 to find the final calibration curve B_z vs I in which positive intensity could correspond to a negative field. This inversion result in the following four B_z expressions:

$$B_{z1} = \frac{B_k \arcsin\left[\Delta\alpha - \frac{\sqrt{I_{max}(I_{x,y}-I_0)}}{I_{max}}\right]}{\sqrt{cM_s^2 - \arcsin\left[\Delta\alpha - \frac{\sqrt{I_{max}(I_{x,y}-I_0)}}{I_{max}}\right]^2}}, \tag{3.12}$$

$$\mathbf{B_{z2}} = \frac{\mathbf{B_k}\arcsin\left[\boldsymbol{\Delta\alpha} + \frac{\sqrt{\mathbf{I_{max}(I_{x,y}-I_0)}}}{\mathbf{I_{max}}}\right]}{\sqrt{\mathbf{cM_s^2} - \arcsin\left[\boldsymbol{\Delta\alpha} + \frac{\sqrt{\mathbf{I_{max}(I_{x,y}-I_0)}}}{\mathbf{I_{max}}}\right]^{\mathbf{2}}}}, \tag{3.13}$$

$$B_{z3} = -\frac{B_k \arcsin\left[\Delta\alpha - \frac{\sqrt{I_{max}(I_{x,y}-I_0)}}{I_{max}}\right]}{\sqrt{cM_s^2 - \arcsin\left[\Delta\alpha - \frac{\sqrt{I_{max}(I_{x,y}-I_0)}}{I_{max}}\right]^2}}, \tag{3.14}$$

$$B_{z4} = -\frac{B_k \arcsin\left[\Delta\alpha + \frac{\sqrt{I_{max}(I_{x,y}-I_0)}}{I_{max}}\right]}{\sqrt{cM_s^2 - \arcsin\left[\Delta\alpha + \frac{\sqrt{I_{max}(I_{x,y}-I_0)}}{I_{max}}\right]^2}}. \tag{3.15}$$

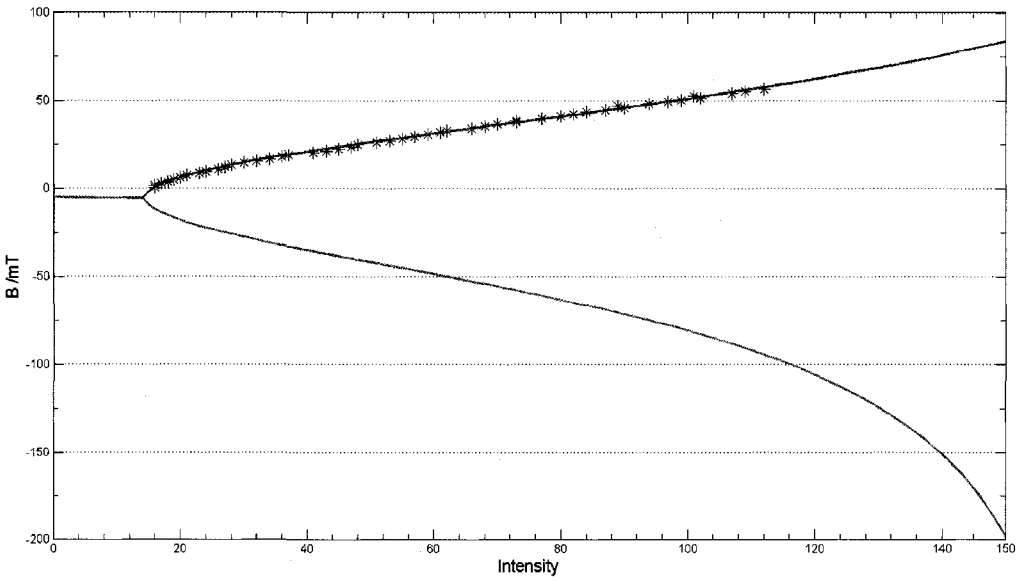

Figure 3.11: A complete calibration curve. Black markers are measured calibration points, upper blue curve plots function 3.12, and lower green curve plots function 3.13 in an intensity range from 0 to 150.

Inserting the experimental data into each of the following four magnetic field expressions, Eq. 3.12 gives the right fit and it is also the original calibration fitting function. Equation 3.13 smoothly connects with Eq. 3.12 but gives the region of *negative* magnetic field, i.e., the expression we are looking for. Equation 3.14 and Eq. 3.15 bare unphysical results are not considered.

We conclude that combining Eqs. 3.12 and 3.13 is the complete calibration curve. Figure 3.11 displays a plot of the two curves in the intensity range from 0 to 150. The lower curve goes to saturation around the intensity of 165 quickly. When intensity is below I_0, the calculated magnetic field values are complex numbers, and only the real part is plotted. It is impossible to measure any intensity $I_{x,y}$ smaller than I_0, so we do not consider the region where $I_{x,y} \leq I_0$.

The application of the new extended calibration curve varies for individual TRMOI measurements and is discussed in later chapters. Note that any curve we obtain from calculation or fitting other than the real calibration measurement will have uncertainties that may result in very noticeable errors if the majority of the data are

from the extended calibration curve.

Chapter 4

YBCO thin films

4.1 Introduction

In this Chapter, we show measurements and important results of the magnetic flux behavior of the high-temperature superconductor YBCO thin film using TRMOI technique. The measurements were done in the presence of both an external magnetic field and a transport current. By solving numerically the inversion of the Biot-Sawart Law one obtains the current density distribution in the thin film. The ac current enables the vortex matter to self-organize into two coexisting steady states of driven vortex motion with different characteristics. By comparing the magnetic field and current density distribution profiles to the FEM simulations, we find that they agree fairly well in the quasi-static state but the simulations predict a larger hysteretic behavior in the dynamic state.

We further study the current density evolution in the films as a function of the phase of the applied ac current in a perpendicular external magnetic field. We present a new empirical method to separate the total current distribution into a circulating current shielding the external magnetic field and the transport current. We discuss the effects of the ac current and the applied dc field separately in comparison with

the modified critical sate model. No existing theory explains the transport current and shielding current for the case, and our work could be an indispensable approach to such theory.

4.2 Experimental

In our experiment, the YBCO thin film samples have typical dimensions of 10×5 mm with the $250 - 300$ nm thick superconducting layer. The films are normally grown by pulsed laser deposition (PLD) on a bicrystalline $LaAlO_3$ or a $SrTiO_3$ substrate. Determined by ac susceptibility measurements, the YBCO thin films exhibit a critical transition temperature of $T_c = 91$ K, and show a sharp transition within two degrees (at 2.2 Oe loss data). To reduce the critical current, the samples are bridged by a photolithographic technique, whose length is $l = 6$ mm and the cross section width is $2w = 475\mu m$. At 77 K, the critical current density is $J_c = 3.42 \times 10^6 A/cm^2$ corresponding to a critical current $I_c = 4$ A. Figure 4.1 is a picture of a typical YBCO single-bridged thin film sample taken with our optical microscope using a mercury lamp (see section 3.1.2).

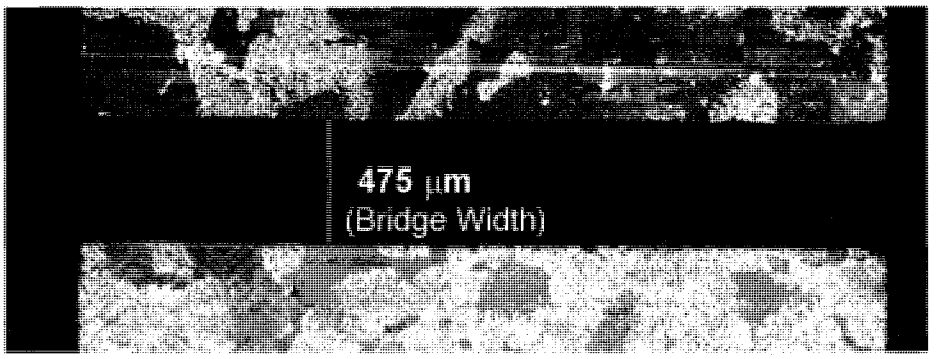

Figure 4.1: The picture of a YBCO thin film. The bridge width $= 475\mu m$.

In our time-resolved magneto-optical imaging experiment, the measurements are often taken at frequency $f = 1000$ Hz. The experimental set-up and basic procedures

are explained in detail in chapter 3. For a whole view of the YBCO thin film bridge, we select a 4× objective to obtain an observing area of $3.4 \times 2.6\ mm^2$, which restricts the spatial resolution to a few microns.

The sample is zero field cooled down to $T = 20 - 40$ K. Then a magnetic field dependence measurement is done with a ramping-up field from 0 mT to 60 mT at a step size of $1 - 2$ mT. The step size is easily adjustable using our custom-developed LabView GUI.

Figure 4.2 is a MO image of the sample with an external field $B_a = 10$ mT and no transport current. There are normally some defects at the edges of the sample bridge which cause inhomogeneous light distribution. We choose a relatively uniform area (between the two blue lines confine), in which the 2D light intensity profiles are averaged.

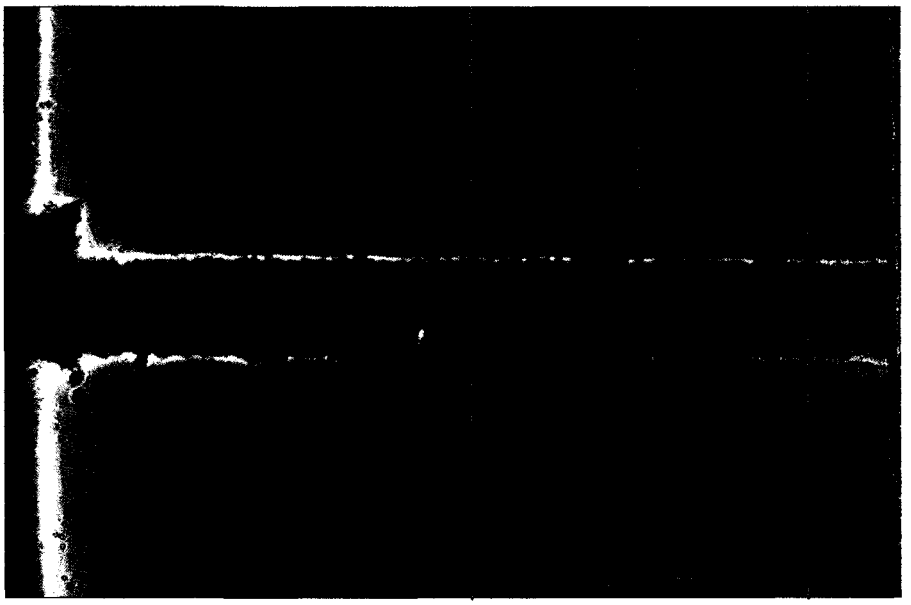

Figure 4.2: A MO image of YBCO thin film with only a perpendicular field applied. The blue lines confine a relatively homogeneous area for taking the 2D profiles.

The 2D magnetic field distribution profiles across the sample width $2w$ (indicated by the arrow) as a function of the external magnetic field are shown in Fig. 4.3. The

profiles are calculated from the calibration of light intensity profiles (see section 3.3). As predicted by the critical state model, the flux penetrates the sample from both edges where the magnitude of the field is maximal, which peaks at almost 100 mT while the external field is at 65 mT. Outside the bridge, the magnetic field equals the value of applied field, and in the sample center, there is no flux thus the field is zero. As the field increases from 0 to 65 mT, the profiles are shaded in blue-black-red.

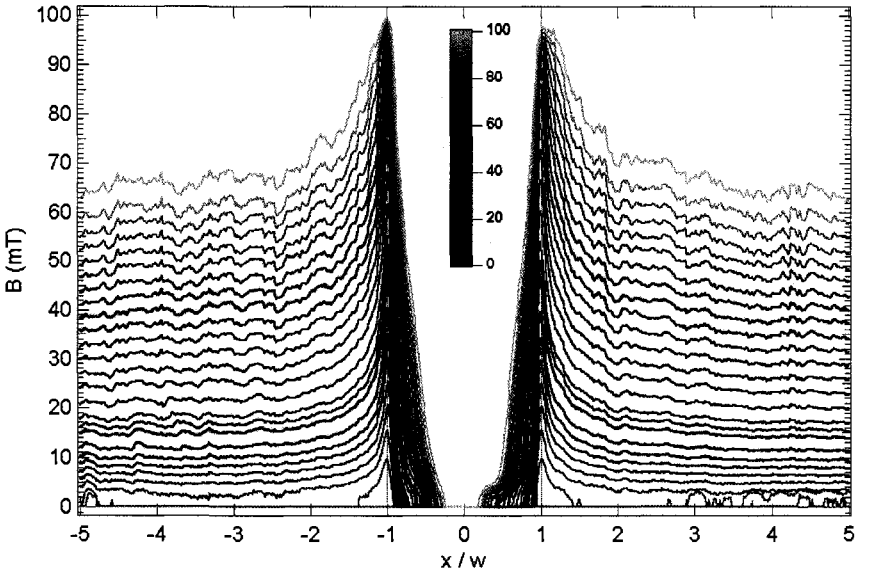

Figure 4.3: The field distribution profiles across the sample width for the field-dependent measurements (calibration). The vertical black dotted lines at $x/w = [-1, 1]$ indicate where the edges are located.

4.3 Results and discussions

4.3.1 Phase-dependence measurements

After the field-dependence measurements for calibration, the film is reset by raising up the sample temperature over its critical temperature. Then the sample is zero-field cooled down again to about 24 K. A perpendicular magnetic field $B_a = 10$ mT is applied and an ac current $I(t) = I_0 \sin(2\pi ft)$ with $I_0 = 8.5$ A and $f = 1000$ Hz is sent

through the sample. The applied current approximately equals to 30% of the critical current $I_c = 30$A. As shown in Fig. 4.4, the MO images are taken at 25 (starting at 0) equidistant phase angles over one current period $\phi = 0° - 360°$ at 1000 Hz, thus the time resolution is $40\mu s$.

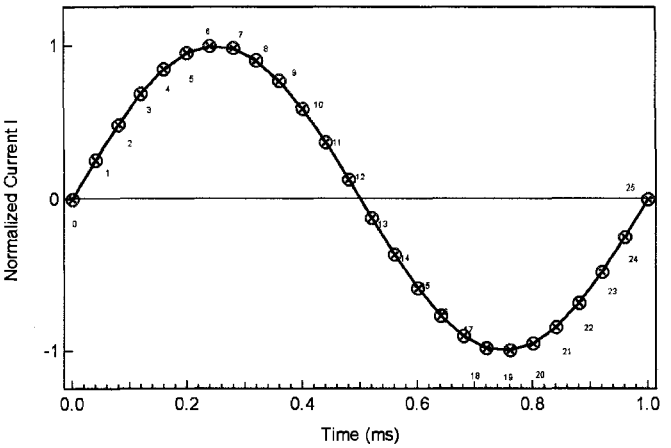

Figure 4.4: The 26 (from 0 to 25) phase points arrangement over a full cycle of an applied ac current.

Figure 4.5 is a series of 6 TRMO images of the YBCO thin film. The images are enhanced at the center bridged area with sharp edges with about 10% of the whole bridge length. The 6 images are taken at different phase points as indicated in the figure. The white arrows in the center of the images indicate the current direction. Bright areas in the images correspond to regions of high magnetic field near the edges of the sample. The dark area in the center of the images are the flux-free region. The uniformly green region represents the intermediate magnetic field outside the sample. At the zero current phases ($\phi = 0°$ and $\phi = 180°$), the perpendicular external magnetic field results in positive and symmetric flux penetration, while inhomogeneities in the flux distribution happen near the sample edges. The finger-like patterns formed by the vortices are visible in the images.

For the other 4 phase points with simultaneously applied magnetic field and ac current, different amount of flux penetrates at the two edges of the sample depending

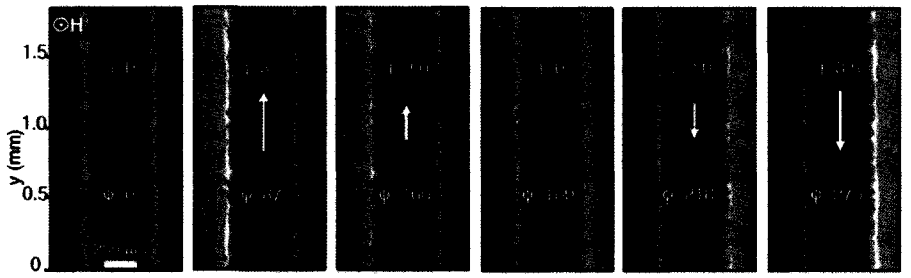

Figure 4.5: TRMO images for 6 different values of phase ϕ of the applied ac current with the applied field normal to the surface. To display more clear detail features, each images are enhanced in contrast and its color channels.

on the direction and intensity of the ac current. A higher flux penetration occurs on the left side of the sample when the transport current flows in the positive $y-$direction at phase points $\phi = 87°$ and $\phi = 160°$. Additional flux penetration occurs on the right side when the current flows in the negative $y-$direction at phase points $\phi = 218°$ and $\phi = 275°$.

Magnetic flux distribution

The time dependent magnetic flux distribution profiles of YBCO thin film are shown in Fig. 4.6 of the first (a) and the second half (b) wave of the applied current. At regions far outside of the sample bridge, the magnetic field approaches the applied field value of $B_a = 10$ mT, which reflects a quantitatively correct calibration. The non-smooth profiles outside the sample are mainly caused by the Bloch walls in the MO indicator. One can see the differences of the current direction in the two half-period profiles. In Fig. 4.6(a) the first half of the cycle the self-field due to the applied current adds positive flux on the left edge of the sample and negative flux on the right. The intensity on the left of the field profile is increased and a steep ridge and a trough are formed on the right. In the second half of the cycle shown in Fig. 4.6(b), the applied current flows in the negative direction and increases the flux profiles on the right edge while it forms a sharp minimum close to the left edge,

creating symmetrically opposite flux profiles with respect to the first half of the cycle

.

Comparing the two half-cycle field distributions, one finds the profiles corresponding to the same transport current in the decreasing and increasing current half wave are similar, which implies the remanence effects in the transport measurements are negligible and the transport currents do not create any flux in the sample. The field peaks at the sample edges change about 19 mT as the current alters from the maximum to the minimum. The magnetic field reaches zero at the flux penetration front $a \approx 0.73w$.

In the flux-free region $|x| < a$, the magnetic field is set to zero manually due to the noises from the nonlinear calibration. The calibration function (3.7) is strongly amplifies noise in the intensity at low intensity levels when I is very close to I_0 due to the vertical gradient $\partial B/\partial I$ of the calibration curve. A small amount of noise of the images can cause a few mT of fluctuations in the sample center where $B = 0$ mT. The magnetic field profiles are smoothed at the edges after the center regions being set to zero.

The current density distribution

The current density distribution are calculated from the numerical inversion of the Biot-Savart law. All the current density profiles we inverted from our calibrated magnetic field data are using this inverted matrix method of (2.39). The current density in the thin film integrated over the film thickness d is given in units Am^{-1}. The distance between the sample and the MO indicator $h = 0.01w = 2.35\mu m$ is assumed in the inversion.

Figure 4.7 are the phase dependent current density profiles. Only the central part of the profiles $\left|\frac{x}{w}\right| \leq 2$ are shown in this figure to give larger view of the central part.

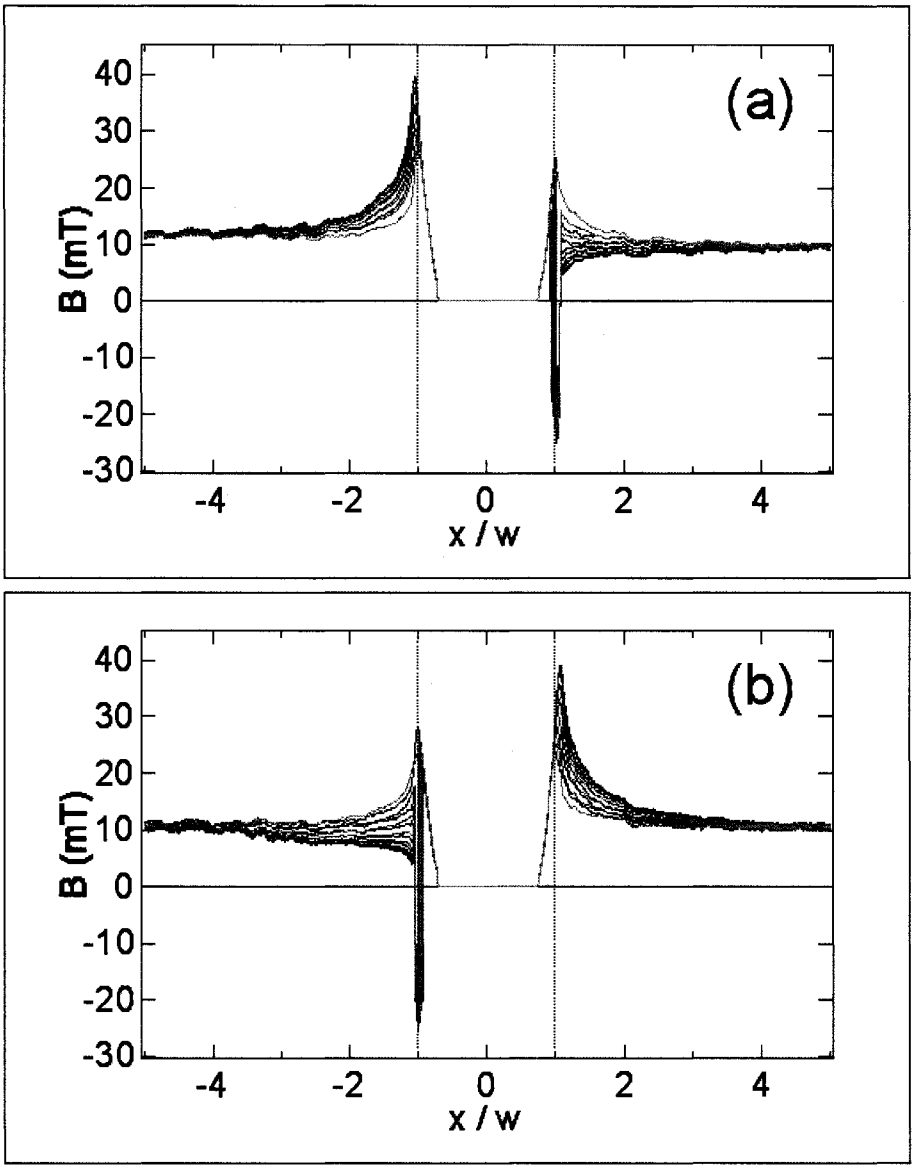

Figure 4.6: The magnetic field profiles for different values of the phases of the applied ac current with a peak value of $I_{peak} = 8A$. The top, from red to green curves are profiles taken for the first half of the period $\phi = 0°$ to 180°, and the bottom is the second half period.

The measured profiles are same as in the field distributions profiles that are extended more than $\left|\frac{x}{w}\right| = 5$ outside the sample.

When there is no transport current flowing in the sample (at phases $\phi = 0°$ and $\phi = 180°$), the current distributions are symmetric, which is different from the other phase points. The current line profiles change shape and magnitude mainly at the sample edges. Their peak positions indicate the region where the magnetic field changes its sign. Outside of the sample bridge ($\left|\frac{x}{w}\right| > 1$), there is no current flowing thus the current density goes to zero.

4.3.2 The ac current driven dynamic vortex state

We already described the critical state model in section 2.4, and discussed that this model would not be enough to well predict our TRMOI data measured with both field and ac current applied. In the thin film measurement, we directly compare the data to the model and the comparison explains the limitation of the model.

Figure 4.8 shows the magnetic field profiles at different transport current phases. At phases $\phi = 0°$ and 360°, the profiles overlap almost completely. At $\phi = 90°$ and $\phi = 270°$ phase points, the two profiles are very asymmetric but mirrors each other. The dotted curves are the prediction of the critical state model. We fit the theoretical magnetic flux distribution to the measured data at $\phi = 90°$ and zero phase point. The parameters we use in the critical state model are the transport current I_T, the critical current density J_c in the form of the characteristic field for the thin film geometry $B_f = \frac{\mu_0 d}{\pi} J_c$, the applied field B_a and the observation distance h. In general the model explains the data well: outside of the sample ($\left|\frac{x}{w}\right| \leq 1.4$) the measured magnetic field profiles agree with the model; the flux penetration front at $x \approx 0.73w$ is reproduced well; when there is no transport current, the model fits the data in shape with a little higher peaks; at $\phi = 90°$ the lower side of the field peak is reproduced well. However,

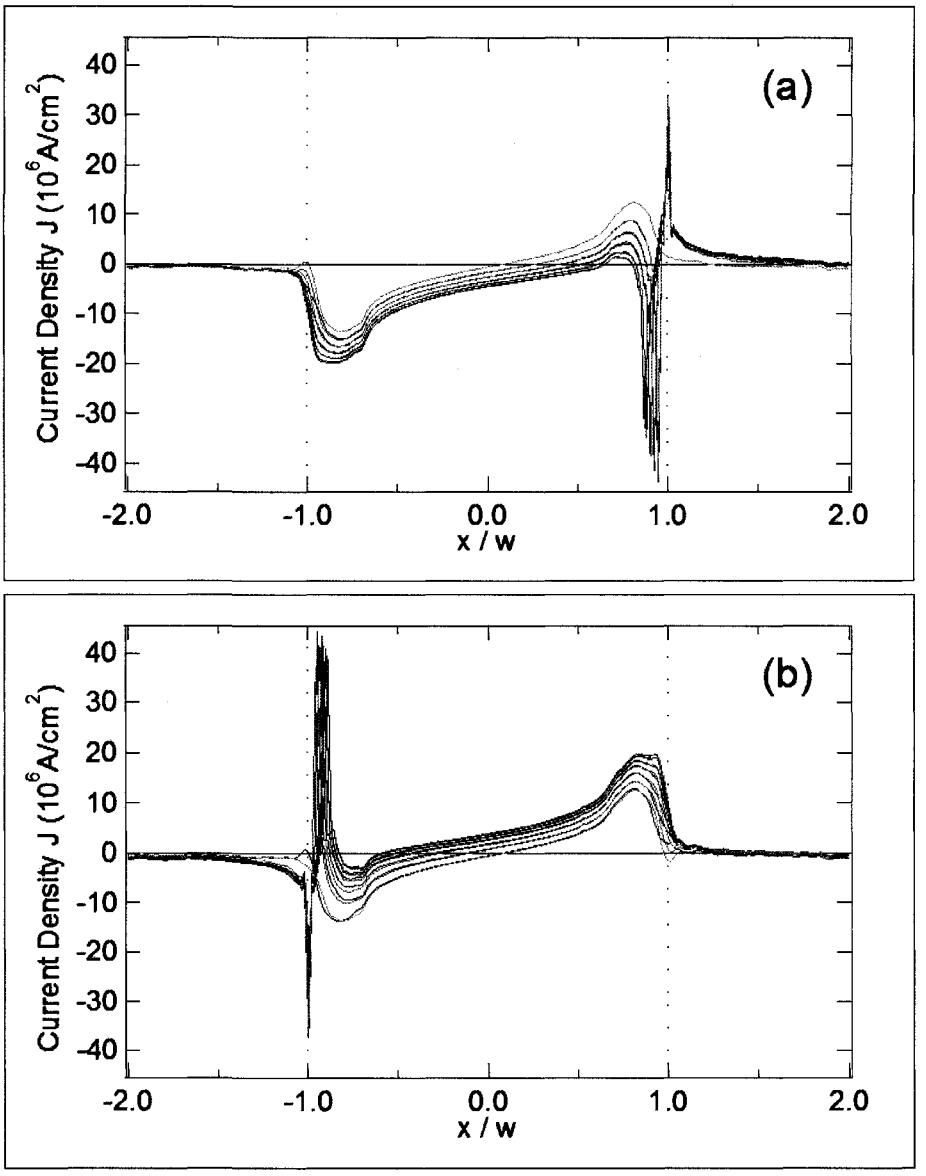

Figure 4.7: The current density profiles for different values of the phase ϕ for the total current showing in (a) the first half period and (b) the second half period of the applied ac current.

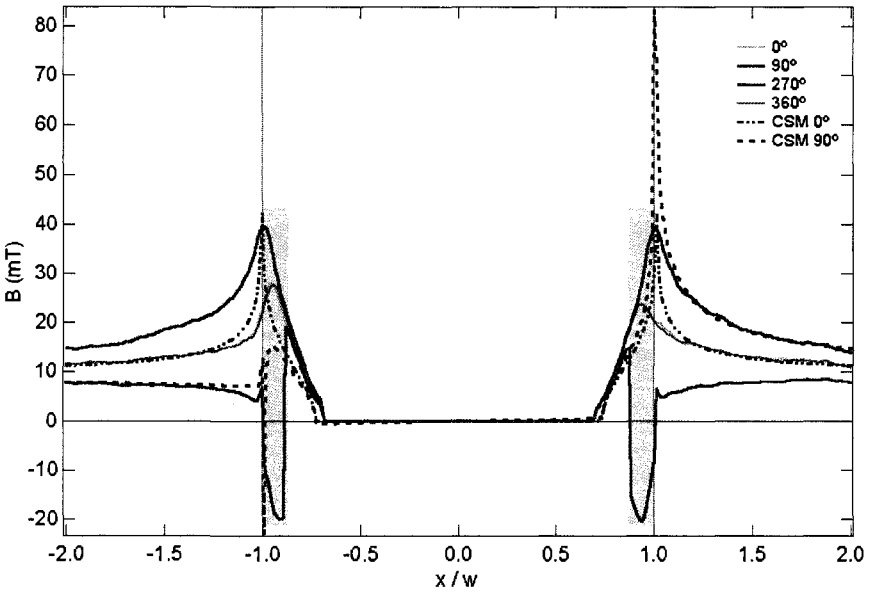

Figure 4.8: The magnetic field profiles at selected phase points 0° and 90° plotted with the modified critical state model.

the higher peak on the right hand side is overestimated by the critical state model. More misfitting details can be easily observed in blue high-lighted area in the figure. The lower peak is shifted more to the edges in the critical state model, and the flux front moves in to the sample center in a uniform shape but in our data, the transition is definitely divided into two phases.

The corresponding current density profiles are plotted in Fig. 4.9. In the center of the sample without flux penetrated, the model and the experimental curves have a good overall agreement as well as at the zero phase points where no transport current is flowing, the critical state model can predict the shielding current distribution fairly well. At the phase point $\phi = 90°$, at the right hand side, the model shows a higher peak than the data yet fits well outside the blue high-lighted region; and on the left hand side, the experimental curve shifts the current further inside the sample with higher values and different shape. The main differences again happen in the blue high-lighted regions that we intend to give more discussion and explanations.

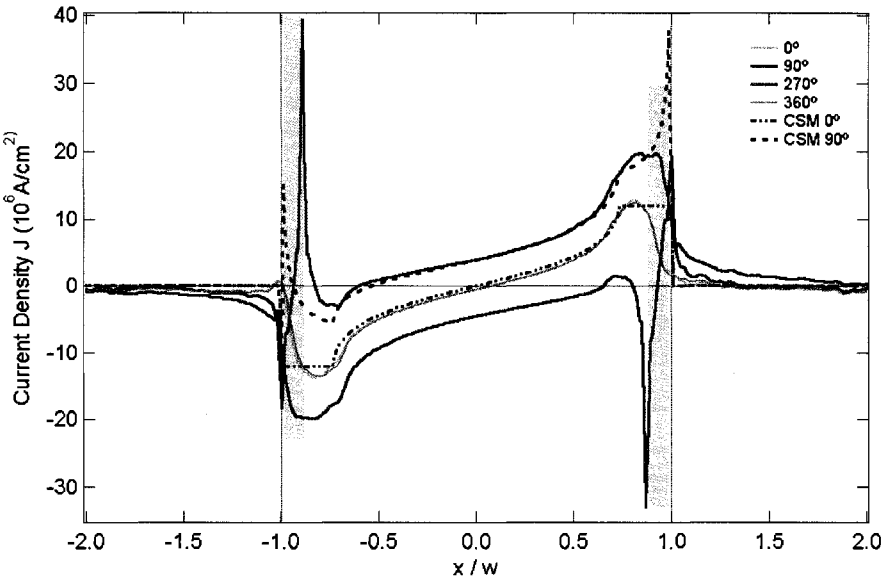

Figure 4.9: The current density profiles at selected phase points plotted with the critical state model at 0° and 90°.

The interesting features of the magnetic vortex penetration in HTSC thin films revealed in our TRMOI experiments are induced by the applied field and/or the transport current. The critical state theory describes the behavior of the magnetic vortices in quasi-static changes of an applied field or a transport current[45,47]. Recent experiments show that the vortex mobility can be strongly affected by a dynamic magnetic field or ac current. Some of the vortex dynamics are ascribed to dynamic instabilities[20,57] and transient[58] or steady states of driven vortex motion created during the reordering induced by the applied current[59]. Many HTSC applications[60] are related to the dynamic interaction of the vortex matter with both a magnetic field and a current applied.

To study the dynamical vortex states, we now compare the cross-sectional field and current profiles from the measurements with simulations using a recently developed method based on FEM calculations (see section 2.4.3) that accounts for thermally activated flux creep. In our simulation, we fix the magnetic field $B_a = 10$ mT and the transport current $I_t = 8.54$ A at 1000 Hz which are the values we used in our

experiments. In order to avoid transient effects, the tenth cycle of simulation is considered for analysis.

The magnetic field distribution and the current density profiles at selected phase points are displayed in Fig. 4.10[51] with the calculated FEM profiles for the two extreme phase points $\phi = 90°$ and $\phi = 270°$. The simulations reproduce well the flux penetration front and the shifting of the maxima with the phase and the asymptotic behavior outside the sample. Near sample edges the simulations give higher peaks than the measured curves which also move further inside the sample center.

Figure 4.11[51] shows in details of the shielding currents induced by the field without any net transport current flowing in the film. For a complete comparison, we include different shielding current profiles in this figure. The black line represents the shielding current from static field-only measurement ($B_a = 10$ mT). The curves indicated by blue squares and red triangles are the profiles measured at $\phi = 0°$ and $\phi = 180°$ in transport measurements with the same applied field. These two profiles overlap fairly well over the whole sample width, with the exception of a small deviation in a region close to the edges. The smooth blue and red solid lines are the FEM simulations at the same phases. Near the sample edges, the simulations show a stronger hysteretic behavior than the measured profiles. Comparing the three different shielding currents, the transport current reduces the peak shielding current and moves the shielding current further inside the sample. From the current density profiles in (**b**), the current density is reduced and a gap appears near the edges. No hysteretic effects are observed.

In the mixed state regions near the HTSC sample edges, the vortex motion are divided into two coexisting steady states. Near the sample edges exists a dynamic state of plastic motion. The Lorenz force associated with the transport current is larger than the critical depinning force and causes the vortex to move inside. The ac

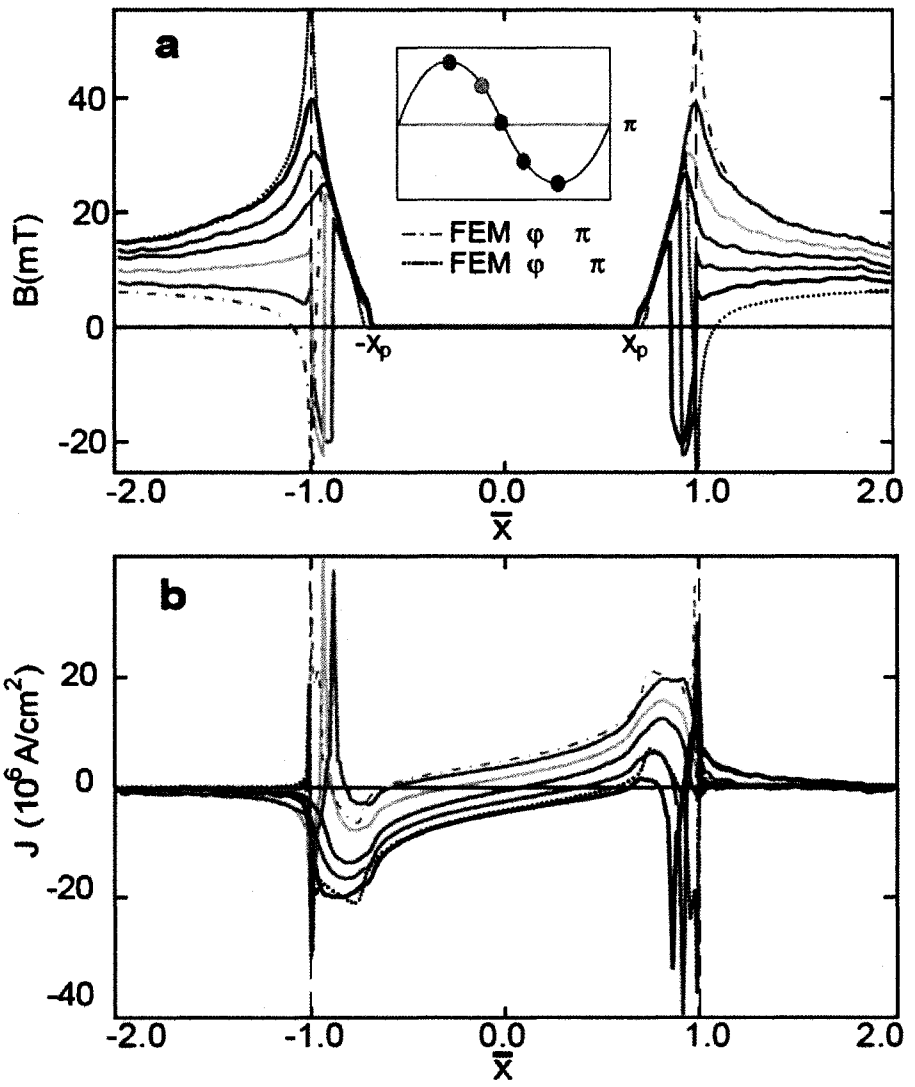

Figure 4.10: The magnetic field distribution (**a**) and the total current density profiles (**b**) for selected phase points measured in TRMOI experiments, compared to the FEM simulations (dotted line) at 90° and 270°.

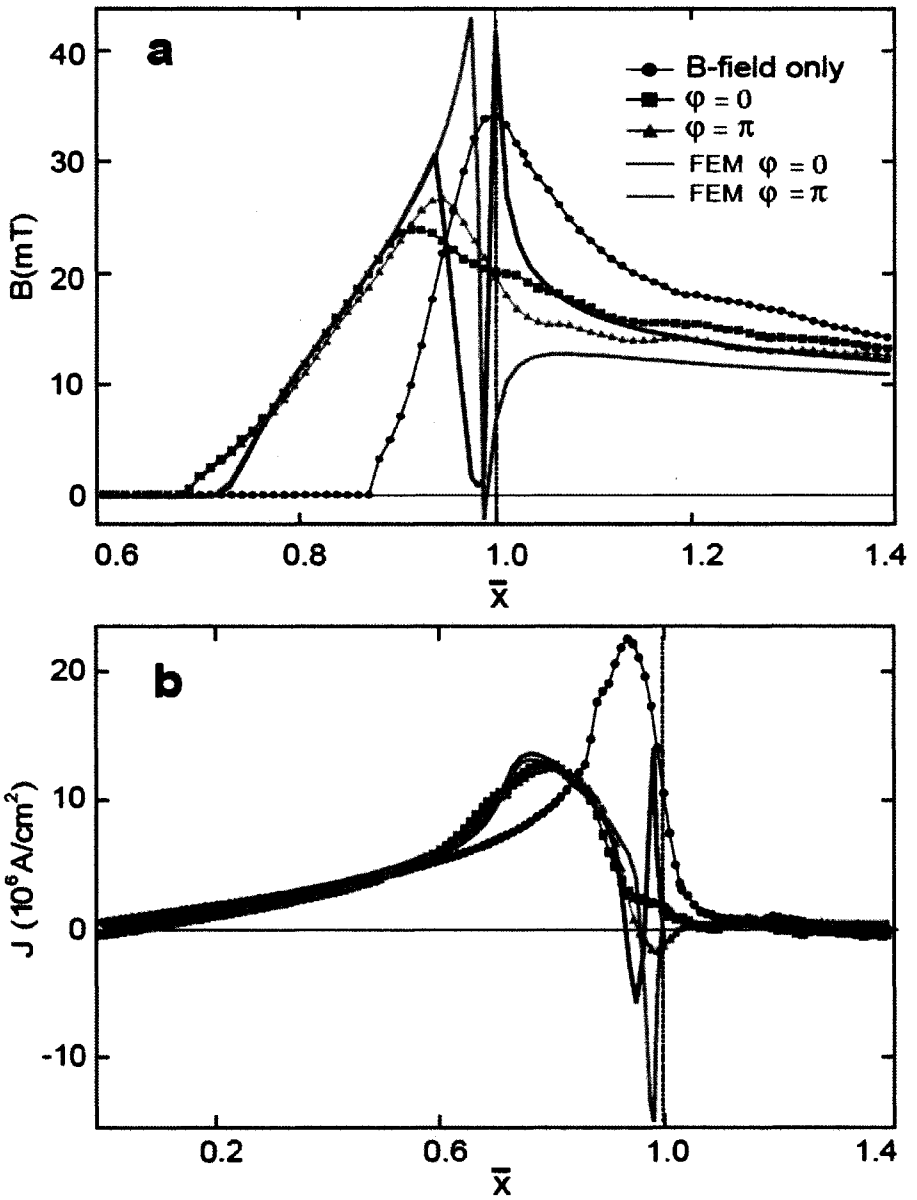

Figure 4.11: The magnetic field (**a**) and the current density distribution (**b**) corresponding to the shielding current at $\phi = 0°$ and $\phi = 180°$, compared to the shielding current density induced by an applied field only $B_a = 10$ mT and the corresponding FEM simulations at the same phase points.

current at the edges injects flux creating a transient disordered state. The vortices stay in a steady state of driven vortex motion. The motion occurs in the presence of strong pinning centers that hinder a smooth entrance of the injected fluxions.

4.3.3 The transport current dynamics

The previous Figures of 4.8, 4.9 and 4.11 show no significant remanence or hysteretic effect at the zero phase points with no transport current flowing, instead the flux lines rather distribute in a more equilibrium way to reduce the screening currents and the hysteresis effect. This phenomenon is in contrast to what the critical state model or the FEM simulation results predict. In the total current density distribution (Fig. 4.7), at zero phase points of $\phi = 0°, 180°$ and $360°$, there is no transport current flowing and thus the current density at these phases represent the circulating shielding current $J_{circ} = J_{total}$, which shields the external magnetic field. This allows us to obtain the transport current distribution at each phase point simply by subtracting the circulating current from the total current. Therefore the time dependent transport current distribution is

$$J_{tr} = J_{total}(\phi) - J_{circ}. \tag{4.1}$$

Figure 4.12 shows the transport current distribution calculated from equation (4.1) for a complete ac cycle. The two half cycles are colored in blue and red shades. At the three zero phases $\phi = 0°, 180°$ and $360°$, the transport currents are zero after the separation, so the total currents which are also the shielding currents are plotted in the same figure for comparison.

This empirical approach is valid because the flux induced by the magnetic field remains pinned during the cycle of the transport ac current thus the shielding current density is stationary. The shielding current only flows in the region near the sample edges where the Lorentz force is not sufficient to change the flux distribution and it is

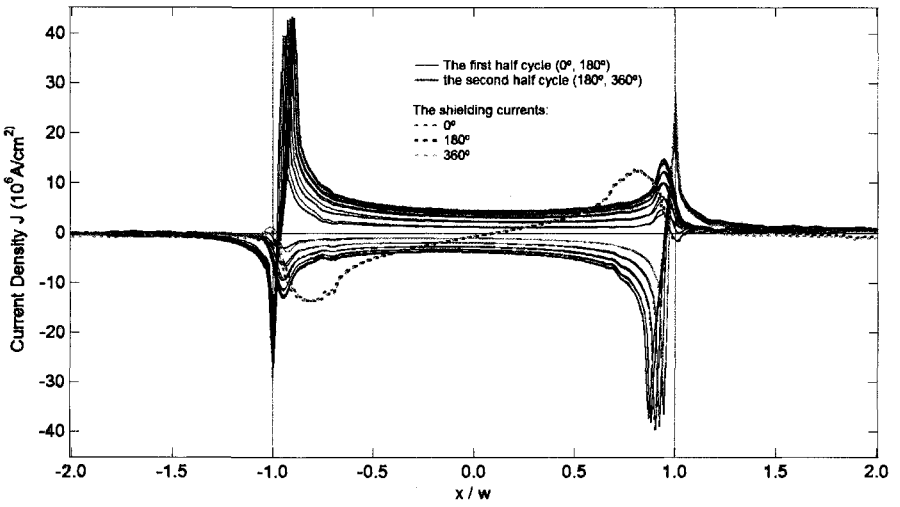

Figure 4.12: The time dependent transport current distributions plotted with the shielding currents (the dashed lines) at zero phase points $\phi = 0°, 180°$ and $360°$.

independent of the transport current which does not induce any flux in the flux-free region. Furthermore, we integrate the calculated transport current density (Fig. 4.12) in the range of the sample bridge width. The applied ac transport current $I(t) = I_0 \sin(2\pi ft)$ with an amplitude $I_{peak} = 8.54$ A in the experiment. The integration yields a sine wave shape with the two peak values $I_{peak+} = 8.10$ A and $I_{peak-} = 7.00$ A, respectively. Figure 4.13 compares the transport current sending from the ac power source and the integrated transport density profiles experimentally obtained from the TRMO images. Our data reproduces correctly the sine wave of the applied current and yields the correct magnitude of the applied ac current with overall error less than 10% which proves that this separation of the transport current distribution is quantitatively correct. The orgins of the ac current reduction in the data may due to the transport current bypassing the sample over a shortcut through the cryostat. However, before the experiment all part of the cirulating wires and units are well isolated and the sample itself is superconducting so that a normal conducting shortcut parallel to the sample would not divert much current from it. The distance between the sample and the indicator is underestimated since higher distance would lead to

higher current density, but the increase in current density with this distance is small.

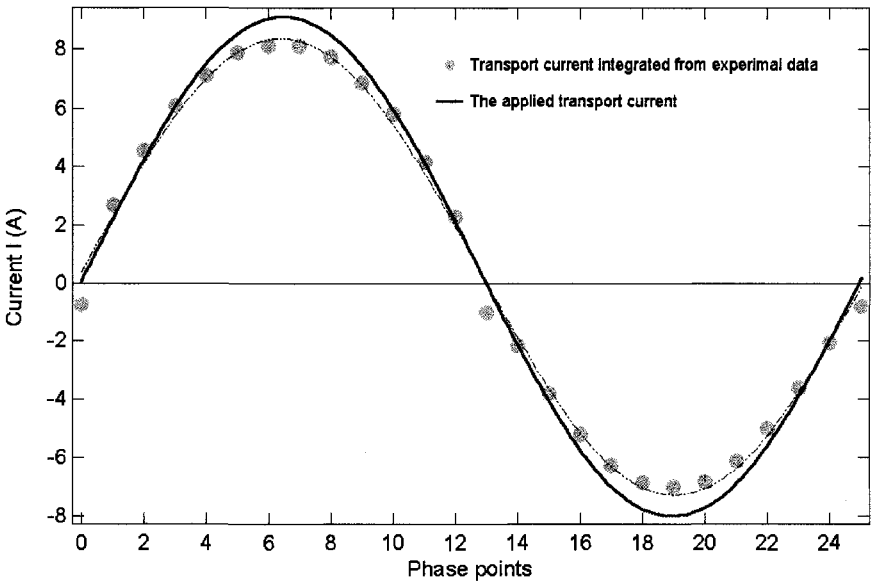

Figure 4.13: The integrated transport current value for the 25 measured phase points (olive green dots), which reproduce well the applied ac current (dark green solid line).

The total current distribution of a dc magnetic field applied simultaneously with an ac current cannot be predicited well by the critical state model, which only gives analytical solutions for the cases when there is either a magnetic field or a current applied to the thin film but not the superposition of both. Next, we can compare the transport current density profiles to the theoretical results. In thin film geometry, the current density expression for only a perpendicular magnetic field applied is given in Eq. (2.20) and the current density expression for only a transport current applied along the $y-$direction is given by Eq. (2.25) (see section 2.4.2).

Figure 4.14 shows the transport current at elected phase points compared with the best fits (the dotted lines) from Eq. (2.20). The theoretical curves reproduce the experimental data well in the sample center. The fits give $\frac{I_0}{Ic} = 0.35$ and $J_c = 1.7 \times 10^7 Acm^{-2}$ that are in good agreement with our data. The major difference is the asymmetry in the measured profiles with most current flowing at the edges. The transport current likes to distribute in such a way that there is no induced flux in the

flux-free region and yields the relation[47] of

$$|J_{total}| = |J_{tr} + J_{shielding}| < J_c. \tag{4.2}$$

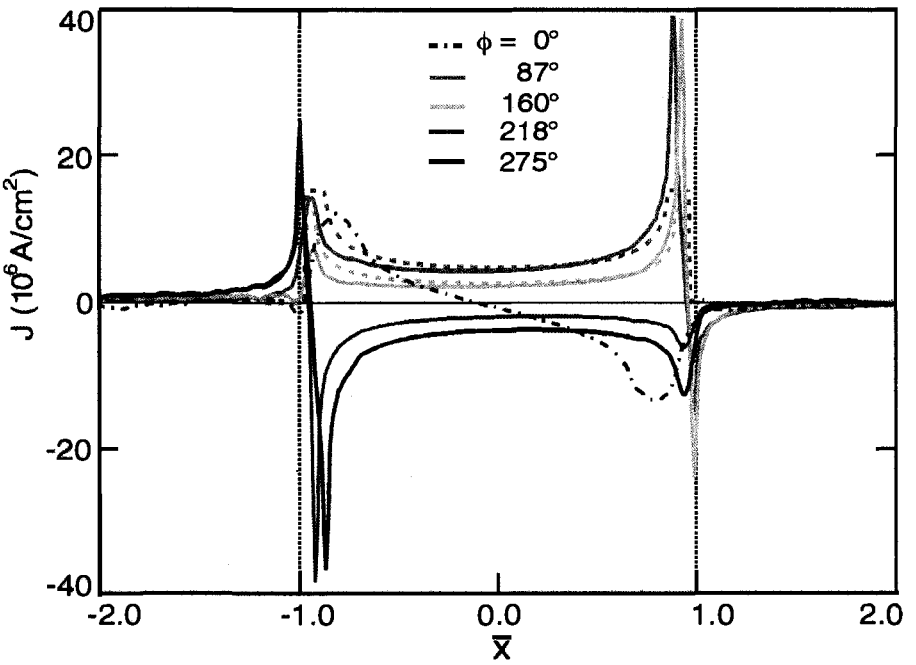

Figure 4.14: The current density profiles for different values of phase for transport current (solid lines), the corresponding best fits (the dashed lines) based on the CSM and the shielding current at zero phase (the black dotted line).

At the sample edges, the very high local densities in the transport current results from the abrupt variation in the flux distribution in that region. The ac current causes the nucleation of vortices and anti-vortices at the sample edges. The positive and negative fluxions annihilate in these narrow regions resulting in zero-flux lines which cause spikes in the ac current density. The peaks are a direct consequence of the applied ac current. Peaks in the current distribution have been previously observed in pulsed current MO measurements[61]. The stacking faults of the YBCO thin film during PLD deposition causes threading dislocations, which give the vortices strong pinning sites even in very high current densities. The thin films grown by

PLD have a large amount of columnar boundaries providing the necessary pinning strength required for the high local values of the transport current observed in our measurements.

One can find the phase dependent self-field distribution from the transport current distribution by using the Biot-Savart law in one dimension Eq. (2.32) as shown in Fig. 4.15. The peaks of the self-field are close to at the sample edges. The self-field profiles are zero in a wider region than the field free region (indicated by the magnetic profile at zero phase) of the sample center. The self-field is responsible for the strong phase variation of the magnetic flux profiles at the sample edges.

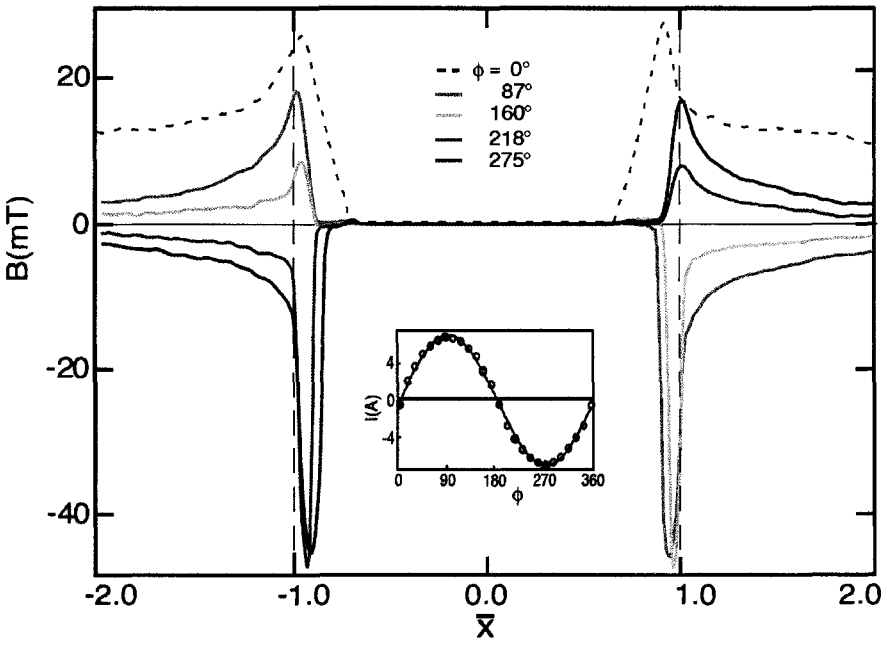

Figure 4.15: The self-field profiles (solid lines) from the transport current plotted with the magnetic profile at zero phase $\phi = 0°$ (the dashed line).

In the dynamic transport current study, we find that the transport current distribution flows predominantly at the sample edges where it cancels out the shielding current. The overall distribution of the current density is governed by the minimization of the total loss caused by the reduced Lorentz force on the vortices. When the transport current flows predominantly in the opposite direction of the shielding

current, the two opposing Lorentz forces cancel each other, thus the vortices dissipate less energy.

4.3.4 Frequency-dependence measurements

The magnetic field distribution in YBCO thin films with an applied ac current are measured at different frequencies to determine whether the time dependent magnetic effect lead to a frequency dependence effect.

In the experiments, we zero-field cool the film down to $T = 20$ K. When the sample reaches the temperature, a 10 mT perpendicular external field is applied to the sample with an ac transport current of amplitude $I_{max} = 8.54$ A. The frequency is varied in the range of $f = 100$ Hz to 1000 Hz with a step size of 100 Hz. We collect TRMO images at each frequency for phase points $\phi = 90°$, 270° and the three zero phase points of the ac current, and one between the extremes and the zeros.

The difference from previous TRMOI measurements are the camera's exposure time adjustment, since at lower frequency, less pulses are captured in the same time thus leading to darker intensity profiles, which will of course effect the calibration to obtain the correct magnetic field profiles. An adjustment can be done either by carefully comparing the intensity profiles while taking the measurements or normalizing all the intensity profiles later on before the calibration (See section 3.3). In this measurement, we can convert the intensity profiles recorded at different frequencies to the highest frequency 1000 Hz with an exposure time $\tau = 20$ ms.

This method is based on a linear approximation of the curve shown in Fig. 3.10. The points may not arrange so nicely and the fit linear curve could have a large error thus giving normalization uncertainties. To minimize such errors, we may normalize the light intensity while we take the data by adjusting the laser output power. A. Frey[62] reported in detail frequency dependence measurements using this normaliza-

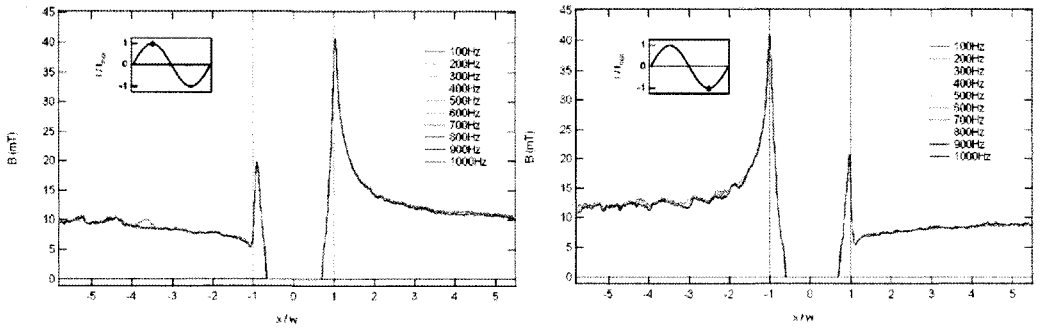

Figure 4.16: The magnetic field distribution across the YBCO thin film bridge of 10 different frequencies at $\phi = 90°$ and $270°$ phases of ac transport current.

tion, and concluded there is no visible frequency dependent effects. Small variations are just artifacts due to this imperfect exposure time correction, with an error in the parameter $\xi \approx 10\%$. Figure 4.16 shows frequency dependent magnetic field profiles at the maximum (left) and minimum (right) phases of the ac transport current.

4.4 Conclusion

In conclusion, we use the TRMOI technique to study the spatial magnetic field distribution of a YBCO thin film in high frequency $f = 1000$ Hz region at low temperatures $T \approx 20 - 40$ K. We present a numerical solution to obtain the current density profiles from the inversion of the Biot-Savart law, and compare the resulting magnetic field and current density distribution with the critical state model and the FEM based simulations.

The TRMO images show the phase evolution of steady state vortex motion driven by an ac transport current, and the quantitative analysis of the experimental data and FEM simulations reveal the formation and coexistence of a quasi-static glassy state in the sample interior and a disordered dynamic state of plastic motion near the edges of the thin film.

In the transport current study, we separate the total current density into trans-

port current and shielding current. The transport current density profiles distribute differently from the prediction of the modified critical state model, are asymmetric and have pronounced peaks at the sample edges. They tend to arrange in such a way as to minimize the total energy losses.

At last, we presented briefly the frequency dependence measurements and concluded that in the range from 100 Hz to 1000 Hz, the magnetic field distribution is independent of frequency and shows no time dependent effects, such as thermally activated flux creep.

Chapter 5

YBCO Multifilamentary thin films

5.1 Introduction

As the most promising HTSC ceramic material, YBCO is used in both dc and ac applications. In recent years, the new YBCO coated conductors, also known as the second generation HTSC, are widely used in many ac electrical applications, such as generators, power transmission cables, transformers and motors (see section 6.1 for more discussions). In such ac power applications, the low ac loss is important. For high frequency applications like for the new airborne electrical devices[63], the ac loss reduction is crucial. There are several possible ac loss mechanisms: the hysteretic loss, ferromagnetic loss of the substrate, eddy current losses in the substrate and in the stabilizing layer, and transport current losses[64–66]. Hysteresis is the heat generated by the induced ac electric field when the material interacts with high density current. The hysteresis loss is proportional to the tape width[47] when the thin superconductor sample is exposed to an ac magnetic field and/or ac current[67–70]. The coated conductor tape has a relatively wide cross section that results in a very high aspect ratio inherent to the architecture. This makes the hysteresis loss a major problem in coated conductors[71].

The many methods that have been proposed to reduce the ac loss are all based on multifilamentary or striated structure of YBCO layer, because the amount of heat generated in such striated tape decreases proportionally to the ratio of the individual filament width to the sample width, and it reduces of the number of the filaments increases[72–74]. In a sinusoidal time dependent perpendicular field, the time average hysteresis loss for a superconducting filament is

$$\frac{< P >}{V} = \frac{4\mu_0}{\pi} f J_c w H_a, \tag{5.1}$$

where V is the volume of the superconductor, f is the frequency, J_c is the critical current density,w is the half width of a filament and H_a is the magnetic field amplitude. This concept was confirmed experimentally by Cobb *et al.*[75]. They measured the magnetization loops of small samples of YBCO thin film striated by laser ablation. The hysteretic loss obtained from the magnetization loops decreased in proportion to the filament width, as expected.

5.2 Experimental

So far, all the multifilamentary YBCO samples have been measured in an ac magnetic field with a static field, or in a flowing current induced by an ac field without static field[66], or in a frequency dependent experiment[76]. A transport current measurements on multifilamentary films offers an interesting change, and our TRMOI technique offers this possibility.

Numerous techniques can be used to striate the YBCO film, including wet chemical etching, ion beam etching, and laser ablation. Depending on different experimental purposes, the sample size, the number, the width of the filaments, and the width between each filaments varies widely. In our experiments, the sample size is normally

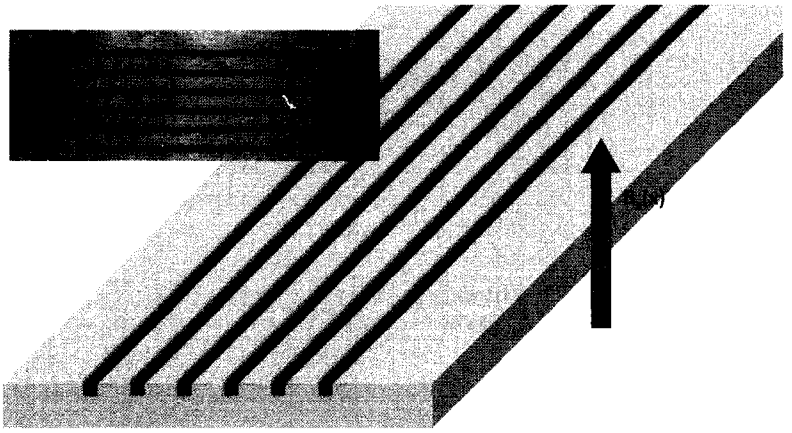

Figure 5.1: The YBCO multi-filamentary thin film sample with six etched filaments: a 3D drawing and a microscopic top view picture taken by our MOI optical setup.

0.5 × 12 mm with 6 filaments. The striation was made by photolithography and wet etching. The average superconducting filament width is 125 μm with an average separation of 500 μm. Figure 5.1 shows the sample we measured in the TRMOI experiment : The top view from a microscope, and the bottom view of a 3D drawing where the dark areas are the superconducting YBCO.

We examined the straited thin films carefully for defects. The defects between each superconducting filament may couple two neighboring filaments, and the defects on a superconducting filament may discontinue the superconductivity. The straight edges of each filament are necessary to obtain a uniform MO image. A good sample should have all 6 filaments conducting with sharp edges with no bridges between the filaments.

The multifilamentary sample is zero-field cooled down to 15 K, then we apply an increasing magnetic field from 0 mT to 60 mT for calibration. An MO image of the multifilamentary sample at $B_a = 40.21$ is shown in Fig. 3.9 of chapter 3. For ac transport current only measurements, there is no external magnetic field, we apply ac transport currents I_{tr} with peak values of $4 - 8$ A at fixed frequency $f = 1000$ Hz. Since there is no magnetic field, the signal is low and one may need to increase

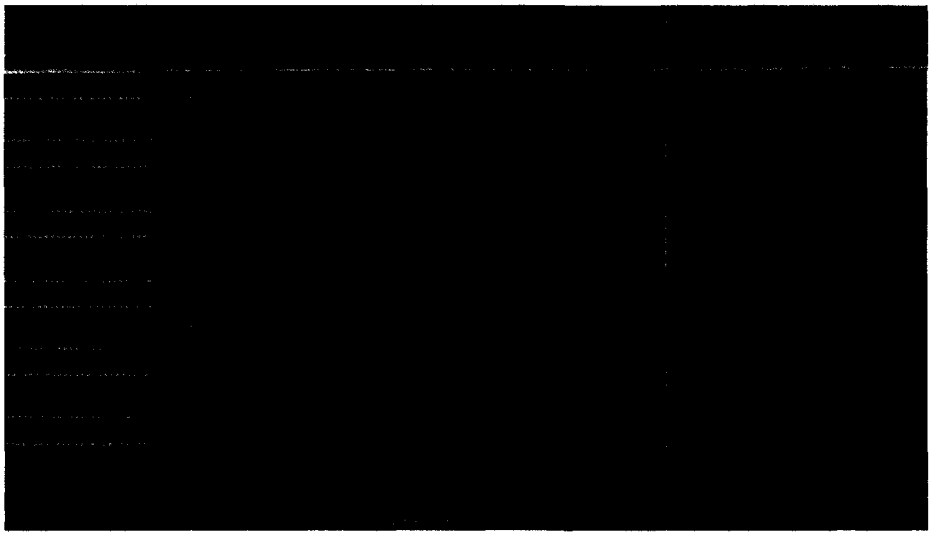

Figure 5.2: One TRMO image of six-multifilamentary film with $I_{tr} = 8A$ and no external field. The dotted lines indicate each filament's edge, and the dashed lines indicate the region of interest to take the profiles for further analysis. The dark circles and wavy lines are due to the MO indicator's imperfections. Using background correction, we can obtain more homogeneous light intensity.

the camera's exposure time to get better images. One sample image with enhanced contrast is shown in Fig. 5.2. For simultaneous ac transport and dc external magnetic field measurements, we fixed the field at $B_a = 5$ mT and applied an ac current with peak $I_{peak} = 5 - 8$ A in order to emphasize the current's effects on the sample. For a comparison, we also doubled the field to $B_a = 10$ mT and reduced the peak ac current to $I_{peak} = 4$ A. Figure 5.3 shows images taken while applying an ac current with peak $I_{peak} = 8$ A and applied field $B_a = 5$ mT at the maximum, zero and minimum phase points.

5.3 Results and discussions

5.3.1 Comparing different values of ac current and dc field

Among all the measurements mentioned above, we pick three sets of measurements on the six-multifilament YBCO thin film, and do the quantitative TRMO image analysis.

Initially, we choose the set of measurements with only an ac current applied in zero external field. The peak value of the applied transport current is 8A since the highest current gives the strongest signal and better results. For a convenient reference, we call this set of measurements *M80*. An image of *M80* is already shown in Fig. 5.2, in which $I_{tr} = 8$ A flows in one direction along the sample. The self-field induced by the current appears very bright on the top edges whereas dark lines (darker than the flux-free region) appear on the lower edges of each filament. This is because the two polarizers are just slightly off cross polarization, and the light intensity corresponding to the negative magnetic field can not be smaller than the lowest intensity the camera can sense. After light intensity calibration, the magnetic field distribution profiles are displayed in the top of Fig. 5.4.

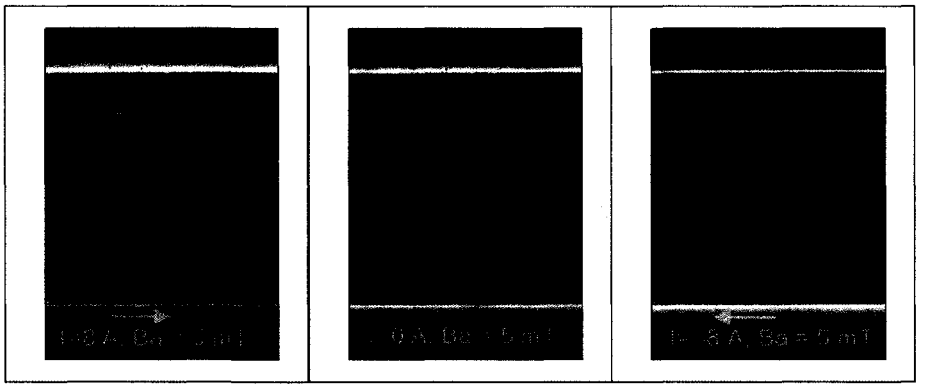

Figure 5.3: The enhanced color contrast TRMO images with applied ac current with peak $I_{peak} = 8$ A and applied field $B_a = 5$ mT at three phase points. The images show only the areas with relatively homogeneous light illumination and the least amount of defects.

In Fig. 5.4, there are 51 phase points over one complete period, $\phi = 0°$ to 360°, of the ac transport current at 1000 Hz, thus the time resolution is 20 μs. The positive and the negative half period are colored in cyan-magenta shades, respectively. The self-field distribution that is induced by the transport current is calculated from a careful calibration. Applying the numerically inverted Biot-Savart law, one obtains the total current density distribution as shown at the bottom of the figure.

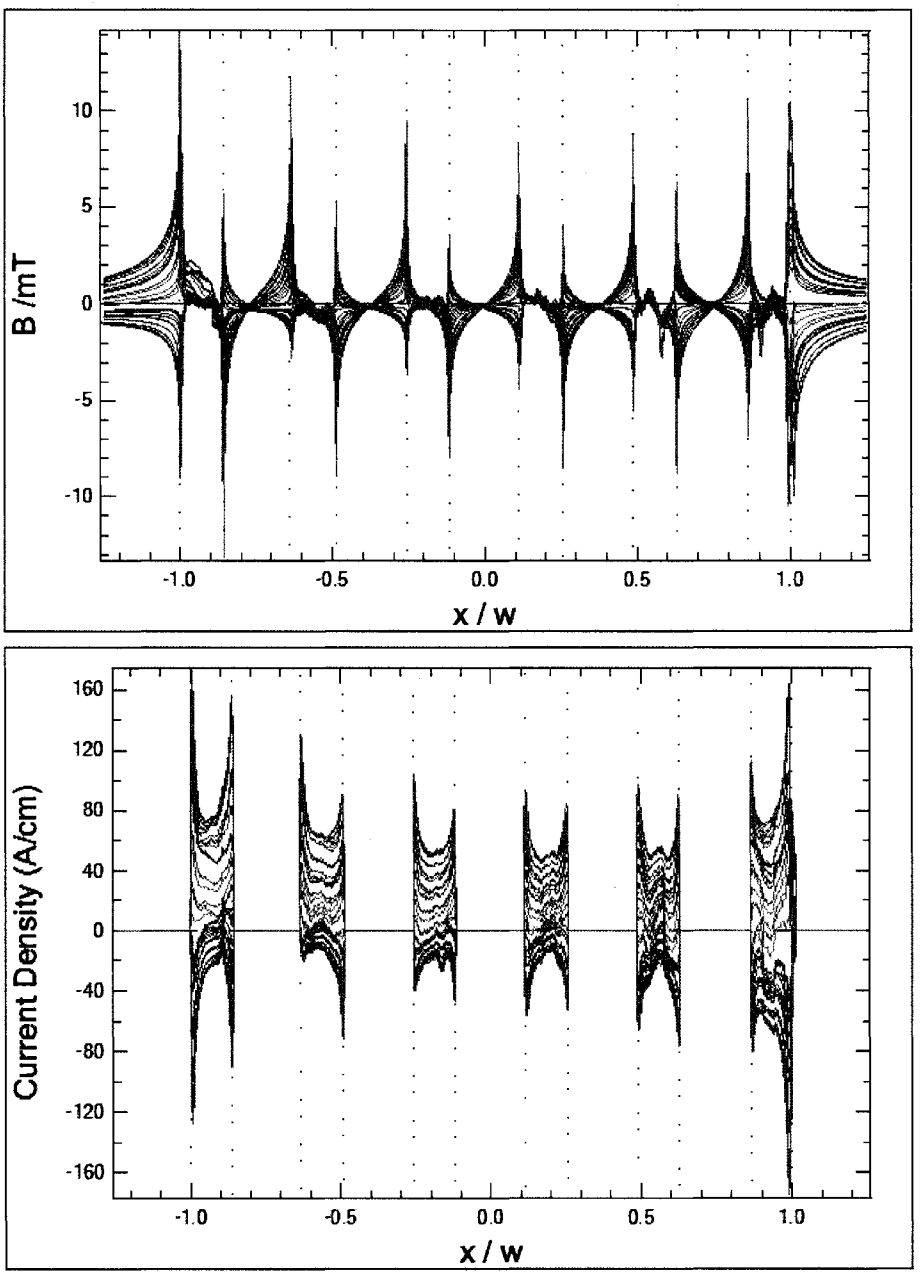

Figure 5.4: The magnetic field distribution (top) and the total current distribution (bottom) for the multifilamentary YBCO sample while only applying a transport current ($I_{peak} = 8$ A) without any external field ($B_a = 0$ mT). The total current density distribution is also the transport current density distribution. The positive and negative ac current cycles are colored in cyan-magenta shades. The vertical dotted lines indicate the edges of each filament.

Since no magnetic field is applied in the $z-$direction of the film, no self-screening currents are induced by the external magnetic field. The transport current density distribution represents the total current density distribution. The noise and artifacts are set to zero in the regions between each superconducting filaments. In the TRMOI experiments, the strong variations in the center of the filaments are considered noise since the signals are weak when there is no external field. Applying the Biot-Savart law to the current density profiles, one can obtain the reduced-noise magnetic field profiles as shown on the top of Fig. 5.3. In the center of the $4th$ and the $5th$ superconducting filament, the magnetic field profiles fluctuate vigorously. The slope of the calibration curve (see Fig. 3.8 in chapter 3) is very steep at low intensities, which means a little change of the intensity will lead to a large change of the magnetic field value. This behavior causes the strong fluctuations on the magnetic field profiles.

In another set of measurements, we reduced the peak value of the ac transport current to $I_{peak} = 4$ A of the same frequency $f = 1000$ Hz. Meanwhile, we also applied a high perpendicular dc magnetic field, $B_a = 10$ mT. Similarly, we call this set of measurements *M410*. All the other experimental parameters are the same as for the *M80*. The 51 magnetic field profiles are plotted on the top of Fig. 5.5. The lime green and fire red colors shade the two half-periods of the ac current cycle. In the middle panel of the figure is the total current distribution calculated from the inverse Biot-Savart law. Outside of the six superconducting filaments, the unphysical currents are set to zero. At phase points $\phi = 0°, 180°$ and $360°$, there is no transport current flowing and the total current densities are the shielding current (induced by the external field) distribution. Subtracting the shielding current density from each of the total current density profiles yields the transport current density distribution is shown in the bottom panel of Fig. 5.5. The validity of this method is confirmed in section 4.3.3.

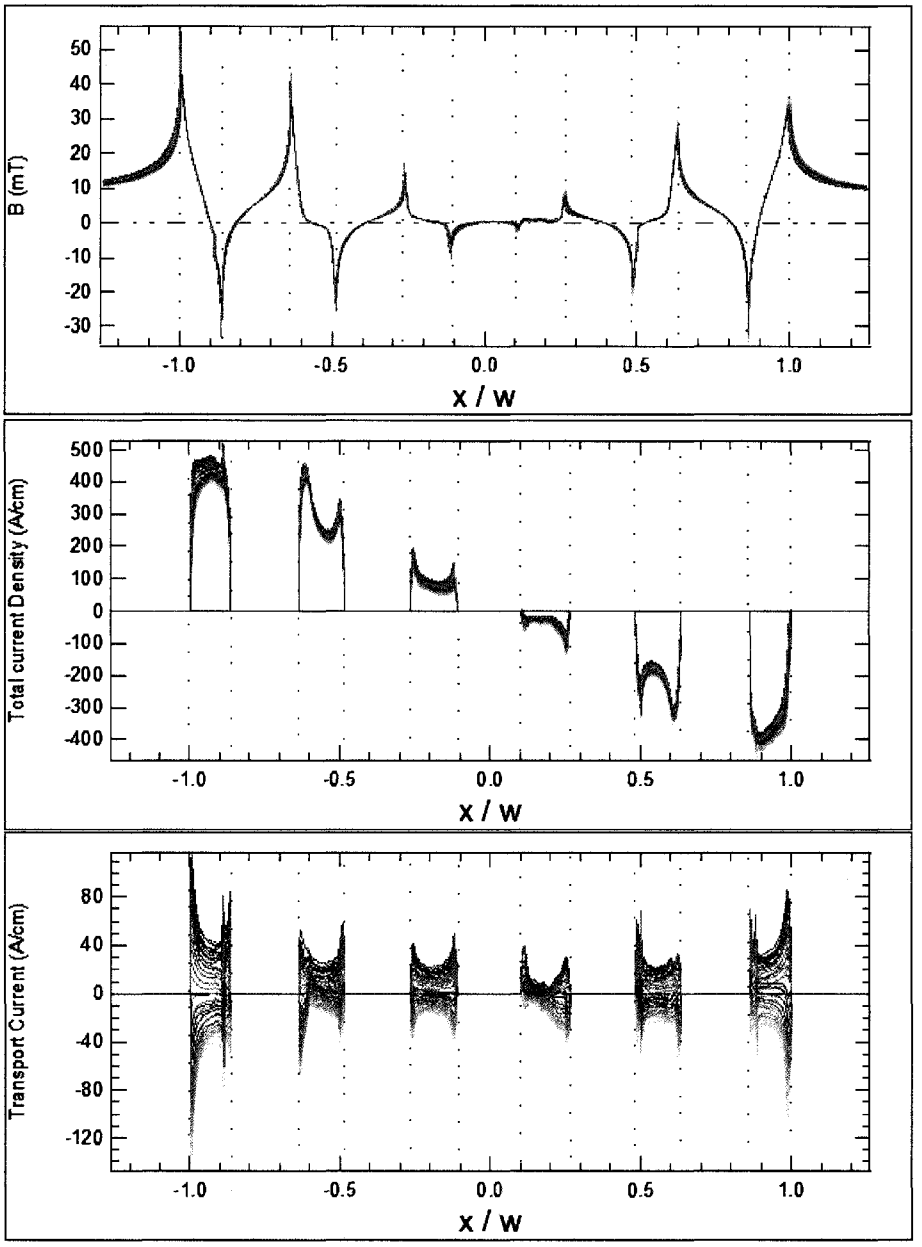

Figure 5.5: The magnetic field distribution (top), the total current distribution (middle) and the transport current distribution (bottom) of the multi-filamentary YBCO sample with an ac transport current ($I_{peak} = 4$ A) flowing and an external field ($B_a = 10$ mT). The positive and negative ac current cycles are colored in limegreen-firered shades. The vertical dotted lines indicate the edges of each filament.

To quantitatively judge the current density profiles shown in both Fig. 5.4 and Fig. 5.5, we integrate the transport current density (for *M80*, it's also the total current density) of each filament and sum them all. This should yield the ac current we initially applied in the experiment. The results of such integration are shown in Fig. 5.6. They both have the correct wave form, but the amplitude is approximately 40% of the applied ac current. For *M80*, the low light intensity and resulting low signal-to-noise ratio can explain the large discrepancy. For *M410*, the big error occars because of the relatively high external field and low ac transport current. The phase of the ac current varies less with the intensity profiles while a large static shielding current is present. This can be easily seen in the top panel of Fig. 5.5. In *M410* the changes from the maximum to the minimum are very weak and the lime green curves almost overlap with the fire red curves. In the *M80* curves shown in the top panel of Fig. 5.4, where the two colors of cyan-magenta shades can be easily distinguished. The small differences in *M410* show sensitivity when we analyzed the intensity differences of the TRMO images. For better results, we optimized our experimal parameters.

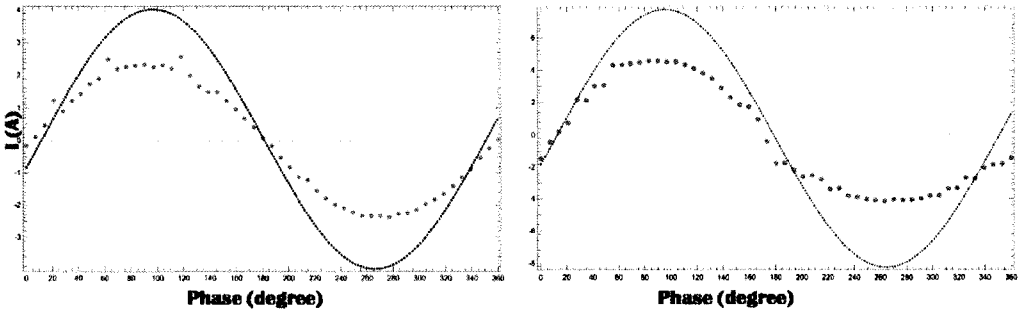

Figure 5.6: The integrated transport current (dots) plotted with the applied transport current (dashed black lines) for the left - with an ac transport current ($I_{peak} = 4$ A) flowing and an external field ($B_a = 10$ mT), and the right - with ac transport current ($I_{peak} = 8$ A) flowing without any external field ($B_a = 0$ mT), respectively.

5.3.2 The optimized measurement

We cut the external perpendicular magnetic field to half, $B_a = 5$ mT, of what we used in *M410* which produced enough signal, but not too much shielding current to disturb the transport current effects. Under this static field, we increased the ac transport current peak values from $I_{peak} = 4$ to 8 A at fixed frequency $f = 1000$ Hz. The $I_{peak} = 8$ A was the highest current we could possibly apply to the film, since the sample would burn when $I_{peak} = 9$ A was used in the measurements. A total of 51 phase points were captured with the time resolution of 20 μs. We refer to this measurement as *M85*.

The phase dependent quantitative analysis

The one dimensional light intensity profiles in arbitrary units averaged over the sample center area (as shown in Fig. 5.3) for all the phases are plotted in Fig. 5.7. The vertical dotted lines indicate the edges of each superconducting filament, numbered from 1 to 6. The positive and negative half-period of the ac current are distinguished in blue-black-red shades. Compared to the shielding current, the transport current is large in this measurement. Thus the ac current was able to cancel out the shielding current on one side. It was even strong enough to change the sign of the total current flowing on the edge.

It is difficult to illustrate the phenomenon of the light intensity profiles since intensity does not change its sign. The intensity profiles are supposed to be *negative* at corresponding filament edges, depending on the current direction , and are also displayed as positive. The effect occurs at the right edges of filaments 1 and 2 and the left edges of filaments 5 and 6. There is not enough ac current in the two center filaments 3 and 4 to change the sign. The inset is an enlargement of the left edge of filament 5 for a clear view. To get this calibration correct, we will need to use the

negative part of the calibration curve shown in Fig. 3.8, which is discussed in section 3.3.

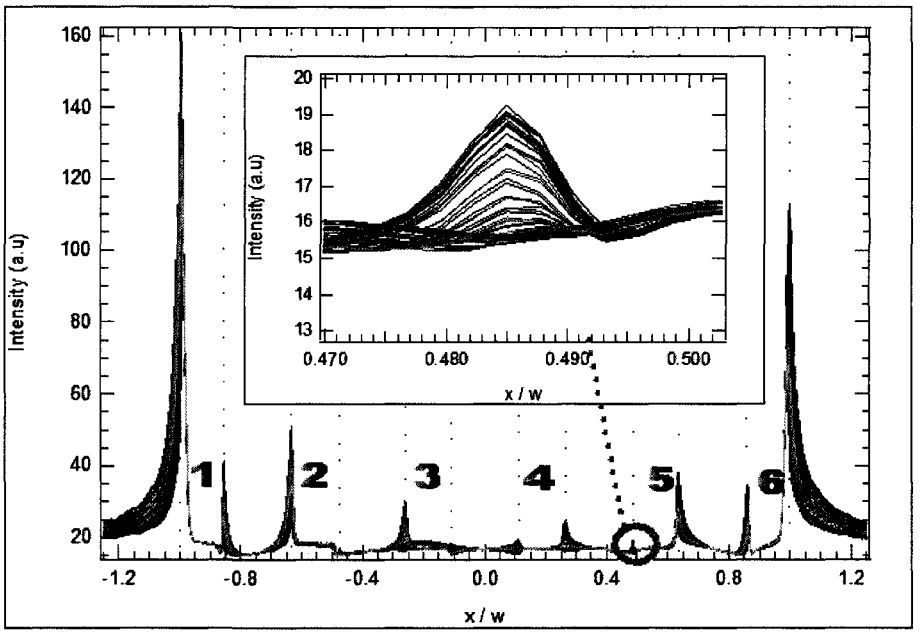

Figure 5.7: The cross section intensity profiles of the multi-filamentary YBCO sample with an ac transport current ($I_{peak} = 8$ A) flowing and an external field ($B_a = 5$ mT). The inset shows an example of the peaks at certain filament edge that need to use the extended calibration procedure to get the correct magnetic field profiles. The positive and negative ac current cycles are colored in red-black-blue shades.

Figure 5.8 (top) is the magnetic field distribution of measurement *M85* calibrated from light intensity profiles. The magnetic field changes its sign and amplitude with the phase evolution of the ac current. One expects that at the phase $\phi = 270°$, filament 1 (red) has same peak height as filament 6 (blue) at the phase $\phi = 90°$, but the red curve has a slightly higher peak than the blue. The reason could be material quality since such asymmetry is found in all the measurements. It is not due to inhomogeneous light intensity distribution because the images are background corrected and the light intensity profiles are normalized. The positive field has higher absolute values then the negative field because the external field is static and always contributes to the positive field.

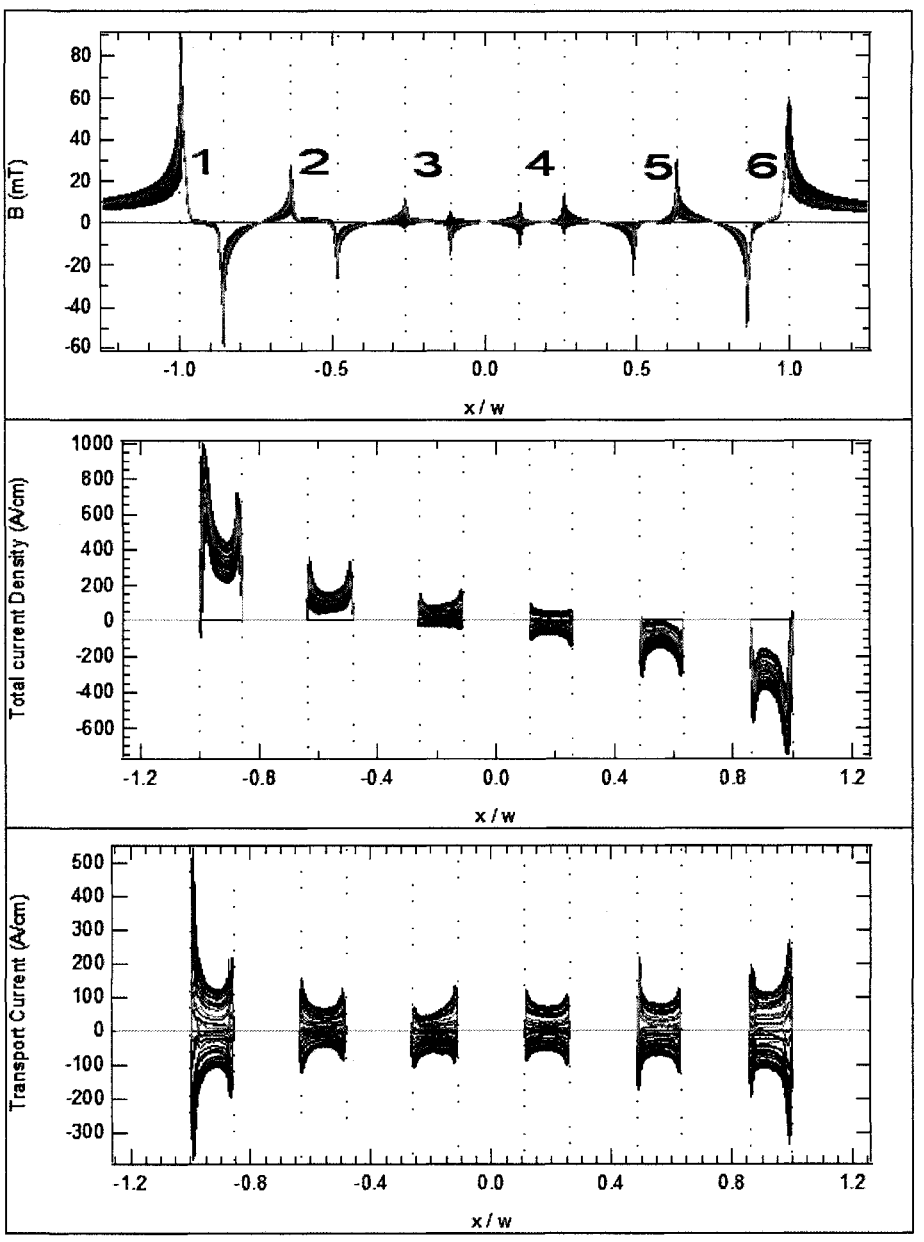

Figure 5.8: The magnetic field distribution (top), the total current distribution (middle) and the transport current distribution (bottom) the multi-filamentary YBCO sample with an ac transport current (I_{peak} = 8 A) flowing and an external field (B_a = 5 mT). The positive and negative ac current cycles are colored in red-black-blue shades.

The total current distributions are shown in the middle panel of Fig. 5.8 as obtained from the magnetic field distributions by the numerical inversion of the Biot-Savart law. Most of the total current is flowing in the positive $y-$direction in the first 3 filaments. Then then current sign changes to negative in the last three filaments. The material quality asymmetry is also observable in the total current distributions where the current profiles at all phases give higher absolute values in filament 1 than filament 6. For all 51 different phase profiles, the unphysical current flowing outside of the six superconducting filaments are set to zero. Because of the optimized experimental parameters in this measurement, there is not much current set to zero, which can be estimated in the intensity profiles shown in the Fig. 5.7. In the non-superconducting areas, the light intensity profiles are very close to the lowest light intensity - the black level.

The transport current distributions are calculated by subtracting the shielding current (which is the total current density at zero phase point) from the total current are shown in the bottom panel of Fig. 5.8. As expected, in the positive half-period, only positive current (red shades) flows through all six filaments, and vice versa. The positive and negative currents are almost symmetric for all the filaments except the first, in which there is a high peak at the maximum phase.

Figure 5.9 is the integration of the transport current flowing in all six filaments at each phase points, indicated as red dots. The integration value at the minimum is $I_{tr} = -7.72$ A, and at the maximum is $I_{tr} = 8.33$ A. The applied ac transport current (the black dashed line) in the experiment is 8 A at peak, which shows a very good agreement with our measured data. The average error is as small as 3.81%. The measured data also reproduces well the applied current wave form with little phase shifting (less than 3°). This result quanlitatively proves the sucess of our TRMOI measurement of the multifilamentary film and the good optimation on the

experimental parameters.

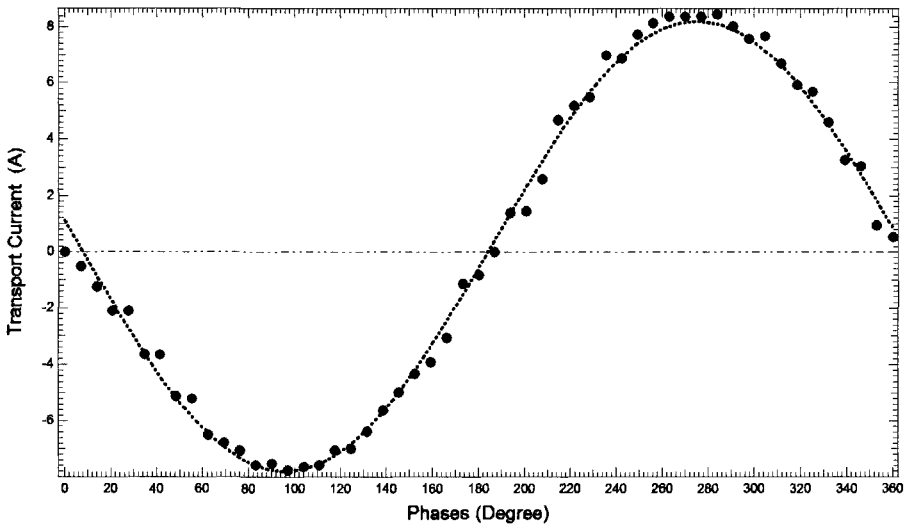

Figure 5.9: The integrated transport current (red dots) when applying an ac transport current ($I_{peak} = 8$ A) and an external field ($B_a = 5$ mT), which agrees fairly well with the applied ac current (the dashed black curve).

To further investigate the transport current distribution in each filament, we integrate the transport current in filament 1 to 6 for each phase. For example, at the phase point $\phi = 90°$, the transport current amplitudes in the filaments are: $I_{tr1} = -1.96307$ A, $I_{tr2} = -1.96$ A, $I_{tr3} = -0.88$ A, $I_{tr4} = -1.01$ A, $I_{tr5} = -0.90$ A, $I_{tr6} = -1.86$ A, which sums to 7.72 A. At another phase point $\phi = 318.5°$ when the transport current is about 70.34% of the peak value, and in each filament the transport current distributes as :$I_{tr1} = 1.46$ A, $I_{tr2} = 0.67$ A, $I_{tr3} = 0.60$ A, $I_{tr4} = 0.73$ A, $I_{tr5} = 0.86$ A, $I_{tr6} = 1.32$ A. We calulate the percent of the transport current flowing in every filament at every phase point and calculate the average. The result is plotted in Fig. 5.10. The clustered cylinder style plot clearly shows that most of the transport current (nearly 50%) flows in the two outer filaments, and then almost equally distributed in the inner four filaments. The first filament has slightly more current (2.2% more) flowing than the last filament due to the better superconducting properties of the material of the filament. Adding the transport current flowing in the first three

filaments 1, 2 and 3 (49.38%), and the other three filaments 4, 5 and 6 (50.63%), one finds that there is almost equal current flowing in the two sides of the film.

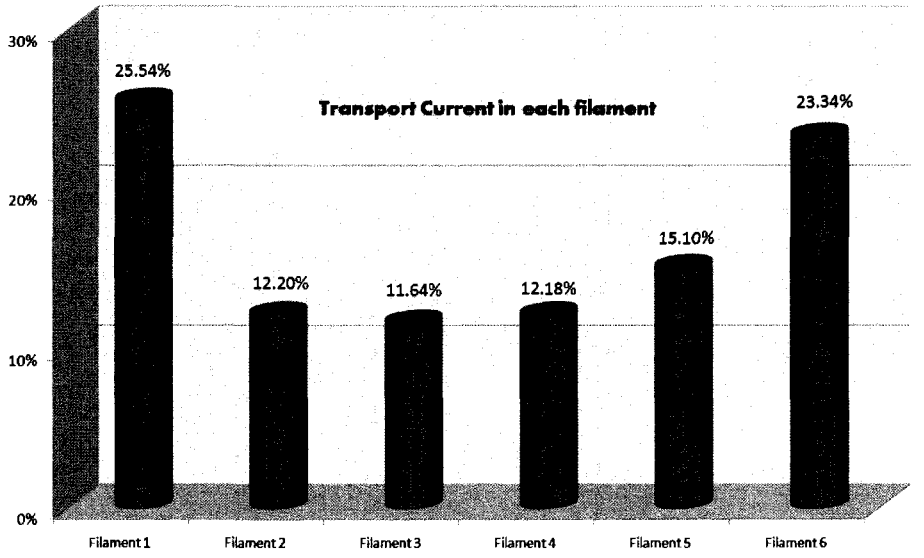

Figure 5.10: The integrated transport current for each filament labeled by percentage of the applied transport current plotted in clustered cylinders.

Comparison with theoretical models

For the multifilamentary films, when filaments are not coupled, the current flows inside the filament and is expected evenly distributed in each filament. On the other hand, when filaments are coupled, the current flows across the transverse resistance between filaments as shown in Fig. 5.11[71].

Figure 5.12 is the transport current distribution (solid lines) at two extreme phase points, $\phi = 90°$ and 270°, of the measurement *M85*, which clearly shows the six filaments are coupled in our experiment. This is also quantitatively proved by calculating the amount of current flowing in each filament. To further confirm the result, we use the modified critical state model in the situation of simultaneously applied ac current and static field in a thin film geometry superconductor. The blue and red dashed lines are the modified CSM fitting curves for a single-bridged sample, which gives an

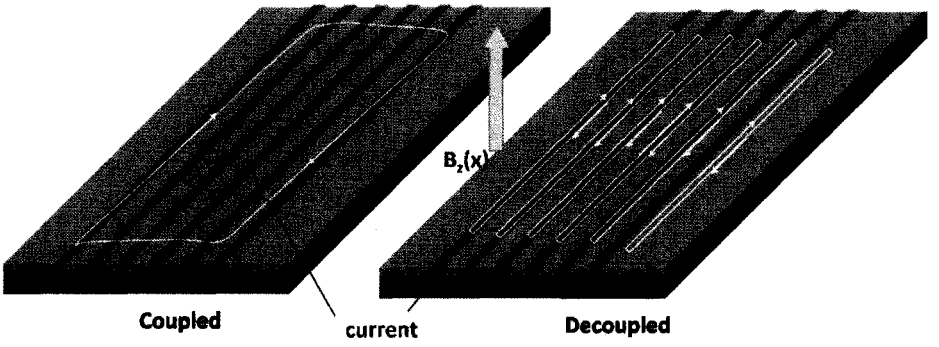

Figure 5.11: A schematic drawing of the filaments coupling. Left, filaments are completely coupled and the right, when they are completely decoupled.

overall current density distribution shape of all filaments. The green dotted curves are the modified CSM fittings for individual filament, which agree fairly well with our measured data in shape and amplitudes. One integrates the green curves and obtains theoretical values of the transport current in each filament at the phase point $\phi = 270°$: $I_{tr1} = 2.50$ A, $I_{tr2} = 1.39$ A, $I_{tr3} = 1$ A, $I_{tr4} = 1.4$ A, $I_{tr5} = 1.5$ A, $I_{tr6} = 2.2$ A. Compared to the transport current values we calculate from the measured data, the average error is approximately 15%.

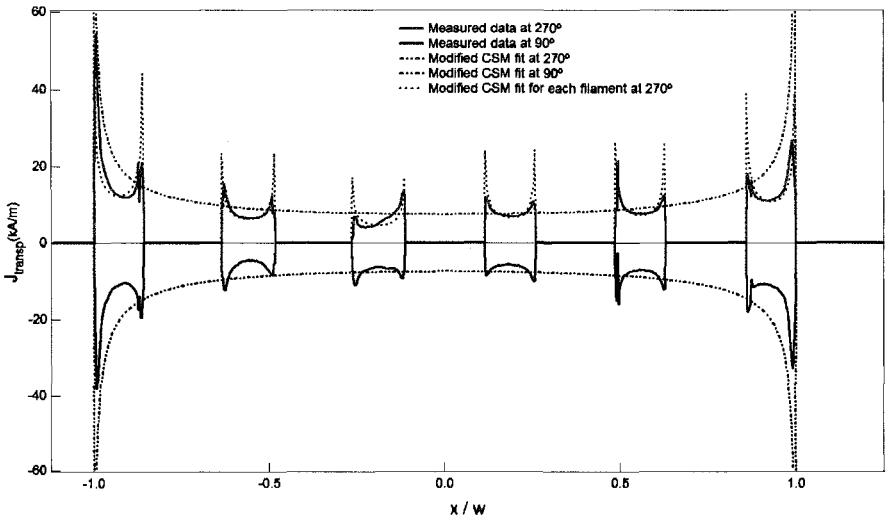

Figure 5.12: The transport current density at two extreme phase points in a comparison with the modified CSM.

We also compare our measured data with FEM simulation data. The simulation

are performed by Dr. Francesco Grilli at Los Alamos National Laboratory. The FEM calculations are plotted in Fig. 5.13. The top is the magnetic field distribution and the bottom is the total current distribution. The parameters for the FEM simulation are the same as we used in the measurement: $B_a = 5$ mT, $I_{peak} = 8$ A at 1000 Hz. One tricky parameter to adjust in the simulation is the critical current density J_c. We first tried a $J_c = 1.7 \times 10^7\ Acm^{-2}$ that is the same J_c of the single bridged YBCO thin films. With this J_c, the simulation shows a much further flux penetration in the filaments than the measured data. After a couple of attempts on finding a proper value of J_c (since each simulation requires a very long calculation time depending on the processing speed of the computer), we use a $J_c = 4.1 \times 10^7\ Acm^{-2}$, more than twice the value of the thin film. The results shown in Fig. 5.13.

We choose three phase points of $\phi = 90°$ (blue), $\phi = 270°$ (red) and $\phi = 180°$ (green) of our measured data (solid lines) to plot with the same phase points of the FEM calculations (dashed lines). The comparison of the magnetic field distributions is shown at the top of Fig. 5.14, and the comparison of the total current density distribution is shown at the bottom. The profiles match pretty well for the field distributions. The peaks are higher in the FEM simulation than the measured data. In the top panel, the measured field penetrates further inside of the superconducting filaments. This feature reflects in the current distribution figure too. For example, in the center of the first filament, the saddle shape total current density profiles have lower values for the FEM simulation than the measured data. This implies that the J_c used in the FEM simulation is a little higher than in the experimental data. The FEM simulation also have higher absolute peak amplitudes than the measured data, which also means that the FEM simulation data have slightly higher J_c. However, the multifilamentary data yields a critical current density at least twice as large as the J_c of the single bridged YBCO thin films is a significant advantage of the

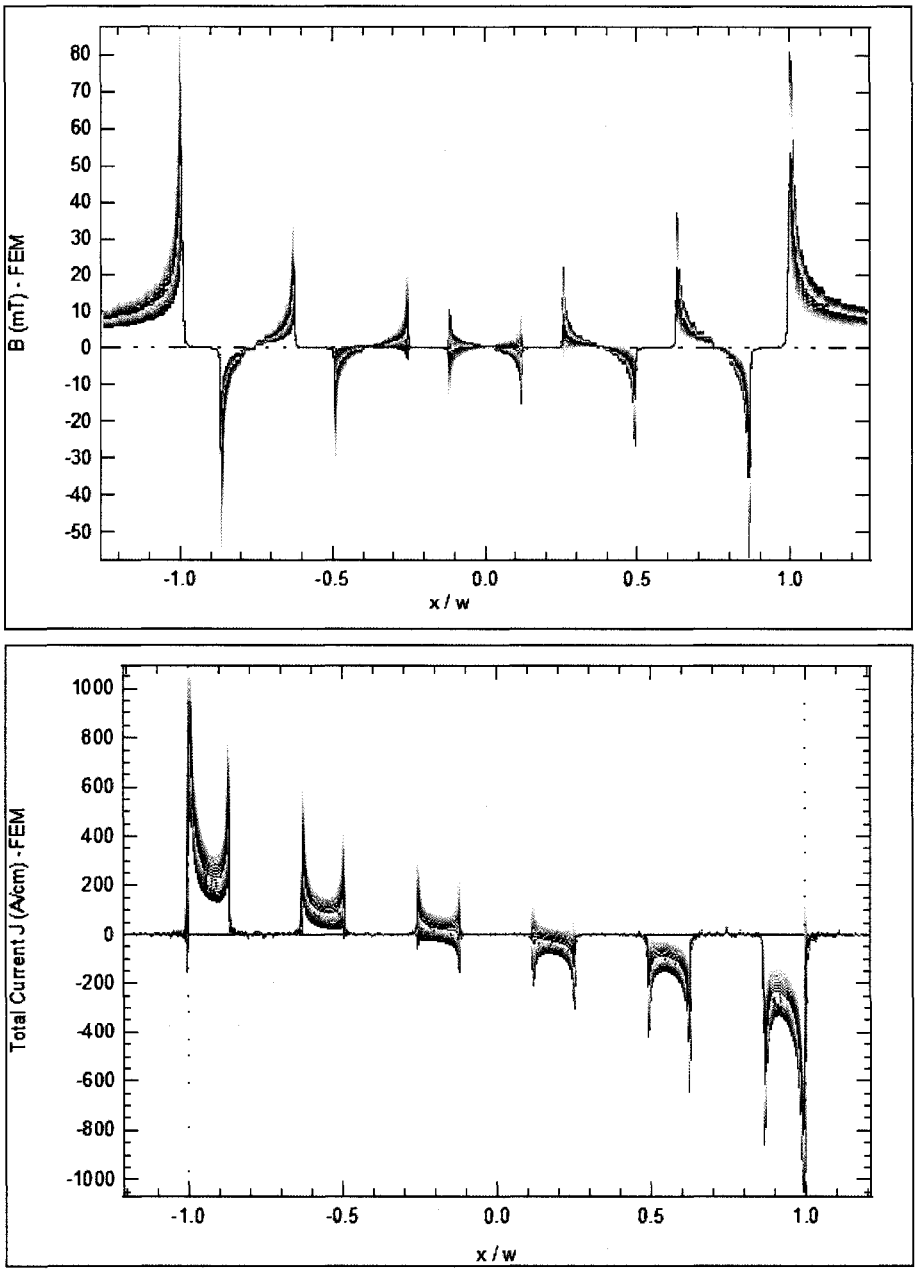

Figure 5.13: The FEM simulated data of applying an ac transport current (I_{peak} = 8 A) and an external field (B_a = 5 mT). The top - the magnetic field distribution and the bottom - the total current density distribution. The positive and negative ac current cycles are colored in red-yellow-blue shades.

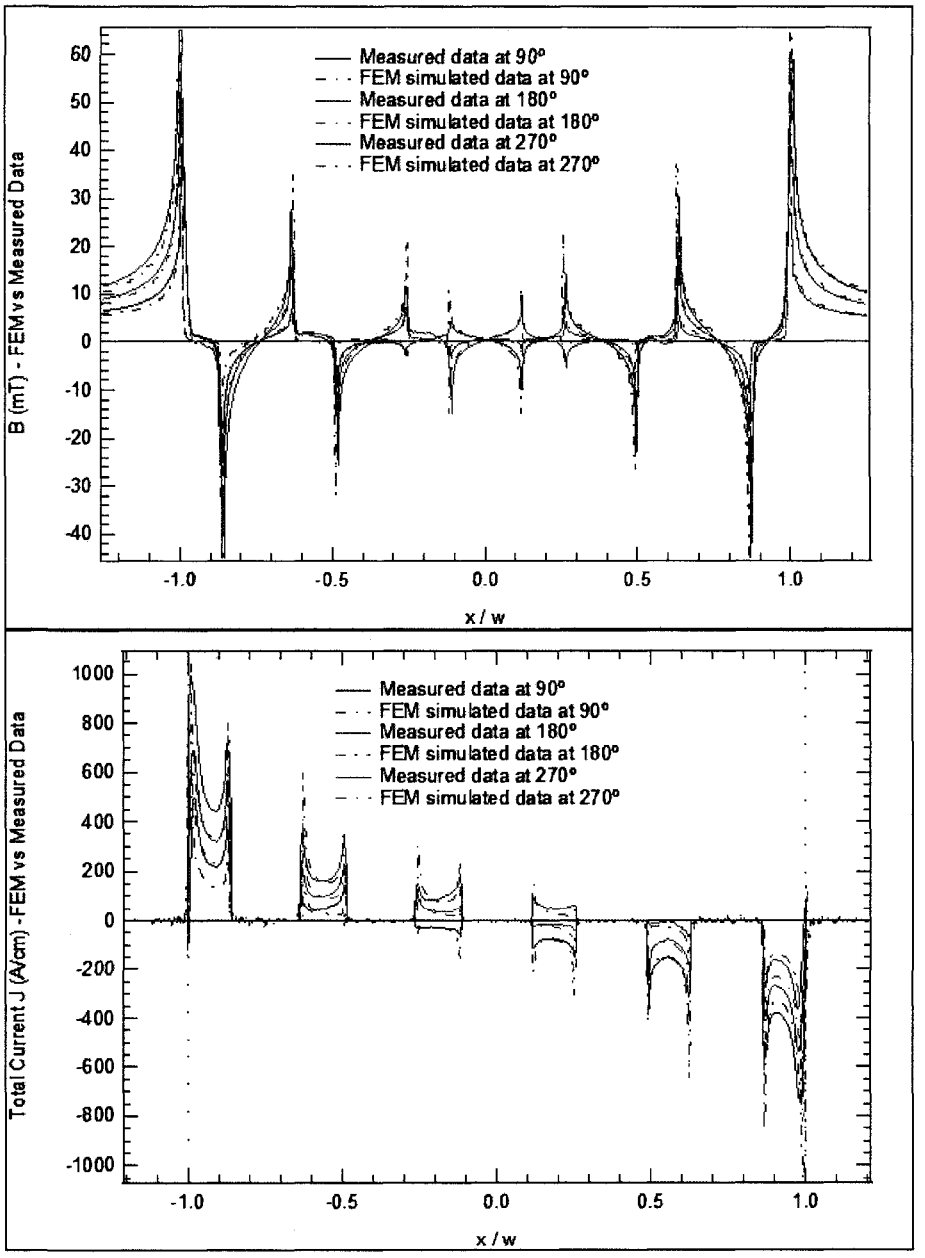

Figure 5.14: The measured magnetic field (top) and total current density (bottom) distribution(solid lines) comparing with the FEM simulation(dashed lines) at $\phi = 90°$ (blue), $\phi = 270°$ (red) and $\phi = 180°$ (green) phase points

multifilamentary film.

5.4 Conclusion

In conclusion, we use the TRMOI technique to measure multifilamentary YBCO thin film samples with different experimental parameters. If we apply an ac transport current without any external magnetic field, the light intensity is low and results in a lot of noise in the images. If we apply a low amplitude ac transport current in a relatively high external magnetic field, the large shielding current induced by the static field reduces the effect of the transport current and not much phase dependent variations are observable. Both situations are not ideal for the TRMOI technique since the phase dependent measurements are sensitive to the differences in each image.

To optimize the experimental parameters, we apply a lower external dc field of 5 mT which produces enough signal but does not induce a large shielding current to reduce the transport current variations. A maximum ac transport current with peak value of 8 A is sent through the sample. A quantitative data analysis proves that our data agrees fairly well with the real experimental values. We also find that half of the ac transport current flows at the most outer two filaments while the inner four filaments share roughly same amount of the rest of the transport current. The filaments are coupled with each other in the experiment. This is confirmed quantitatively by integrating the transport current in each filament, and the results agree fairly well with the modified CSM. Compared the FEM simulation with our measured data shows that the multifilamentary films have at least twice the critical current density J_c than the single bridged YBCO thin films.

The ultimate goal in striating the YBCO coated conductor films is to reduce their ac losses and to increase their critical current density. Coated conductors are often used in ac power units but are subject to high hysteretic loss. To map such loss we will need to calculate the electric field distribution[77,78], which will be future work.

Chapter 6

The second generation (2G) superconductors - coated conductors

6.1 Introduction

Many applications of high-temperature superconductors require long wires that are able to carry large amounts of current. The first generation HTSC wires made of BSCCO have well developed manufacturing technology, and high-quality BSCCO tapes are available commercially in kilometer length with the critical current I_c up to 150 A[79]. However, the BSCCO wires are not used for large scale replacement of conventional copper or aluminum conductors[80], because of the high cost of bismuth and the high amount of silver; and it carries much less current in strong magnets unless the temperature is lowered close to absolute zero[81,82], but lowering the temperature limits its advantage over LTS materials.

In 1995, researchers at Los Alamos National Laboratory and Oak Ridge National

Laboratory[7] invented a new HTSC tape using YBCO. This new tape can carry a current density of $J = 10^6 Acm^{-2}$[83,84]. However, the engineering current density is lowered than YBCO films[12,85] due to the very thin superconducting layer compared to the substrate. YBCO's cheaper starting materials and better ability in high magnetic fields, this novel second generation HTSC wire, also referred to as *coated conductor (CC)* can be advantageous in many traditional copper-wire-based high power and transport applications, resulting in large cost reduction and energy savings. The introduction of flexible metallic substrates onto which epitaxial thick films can be grown made it possible to use the excellent superconducting properties of YBCO up to 77 K.

In recent years, significant progress has been made for application of the coated conductor wires. The length of the coated conductor has reached 350 m in 2006, and such chilled high-temperature superconducting cable is delivering electricity at three to five times the capacity of copper in Under Albany, New York and a 600-meter span of 138 kV HTS cable is being prepared to power part of Long Island. Actually because the manufacturing success in depositing nearly single-crystal layers of YBCO onto nickel-alloy flexible tapes: two major superconductor manufacturing companies in the US, AMSC and SuperPower Inc, have both abandoned BSCCO[86].

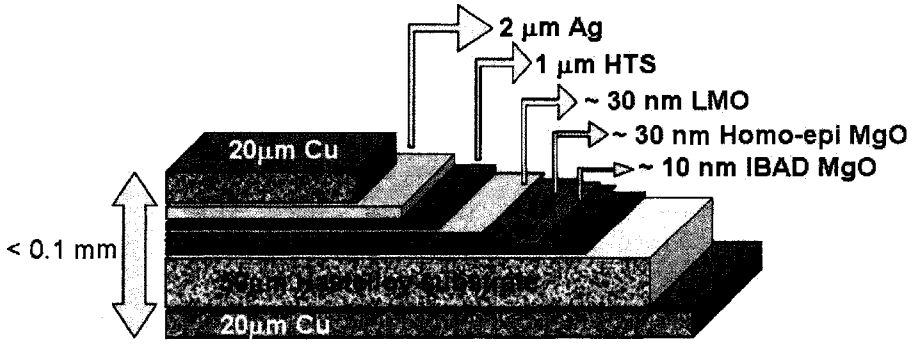

Figure 6.1: The configuration of SuperPower 2G HTS Wire fabricated by an automated, continuous process using thin film deposition techniques to apply the superconducting material on buffered metal substrates.

SuperPower is now routinely manufacturing long lengths (600 m plus) of robust and high performing 2G HTS wire (coated conductors), based on YBCO (yttrium barium copper oxide). This 2G HTS wire is fabricated by an automated, continuous process using thin film deposition techniques, such as those used in the semiconductor industry, to apply the superconducting material on buffered metal substrates.

Scaling up the length of the wires are still the major challenge for the field. YBCO's various shaped grains make it much harder to orient than the plate-like grains in BSCCO. Researchers and companies use different techniques to coat a nickel wire with ultrathin layers of materials that orient the YBCO grains as they grow on top. The two primarily used manufacturing processes used to grow coated conductors are ion beam assisted deposition (IBAD) and rolling assisted biaxially textured substrates (RABiTs). IBAD relies on texturing the buffer layers between the YBCO and the metal substrate, while RABiTS textures the metal substrate and then grows the superconducting layer epitaxially onto the biaxially aligned template. Figure 6.1 is a scheme of the YBCO coated conductor configuration by SuperPower Inc.[87].

Magneto-optical experiments have strongly contributed to the analysis of current-limiting features like cracks, grain boundaries and precipitates in technical materials, such as coated conductors[88], tapes and melt-textured bulk samples[89]. Our TRMOI technique offers a quantitative understanding of the current distribution of such coated conductors, especially in regions with inhomogeneous current density distributions and grain boundaries. In the TRMOI technique, the time evolution of flux pattern in coated conductors has to be taken into account. It has been shown experimentally[35] that electric field pattern and the related time decay of the current pattern in CCs are strongly inhomogeneous.

6.2 Experimental

The samples used in our experiment are small pieces of coated conductors produced by Superpower Inc. with the IBAD technique. The coated conductor is made of several layers deposited over a Hastelloy - C metal tape substrate, which gives a very smooth surface for the YBCO superconducting layer's growth. The HTSC layer is very thin (about $1 - 2\mu m$). The average critical current is $J_c = 100 Acm^{-1}$-width at 77 K in self-field for tapes about 100 m in length. The J_c values vary from $60 - 193 Acm^{-1}$-width along the tape length at alternating intervals. Increasing the film thickness can decrease the critical current density[85].

The standard width of the CC tapes is 12 mm. Our CC samples are several pieces of 10 mm long cut along the tape transversal direction, and then the pieces are reduced from $10 \times 12 mm^2$ to a strip of $10 \times 1 mm^2$ with a thickness of 0.5 mm by laser ablation. The laser ablation creates straight edges with roughness estimated from SEM images up to a few microns. The laser processing does not affect significantly the critical current values of the strips that range from 8 to 12 A. For a good TRMOI investigation, the silver cap coating of each CC sample must be removed. We use a mixture solution of methanol, hydrogen peroxide and ammonium hydroxide with the volume ratio of 4 : 1 : 1 for the etching purpose. This mixture solution should be made up fresh before the etching. Compared to the YBCO thin film samples, the coated conductor tapes have rougher sample edges and much narrower width. One has to apply the delicate MO indicator carefully onto the sample surface to avoid scratches. One needs to choose the proper width of the indicator to prevent the indicator wobbling on the CC sample and , that creates uneven light illumination.

In the MOI experiments, the CC sample is first zero-field cooled down to 25 K and then an external magnetic field is applied normal to the sample surface. For time dependent measurement, an ac current with peak value $I_{peak} = 3.7$ A is sent along the

$y-$ direction of the sample. TRMO images are taken at discrete values of the phase angle $\phi = 2\pi f \cdot t$ with a time resolution of 40 ms. The applied dc field is 19 mT. In current dependent measurement, the dc current is ramped up from $0 - 3770$ mA along the $y-$direction of the sample, and an external field $B_a = 10$ mT is applied.

6.3 Results and discussions

6.3.1 Inhomogeneous flux penetration

Figure 6.2 shows seven time-resolved MO images of the CC sample from $\phi = 90°$ to 270°. The images are focused on the sample center, and enhanced in color contrast. The images are taken at $f = 1000$ Hz and $I_{peak} = 3.7$ A. The dark spots on the images are caused by the MO indicator's small defects. The bright yellow areas near the sample edges represent regions with the maximum density of magnetic flux, and the darkest part in the center is the flux-free region. The magnetic flux penetrates from the edges further inside the sample as the phase changes from $\phi = 90°$ to t$\phi = 270°$. The bight yellow area shifts from the lower edge in the first image to the higher edge in the last image.

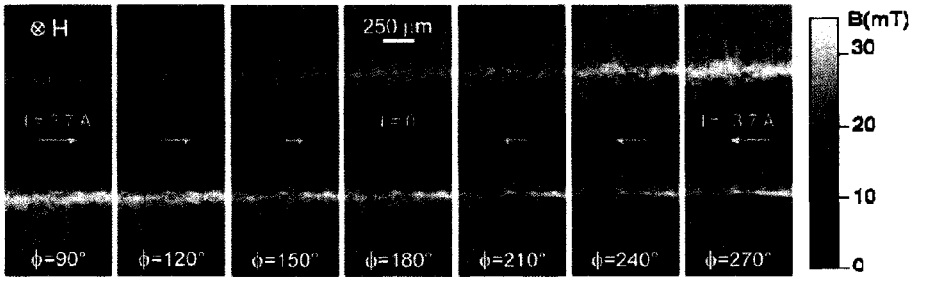

Figure 6.2: TRMO images of a YBCO coated conductor for different phase points of the applied ac current in a perpendicular magnetic filed $Ba = 19$ mT.

Inhomogeneous magnetic flux distributions are observed for all the phases shown in Fig. 6.2, consisting of a non-uniform flux front penetration inside the sample and

an asymmetric flux evolution at the edges. At $\phi = 180°$, the latter effect is very clearly visible, as one would expect from a symmetric distribution when there is no transport current flowing in the sample. From the MO images, one can find that the magnetic flux will leak through the network of grain boundaries, strongly affecting the magnetic and transport properties of coated conductors[35]. However, in the TRMO imaging studies of YBCO thin film we discussed in Chapter 4, we reported a symmetric phase evolution of the magnetic flux[29].

Figure 6.3 shows a series of MO images of the coated conductor as a function of applied dc current from $I = 2420$ mA to 3770 mA. The external applied field is half of the value in the phase dependence measurement in order to emphasize the effect of the transport current. The images are enhanced with color contrast. As the dc current increases, the flux front penetrates further inside the sample in a finger-like pattern. Each finger has relatively sharp edges at lower current ($I = 2420$ mA), and starts to grow wider with increasing current ($I = 3000$) mA. At the highest current $I = 3770$ mA, the finger tips are rough and each finger's border is not as sharp as before.

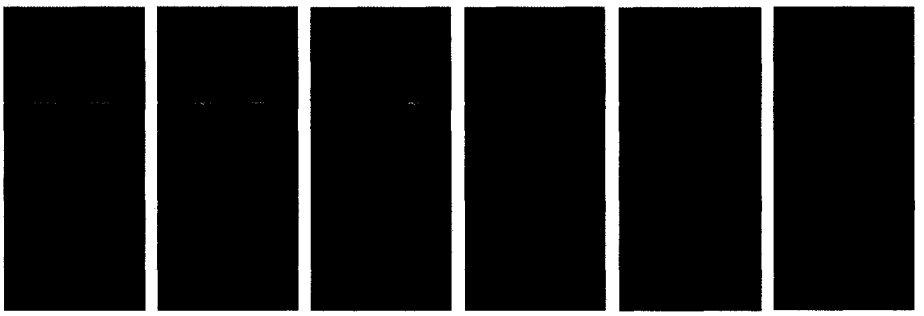

Figure 6.3: A series of MO images of YBCO coated conductor strip with increaing dc current $I = 2420 - 3770$ mA and an external magnetic field $B_a = 10$ mT.

The current increases the sample temperature locally and triggers thermal instabilities. This effect is very clear in Fig. 6.4, which shows the MO image of the CC at $I = 3770$ mA. In this image, we can see the flux avalanches, especially on the right

hand side of the image, where a defect (the bright yellow spot) exists right at the lower sample edge. Around that defect, the finger-like pattern of flux turns into a blurry cloud. Due to the lower critical current density property of CC compared to the YBCO thin film, $I = 3770$ mA was the highest current we could apply in that experiment. Applying even higher current to the sample either burns the sample or locally heats the sample too much, thus losing the superconductivity.

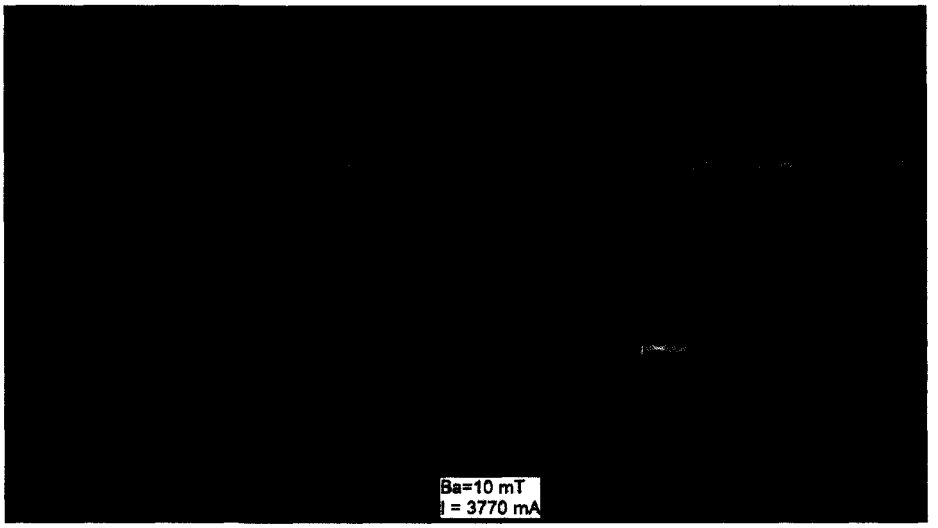

Figure 6.4: The color contrast enhanced MOI image of YBCO coated conductor strip with a dc current $I = 3770$ mA and a dc external magnetic field $B_a = 10$ mT.

6.3.2 Phase dependent quantitative study

To further study the phase dependence of the magnetic flux behavior, the cross-section profiles of the magnetic field over half a period of the ac current averaged along the $y-$direction are plotted in Fig. 6.5. The figure shows mainly the center area of the sample $\left|\frac{x}{w}\right| = 2$. Outside the bridge, the field is equal to the applied field $B_a = 19$ mT. At the sample edges, the peak intensity and position of the profiles change with the phase. At $\phi = 180°$ (the green curve), the field profile due to the self-field of the superconductor is symmetric since the spatial inhomogeneities related to grain boundaries observed in the image (Fig. 6.2) have been averaged out. At

phase $\phi = 90°$ (the red curve), the absolute maximum of the magnetic flux is near the right edge ($\frac{x}{w} = 1$) of the sample. At the other sample edge ($\frac{x}{w} = 1$), the magnetic flux peak corresponding to the relative maximum is shifted further into the sample. The absolute maximum decreases while the relative maximum progressively increases as the phase changes from $\phi = 90°$ to $\phi = 180°$. Such behavior happens also at the phase point $\phi = 270°$ (the navy blue curve).

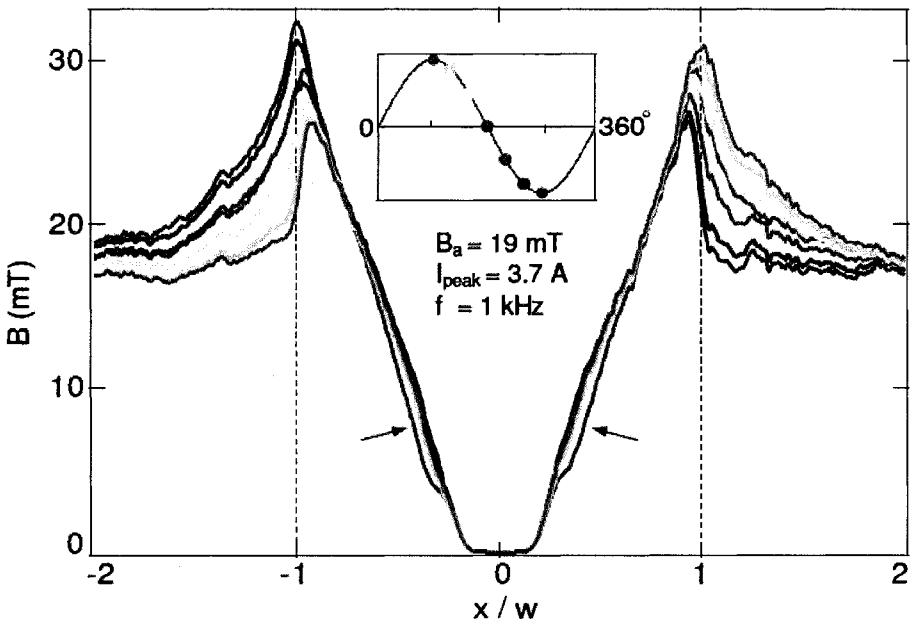

Figure 6.5: The magnetic field profiles for different values of the phase of the applied ac current. The inset shows the phase points chosen in the plot.

The applied current has a peak value of $I_{peak} = 3.7$ A, which is approximately 40% of the critical current (at 77 K) of the CC. Compared to the YBCO thin film experiment, (in which the applied current is $I_{peak} = 8.5$ A with $B_a = 10$ mT) there is less transport current flowing in the sample with twice the external field $B_a = 19$ mT, therefore the transport current has a smaller effect than the shielding current induced by the external magnetic field. The total current density distributions are calculated by the numerical inversion of the Biot-Savart law, and are plotted in Fig. 6.6. To verify the current density profiles quantitatively, one integrates the current desity at

phase $\phi = 90°$ and $270°$ from the left sample edge to the right one ($|\frac{x}{w}| \in [-1, 1]$), and obtains the transport current $I = 3.5$ A and -3.2 A, respectively. The integration results show a good agreement with the applied peak current of $|I| = 3.7$ A with an overal error less than 10%. The deviation can be considered as an effect related to the inherent inhomogeneous flux penetration due to the grain structure of the CCs, and the overall 1D calculation does not completely average out the differences.

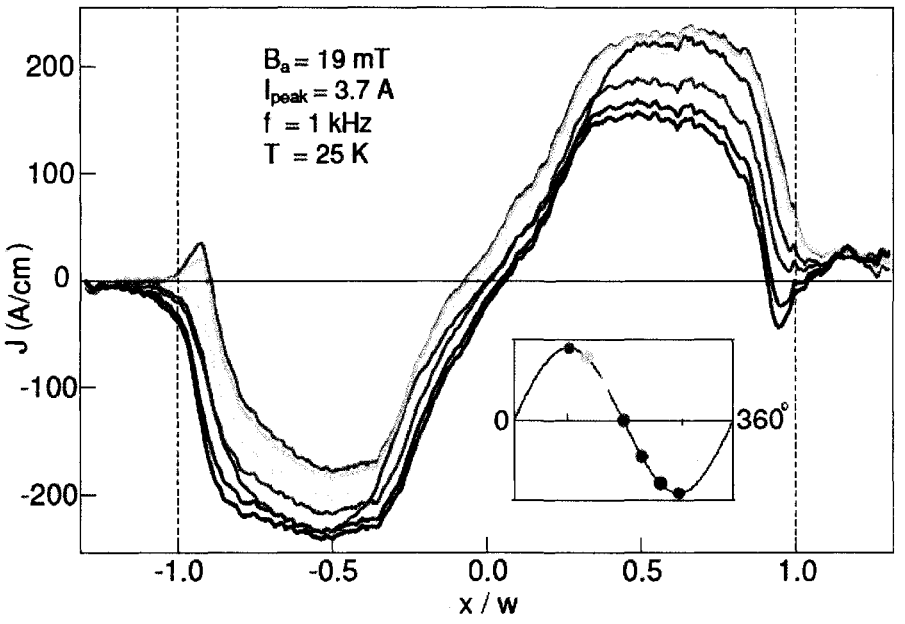

Figure 6.6: The current density profiles for different values of the phases. The inset shows the phase points chosen in the plot.

The current profiles change considerably with the phase. At the phase point $\phi = 180°$ no net current flows through the sample and only the shielding current (the green curve) flows in a closed loop near the sample edges. The zero phase current profile is symmetric and the absolute peak value corresponds to a $J_c = 235 Acm^{-1}$ at 25 K, which is twice the average critical current value at 77 K. At different phases, the ac transport current flows through the sample either in positive or negative $y-$direction according to the polarity of the applied sine wave voltage. The current density profiles can be seen as the sum of the transport current and the shielding current induced by

the magnetic field, and at the 270° phase point, the total current density is equal to the shielding current density.

6.4 Conclusion

In conclusion, we successfully use the TRMOI technique to study the interaction of a perpendicular magnetic field and an applied ac or dc current in YBCO coated conductor. The inhomogeneous flux penetration of CCs due to its large amount of grain boundaries are observed clearly in both phase dependent and dc current dependent TRMOI measurements. For current dependence measurements, a relatively low external field is applied and the flux grows in finger-like patterns. Increasing dc current triggers thermal instabilities of the flux, and a maximum of $I = 3770$ mA is sent through the sample. For phase dependence measurements, time and spatially-resolved images of the magnetic flux profiles are presented at seven phase points (from $\phi = 90°$ to 270°) of the applied AC current. A quantitative analysis of the data allows us to calculate the evolution of the current density with the phase angle. The effect of the ac current is to shift the magnetic flux further inside the sample and to rearrange the overall flux distribution. Small deviations can be observed when the flux inhomogeneities due to the inherent grain structure of the CC samples are not completely averaged out.

Chapter 7

Conclusions

High-temperature ceramic superconductors have drawn a lot of attention since their discovery in 1987. As the most promising HTSC material, YBCO has low cost and good performance in high transport current and high magnetic field conditions. The significant progress made towards the development of the second generation YBCO coated conductors in recent years further opens large applications, especially in ac power devices. It is important to study the ac behavior of such materials.

The new time-solved magneto-optical imaging technique allows us to take MO images of a superconductor at any phase point of an ac transport current with or without applying an external magnetic field. This method advances the normal MOI techniques that only do static measurements. In this dissertation, we study the ac behavior of superconducting YBCO thin films, multifilamentary YBCO thin films and coated conductors using the TRMOI technique. For YBCO thin films, we study the spatial magnetic field distribution in high frequency regions with both an ac current and an external field applied. From a numerical inversion of the Biot-Savart law, we obtain the total current distribution of the thin film. The TRMO images show the phase evolution of the steady state vortex motion driven by the applied ac current. The quantitative analysis reveals two coexistent vortex states: a disordered

dynamic state of plastic motion near the edges of the bridge and a quasi-static glassy state more inside of the sample. This vortex behavior is also revealed in the FEM simulation results. To study the ac transport current behavior, we determine the transport current density by subtracting the shielding current density from the total current density at each of the phase points. We model the transport current density in a modified critical state , and our measured data show asymmetric and pronounced peaks at the edges. We argue that the transport current is distributed in such a way for the purpose of energy minimization. A brief frequency dependent measurement is presented and we conclude that there is no frequency dependence in the frequency range of 100 to 1000 Hz.

The TRMOI study on the interaction of a perpendicular magnetic filed and a transport current on YBCO coated conductors shows inhomogeneous flux penetration due to the large amount of grain boundaries. Clear finger-like patterns are found in both ac and dc transport current measurements, which demonstrate thermal instabilities of the flux that were triggered by the local heating effect of the current. We also quantitatively analyze the phase dependent data while applying an ac transport current and a dc field. The effect of the ac current in the measurement is to move the magnetic flux further inside the sample and to rearrange the overall flux distribution. Due to the grain boundaries of the coated conductor sample, the average over a certain range of the image could not completely diminish the deviations, and flux inhomogeneities are visible even in the 1D profiles.

Because of the high aspect ratio of the coated conductor due to its architecture, the ac loss primarily resulted from high hysteresis loss. This limits its ac power applications or high frequency applications. The idea to reduce such loss is to use the multifilamentary structure of YBCO layer since the amount of heat generated in such striated tape decreases if the width of the filament is reduced. We use our TRMOI

technique to study the ac behavior of a multifilamentary sample with six filaments. To obtain the best quantitative results from the MO images, we chose to apply a low magnetic field and a high ac transport current after comparing different experimental results. The external magnetic field should be high enough to give good signals, but not too high that the induced shielding current may overwhelm the ac transport current. The integration of the transport current of the optimized measurements gives very good agreement with the applied transport current. Quantitatively, most of the transport current flows at the outer two superconducting filaments and the rest of the current distributes almost evenly among the inner four filaments. From the FEM simulation of our data, we conclude that the multifilamentary film exhibits at least a critical current value twice as high as the single bridged YBCO thin film. This behavior is conducive for high-power applications.

The future work is to determine the hysteresis loss in the multifilamentary sample from our data. The electric filed distribution needs to be calculated from the time dependent magnetic field. Furthermore, instead of averaging a certain area of the image, we can calculate a 2D map of the time dependent current distribution by a 2D numerical inversion of the Biot-Savart law[90]. The ac loss thus could be obtained in both $x-$ and $y-$ directions.

Bibliography

[1] R.Ouboter. Heike Kamerlingh Onnes's discovery of superconductivity. *Scientific American*, 276(3):98 – 103, 1997.

[2] J.G.Bednorz and K A Müller. Possible high Tc superconductivity in the Ba-La-Cu-O system. *Zeitschrift für Physik B Condensed Matter*, 64:189–193, 1986.

[3] M.K.Wu, J.R.ashburn, C.J.Torng, P.H.Hor, R.L.Meng, L.Gao, Z.J.Huang, and C.W.Chu. Superconductivity at 93 K in a new mixed-phase YBCO compound system at ambient pressure. *Physical Review Letters*, 58:908–910, 1987.

[4] E.J.Eck. Superconductivity at dry ice temperatures - 195 K achieved with new synthesis method. *http://superconductors.org/195K.htm*, 2008.

[5] H.Takahashi, K.Igawa, K.Arii, Y.Kamihara, M.Hirano, and H.Hosono. Superconductivity at 43 K in an iron-based layered compound $LaO_{1-x}F_xFeAs$. *Nature*, 453:376–378, 2008.

[6] G.F.Chen, Z Li, D Wu, G Li, W. Z Hu, J Dong, P Zheng, J. L Luo, and N. L Wang. Superconductivity at 41 K and its competition with spin-density-wave instability in layered $CeO_{1-x}F_xFeAs$. *Physical Review Letters*, 100(24):247002, Jun 2008.

[7] R.F.Service. The next big hurdle: Economics. *Science*, 314:1075 – 1077, Jul 2006.

[8] J.Clarke and D.C.Larbalestier. Wired for the future. *Nature (physics)*, 2:794 –797, Dec 2006.

[9] A.P.Malozemoff, J.Mannhart, and D.Scaiapino. High-temperature cuprate superconductors get to work. *Physics Today*, (April):41 – 47, Mar 2005.

[10] P.J.Masson, G.V.Brown, D.S.Soban, and C.a.Luongo. HTS machines as enabling technology for all-electric airborne vehicles. *Supercond. Sci. Technol.*, 20:748 – 756, Jun 2007.

[11] C.V.Deimling, W.H.Hchreiner, A.R.Jurello, and P.N.Lisboa-filho. Surface electronic structure and chemical bounding of $REBa_2Cu_3O_2$ (RE =

Y,Pr,Gd,Eu,Er and Sm). *Revista Brasileira de Aplicações de Vácuo*, 24(2): 73–75, Feb 2004.

[12] L. Rostila, J. Lehtonen, R. Mikkonen, J. Souc, E. Seiler, T. Melísek, and M.Vojenciak. How to determine critical current density in YBCO tapes from voltage-current measurements at low magnetic fields. *Supercond. Sci.Technol.*, 20(12):1097–1100, 2007.

[13] J.Bardeen, L.N.Cooper, and J.R.Schrieffer. Theory of superconductivity. *Physical Review Letters*, 108(5):1175 – 1204, Jun 1957.

[14] Y.Tanaka, D.D.Shivagan, A.Crisan, A.Iyo, and p.M.Shirage. Phase diagram of a lattice of vortex molecules in multicomponent superconductors and multilayer cuprate superconductors. *Supercond. Sci. Technol.*, 21:085011, May 2008.

[15] V.J.Emery. Theory of high-tc superconductivity in oxides. *Physical Review Letters*, 58(26):2794 – 2797, Jun 1987.

[16] P.W.Anderson. The resonating valence bond state in La_2CuO_4 and superconductivity. *Science*, 235(4793):1196 – 1198, Mar 1987.

[17] A.Cho. High Tc: The mystery that defies solution. *Science*, 314:1072 – 1075, Nov 2006.

[18] J.N.Chapman. The investigation of magnetic domain structures in thin foils by electron microscopy. *J. Phys. D*, 17:623–647, 1984.

[19] R.B.Dinner, K.A.Moler, D.M.Feldmann, and M.R.Beasley. Imaging ac losses in superconducting films via scanning Hall probe microscopy. *Physical Review B*, 75(14):12, Apr 2007.

[20] Y.Paltiel, E.Zeldov, Y.N.Myasoedov, H.Shtrikman, S.Bhattacharya, M.J.Higgins, Z.L.Xiao, E.Y.Andrei, P.L.Gammel, and D.j.Bishop. Dynamic instabilities and memory effects in vortex matter. *Nature*, 403(27):398 – 401, Aug 2000.

[21] A.Forkl, T.Dragon, H.Kronmuller, H.U.Habermeier, and G.Mertens. Magneto-optical investigation of flux penetration in YBCO thin films. *Appl. Phys. Lett.*, 57(10):1067–1069, Jun 1990.

[22] A.Polyanskii, A.Pashitski, A.Gurevich, J.A.Parrell, M.Polak, D.C.Larbalestier, S.R.Foltyn, and P.N.Arendt. Magneto-optical imaging and current distributions in high-Tc superconductors. *Conference Proceedings (ISS 96')*, page 9, Jun 1996.

[23] C.Jooss, R.Warthmann, A.Forkl, and H.Kronmuller. High-resolution magneto-optical imaging of critical currents in YBCO thin films. *Physica C*, 299:215–230, Apr 1998.

[24] P.E.Goa, H.Hauglin, A.A.F.Olsen, M.Baziljevich, and T.H.Johansen. Magneto-optical imaging setup for single vortex observation. *Review of Scientific Instruments*, 74(1):141 – 145, Dec 2003.

[25] K.Ueno, H.Murakamia, I.Kawayama, Y.Doda, M.Tonouchi, and N.Chikumoto. Magneto-optical imaging of magnetic flux distribution in high-Tc superconductors. *Physica C*, 412-414:1343–1348, Oct 2004.

[26] M.Terao, Y.Yokunaga, M.tokunaga, and T.Tamegai. Observation of single vortices by magneto-optical imaging. *Physica C*, 426-431:94–98, Oct 2005.

[27] A.Villaume, L.Porcar, D.Bourgault, A.Antonevici, T.Caroff, J.P.leggeri, and C C.Villard. In situ strain and transport magneto-optical investigations in superconductors. *Supercond. Sci. Technol.*, 21:034009, Feb 2008.

[28] A.V.Bobyl, D.V.Shantsev, Y.M.galperin, T.H.johansen, M.Baziljevich, and S.F.Karmanenko. Relaxation of transport current distribution in a YBCO strip studied by magneto-optical imaging. *Supercond. Sci. Technol.*, 15:82 – 89, Dec 2002.

[29] A.Lucarelli, G.Luepke, T.J.Haugan, G.A.Levin, and P.N.Barnes. Time-resolved magneto-optical imaging of YBCO thin films in high-frequency ac current regime. *Supercond. Sci. Technol.*, 19:667 – 670, May 2006.

[30] A.N.Lykov. Numerical simulation of flux creep in high-Tc superconductors. *Supercond. Sci. Technol.*, 12:219–225, Mar 1999.

[31] K.Frikach, A.Taoufik, and S.Senoussi. Collective flux creep in YBCO (1-2-3) and the influence of the microstructure. *Physica C*, 341 - 348:1367 – 1368, May 2000.

[32] D.V.Denisov, A. L Rakhmanov, D. V Shantsev, Y. M Galperin, and T. H Johansen. Dendritic and uniform flux jumps in superconducting films. *Physical Review B*, 73:014512, Jan 2006.

[33] D.V.Denisov, D.V.Shantsev, Y.M.Galperin, E M.Choi, H.Lee, S.Lee, A.V.Bobyl, P.E.Goa, A.A.F.Olsen, and T.H.Johansen. Onset of dendritic flux avalanches in superconducting films. *Physical review letters*, 97:077002, Aug 2006.

[34] A.L.Rakhmanov, D.V.Shantsev, Y.M.Galperin, and T.H.Johansen. Finger patterns produced by thermo-magnetic instability in superconductors. *Physical Review B*, 70:224502, 2004.

[35] C.Jooss, J.Albrecht, H.Kuhn, S.Leonhardt, and H.Kronmueller. Magneto-optical studies of current distributions in high-Tc superconductors. *Reports on progress in physics*, 65:651 – 788, Apr 2002.

[36] M.T.Gonzalez, N.Hari-Babu, and D.A.Cardwell. Enhancement of Jc under magnetic field by Zn doping in melt-textured YBCO superconductors. *Supercond. Sci. Technol.*, 15:1372 – 1376, Aug 2002.

[37] A.Gurevich. Pinning size effects in critical currents of superconducting films. *Supercond. Sci. Technol.*, 20:S128 – S135, Aug 2007.

[38] N.Moutalibi and A.M'chirgui. Improved flux pinning behavior in bulk YBCO achieved by nano-alumina addition. *Journal of Physics: Conference Series*, 97: 012284, Dec 2008.

[39] Y.Z.Zhang, H.H.Wen, and Z.Wang. Thermally activated energies of yba2cu3o7and y0.8ca0.2ba2cu3o7 thin films. *Physical Review B*, 74(14):144521, Oct 2006.

[40] M.J.Qin and X.X.Yao. Ac response of high temperature superconductors in the flux creep region. *Physica C*, 272:142 – 150, Feb 1996.

[41] B.Y.Shapiro, I Shapiro, B Rosenstein, and F Bass. Dynamics and thermal instability of magnetic flux in type-II superconductors. *Physical Review B*, 71: 184508, May 2005.

[42] S.M.Hummert. Magneto - optical imaging of superconducting MgB_2 thin films. *Master Degree Thesis, (The College of William and Mary)*, Jul 2007.

[43] A. Lucarelli, S. Hümmert, A. Chaney, G. Lüpke, B. Moeckly, Y. Zhao, and S. X. Dou. Kinetic roughening of magnetic flux penetration in MgB_2 thin films. *Applied Physics Letters*, 91(22):222505, 2007.

[44] C.P.Bean. Magnetization of hard superconductors. *Physical Review Letters*, 8: 250–253, Dec 1962.

[45] E.Zeldov, J.R.Clem, M.McElfresh, and M.Darwin. Magnetization and transport currents in thin superconducting films. *Physical Review B*, 49(14):9802 – 9822, Jul 1994.

[46] M.E.Gaevskii, D.V.Shantsev, A.V.Bobyl, Yu.M.Gal'perin, and T.H.Johansen adn H.Hauglin. Magneto-optic study of spatial magnetic-field distribution relaxation in an HTSC film strip after transport current turn-on. *Physics of the Solid State*, 41(6):877 –880, Jun 1999.

[47] E.H.Brandt and M.Indenbom. Type-II-superconductor strip with current in a perpendicular magnetic field. *Physical Review B*, 48(17):12893 – 12906, Nov 1993.

[48] M.Darwin, J.Deak, L.Hou, M.McElfresh, E.Zeldov, J.r.Clem, and M.Indenbom. Effect of transport currents on the critical state of YBCO thin film. *Physical Review B*, 48(17):13192 – 13195, Jun 1993.

[49] G.P.Mikitik and E.H.Brandt. Magnetic field profiles of a superconducting strip in an oblique magnetic field. *Physica C*, Apr 2006.

[50] R.Brambilla, F.Grilli, and L.Martini. Development of an edge-element model for ac loss computation of high-temperature superconductors. *Supercond. Sci. Technol.*, 20(1):16–24, 2007.

[51] A.Lucarelli, R.Yang, G Luepke, G Levin, T Haugan, and P.N.Barnes. Ac current driven flux dynamics in YBCO coated conductors. *MRS Spring Conference Proceedings*, Jul 2007.

[52] T.H.Johansen, M.Baziljevich, H.Bratsberg, Y.Galperin, P.E.Lindelof, Y.Shen, and P.Vase. Direct observation of the current distribution in thin superconducting strips using magneto-optic imaging. *Physical Review B*, 54(22):16264–16269, Nov 1996.

[53] F.Laviano, D.Botta, A.Chiodoni, R.Gerbaldo, G.Ghigo, L.Gozzelino, S.Zannella, and E.Mezzetti. An improved method for quantitative magneto-optical analysis of superconductors. *Supercond. Sci. Technol.*, 16:71 – 79, Dec 2003.

[54] A.Furuya, H.Yoshikawa, T.Tanabe, M.Yamamoto, P.Taihades, L.Bouet, C.Despax, L.Presmanes, and A.rousset. Magneto-optical properties of a sputtered Bi-substituted Dy – FE garnet-ferrite/hematite bilayer. *Journal of Applied Physics*, 85(8):5106 – 5108, Mar 1999.

[55] R.W.Hansen, L.E.Helseth, A.Solovyev, E.Il'Yashenko, and T.H.Johansen. Growth and characterization of (1 0 0) garnets for imaging. *Journal of Magnetism and Magnetic Materials*, 272-276:2247–2249, May 2004.

[56] HAMAMATSU Photon is Our Business. Avaiable online. *http://sales.hamamatsu.com/en/home*, 2008.

[57] V.Leyton, M.Calero, and E.Z.daSilva. The first-order vortex transition line in three-dimensional anisotropic superconductors in tilted magnetic fields. *Supercond. Sci. Technol.*, 21:025011, Jan 2008.

[58] D.Giller, B.Kalisky, A.Shaulov, T.Tamegai, and Y.Yeshurun. Magneto-optical imaging of transient vortex states in superconductors. *Journal of Applied Physics*, 89(11):7481 – 7483, May 2001.

[59] L.M.Fisher, P.E.Goa, M.Bazilijevich, T.h.Johansen, A.L.rakhmanov, and V.A.Yampol'skii. Hydrodynamic instability of the flux-antiflux interface in type-II superconductors. *Physical Review Letters*, 87(24):247005, Nov 2001.

[60] David Larbalestier, Alex Gurevich, D. Matthew Feldmann, and Anatoly Polyanskii. High-Tc superconducting materials for electric power applications. *Nature*, 414(6861):368–377, 2001.

[61] M.E.Gaevski, A.V.Bobyl, D.V.Shantsev, Y.M.Galperin, T.H.Joansen, M.Baziljevich, H.Bratsberg, and S.F.Karmanenko. Magneto-optical study of magnetic-flux penetration into a current-carrying high-temperature-superconductor strip. *Physical Review B*, 59(14):9655 – 9664, Mar 1999.

[62] A.Frey. Superconducting ybco thin films in the high-frequency ac current regime. *Master Degree Thesis (The College of William and Mary)*, Jun 2006.

[63] P.N.Barnes, Gregory L Rhoads, Justin C Tolliver, Michael D Sumption, and Kevin W Schmaeman. Compact, lightweight, superconducting power generators. *Transactions on Magnetics*, 41(1):268, Jan 2005.

[64] O.Tsukamoto. Ac losses in a type-II superconductor strip with inhomogeneous critical current distribution. *Supercond. Sci. Technol.*, 18:596 – 605, Mar 2005.

[65] F.Grilli, S.P.Ashworth, and S.Stavrev. Magnetization ac losses of stacks of YBCO coated conductors. *Physica C*, 434:185 – 190, Feb 2006.

[66] C.Kwon, J.L.Young, R.G.James, G.A.Levin, T.J.Haugan, and P.N.Barnes. Effects of local artificial defects in multifilamentary coated conductors with patterned links. *Journal of Applied Physics*, 101(8):083908, Jan 2007.

[67] M.D.Sumption, E W Collings, and P N Barns. Ac loss in striped(filamentary) YBCO coated conductors leading to designs for high frequencies and field-sweep amplitudes. *Supercond. Sci. Technol.*, 18:122–134, Nov 2005.

[68] S.P. Ashworth and F.Grilli. A strategy for the reduction of ac losses in YBCO coated conductors. *Supercond. Sci. Technol.*, 19(2):227–232, 2006.

[69] M.Polak, J.Kvitkovic, P.Mozola, P.n.barnes, and g.A.Levin. Characterization of individual filaments in a multifilamentary YBCO coated conductor. *Transactions on applied superconductivity*, 17(2):3163 – 3166, Jul 2007.

[70] M.Majoros, L.Ye, T.A.Coombs, M.D.Sumption, and E.W.Collings. Transport ac losses in YBCO coated conductors. *Supercond. Sci. Technol.*, 20(9):S299–S304, Aug 2007.

[71] N.Amemiya, Satoshi Kasai, Keiji Yoda, Zhenan Jiang, George A Levin, Paul N Barnes, and Charles E Oberly. Ac loss reduction of YBCO coated conductors by multifilamentary structure. *Supercond. Sci. Technol.*, 17:1464–1471, Oct 2004.

[72] Jr W.J.Carr and C.E.Oberly. Filamentar ybco conductors for ac applications. *Transactions on applied superconductivity*, 9(2):1475, Apr 1999.

[73] G.A.Levin, P.N.Barns, N Amemiya, S Kasai, K Yoda, and Z Jiang. Magnetization losses in multifilament coated superconductors. *Appl. Phys. Lett.*, 86(7): 072509, Jan 2005.

[74] P.N.Barnes, G.A.Levin, C.Varanasi, and M.D.Sumption. Low ac loss structures in YBCO coated conductors with filamentary current sharing. *Transactions on applied superconductivity*, 15(2):2827 – 2830, May 2005.

[75] C.B.Cobb, P.N.Barnes, T.J.Haugan, J.Tolliver, E.Lee, M.Sumption, E.Collings, and C.E.Oberly. Hysteretic loss reduction in striated YBCO. *Physica C*, 382: 52–56, Sep 2002.

[76] N.Amemiya, K.Yoda, S.K.Kasai, Z.Jiang, g.A.Levin, P.n.Barnes, and Charles E C.E.Oberly. Ac loss characteristics of multifilamentary YBCO coated conductors. *Transactions on applied superconductivity*, 15(2):1637–1642, May 2005.

[77] S.Sato and N.Amemiya. Electromagnetic field analysis of an YBCO coated conductor exposed to the non-uniform magnetic field in superconducting cables. *Physica C*, 432:215 – 222, Nov 2005.

[78] C.Jooss and V.Born. Determination of electric field distributions in superconductors via magneto-optical imaging and the Faraday law. *Physical Review B*, 73:094508, Mar 2006.

[79] American Superconductor Corporation. Avaiable online. *http://www.amsuper.com*, 2008.

[80] S.Stavrev, F.Grilli, B.Dutoit, and S.P.Ashworth. Comparison of the ac losses of BSCCO and YBCO conductors by means of numerical analysis. *Supercond. Sci. Technol.*, 18:1300–1312, Aug 2005.

[81] M.Ciszek, H.G.Knoopers, J.J.Rabbers, B.tenHaken, and H.H.J.tenKate. Angular dependence of the dynamic resistance and its relation to the ac transport current loss in Bi-2223/Ag tape superconductors. *Supercond. Sci. Technol.*, 15: 1275–1280, Jul 2002.

[82] J.Fang, X.M.Luo, A.K.M.alamgir, E.W.Collings, E.Lee, M.D.Sumption, J.G.Fang, H.P.yi, X.H.Song, S.Q.Guo, M.L.Liu, Y.Xin, and Z.Han. Geometry dependence of magnetic and transport ac losses in Bi-2223-Ag tapes with different aspect ratios. *Supercond. Sci. Technol.*, 17:1173–1179, Aug 2004.

[83] N.Amemiya, O.Maruyama, m.Mori, N.Kashima, T.Watanabe, S.Nagaya, and Y.Shiohara. Lateral jc distribution of YBCO coated conductors fabricated by IBAD/MOCVD process. *Physica C*, 445-448:712 – 716, Aug 2006.

[84] S.Ohshima, K.Takeishi, A.Saito, N.Sekiya, S.Hirano, T.Suzuki, and Y Takano. New contackless Jc-measurement system for HTS coated conductors. *Physica C*, 445 -448:682 –685, Aug 2006.

[85] K.Kimura, M.Kiuchi, E.S.Otabe, T.Matsushita, S.Miyata, A.Ibi, T.Muroga, Y.Yamada, and Y.Shiohara. Film thickness dependence of critical current characteristics of YBCO-coated conductors. *Physica C*, 445-448:141 – 145, Aug 2006.

[86] J.N.A.Matthews. Next-generation high-Tc superconducting wires debut in the power grid. *Physics Today*, page 30, Jan 2008.

[87] SuperPower Inc. Avaiable online. *http://www.superpower-inc.com*, 2008.

[88] D. M. Feldmann, J. L. Reeves, A. A. Polyanskii, G. Kozlowski, R. R. Biggers, R. M. Nekkanti, I. Maartense, M. Tomsic, P. Barnes, C. E. Oberly, T. L. Peterson, S. E. Babcock, and D. C. Larbalestier. Influence of nickel substrate grain structure on $YBa_2Cu_30_{7-\delta}$ supercurrent connectivity in deformation-textured coated conductors. *Applied physics Letter*, 77(18):2906–2908, 2000.

[89] H.Claus, U.Welp, H.Zheng, L.Chen, A.P.Paulikas, B.W.Veal, K.E.Gray, and G.W.Crabtree. Critical current across grain boundaries in melt-textured $YBa_2Cu_30_{7-\delta}$ rings. *Physical Review B*, 64(14):144507, Sep 2001.

[90] R.J.Wijingaarden, K.Heeck, H.J.W.Spoelder, R.Surdeanu, and R.Griessen. Fast determination of 2D current patterns in flat conductors from measurement of their magnetic field. *Physica C*, 295:177–185, Apr 1998.

RAN YANG was born in SiChuan, China, the only daughter of an ordinary Chinese family. She moved to the United States in 2003. She lives in Hampton roads of Virgina with her husband and two dogs.